National Library of Canada
Bibliothèque nationale du Canada

Canadian Theses Service
Service des thèses canadiennes

Ottawa, Canada
K1A 0N4

NOTICE

The quality of this microform is heavily dependent upon the quality of the original thesis submitted for microfilming. Every effort has been made to ensure the highest quality of reproduction possible.

If pages are missing, contact the university which granted the degree.

Some pages may have indistinct print especially if the original pages were typed with a poor typewriter ribbon or if the university sent us an inferior photocopy.

Reproduction in full or in part of this microform is governed by the Canadian Copyright Act, R.S.C. 1970, c. C-30, and subsequent amendments.

AVIS

La qualité de cette microforme dépend grandement de la qualité de la thèse soumise au microfilmage. Nous avons tout fait pour assurer une qualité supérieure de reproduction.

S'il manque des pages, veuillez communiquer avec l'université qui a conféré le grade.

La qualité d'impression de certaines pages peut laisser à désirer, surtout si les pages originales ont été dactylographiées à l'aide d'un ruban usé ou si l'université nous a fait parvenir une photocopie de qualité inférieure.

La reproduction, même partielle, de cette microforme est soumise à la Loi canadienne sur le droit d'auteur, SRC 1970, c. C-30, et ses amendements subséquents.

NL-339 (r. 88/04) c

Canada

THE UNIVERSITY OF ALBERTA

AN ISOPARAMETRIC HERMITIAN FINITE ELEMENT FOR DUCT ACOUSTICS WITH FLOW

BY

DAVID CHARLES STREDULINSKY

A THESIS

SUBMITTED TO THE FACULTY OF GRADUATE STUDIES AND RESEARCH

IN PARTIAL FULFILMENT OF THE REQUIREMENTS FOR THE DEGREE

OF DOCTOR OF PHILOSOPHY

DEPARTMENT OF MECHANICAL ENGINEERING

EDMONTON, ALBERTA

SPRING, 1990

National Library of Canada
Bibliothèque nationale du Canada

Canadian Theses Service
Service des thèses canadiennes

Ottawa, Canada
K1A 0N4

NOTICE

The quality of this microform is heavily dependent upon the quality of the original thesis submitted for microfilming. Every effort has been made to ensure the highest quality of reproduction possible.

If pages are missing, contact the university which granted the degree.

Some pages may have indistinct print especially if the original pages were typed with a poor typewriter ribbon or if the university sent us an inferior photocopy.

Reproduction in full or in part of this microform is governed by the Canadian Copyright Act, R.S.C. 1970, c. C-30, and subsequent amendments.

AVIS

La qualité de cette microforme dépend grandement de la qualité de la thèse soumise au microfilmage. Nous avons tout fait pour assurer une qualité supérieure de reproduction.

S'il manque des pages, veuillez communiquer avec l'université qui a conféré le grade.

La qualité d'impression de certaines pages peut laisser à désirer, surtout si les pages originales ont été dactylographiées à l'aide d'un ruban usé ou si l'université nous a fait parvenir une photocopie de qualité inférieure.

La reproduction, même partielle, de cette microforme est soumise à la Loi canadienne sur le droit d'auteur, SRC 1970, c. C-30, et ses amendements subséquents.

ISBN 0-315-60323-2

NL-339 (r. 88/04) c

Canada

THE UNIVERSITY OF ALBERTA

RELEASE FORM

NAME OF AUTHOR: **STREDULINSKY, DAVID CHARLES**

TITLE OF THESIS: **AN ISOPARAMETRIC HERMITIAN FINITE ELEMENT FOR DUCT ACOUSTICS WITH FLOW**

DEGREE: **DOCTOR OF PHILOSOPHY**

YEAR THIS DEGREE GRANTED: **1990**

Permission is hereby granted to THE UNIVERSITY OF ALBERTA LIBRARY to reproduce single copies of this thesis and to lend or sell such copies for private, scholarly or scientific research purposes only.

The author reserves other publication rights, and neither the thesis or extensive extracts from it may be printed or otherwise reproduced without the author's written permission.

D.C. Stredulinsky
(Student's signature)

PERMANENT ADDRESS:

R.R. 1

Hornby Island

British Columbia

Date: MARCH 19, 1990

THE UNIVERSITY OF ALBERTA

FACULTY OF GRADUATE STUDIES AND RESEARCH

The undersigned certify that they have read, and recommend to the Faculty of Graduate Studies and Research for acceptance, a thesis entitled An Isoparametric Hermitian Finite Element for Duct Acoustics with Flow submitted by David Charles Stredulinsky in partial fulfilment of the requirements for the degree of Doctor of Philosophy.

Dr. A. Craggs ..... Supervisor

Dr. M. G. Faulkner .....

Dr. W. A. Lipsett .....

Dr. F. E. Vermeulen .....

Dr. W. Eversman .....

Date: MARCH 19, 1990

ABSTRACT

A new cubic isoparametric Hermitian hexahedral finite element is developed to efficiently model the propagation of sound through rigid walled duct bends and junctions. With the goal of improved technology transfer, the computer programs developed are implemented on a desk top computer.

The element is first tested for the acoustic enclosure eigenvalue problem and the incompressible potential fluid flow problem. It is demonstrated that the new element generally gives more accurate results, on a degree of freedom basis, than the conventional cubic isoparametric element, but under certain distortions is less accurate.

A finite element model using this element is then developed to study the propagation of sound through duct bends and junctions including the convective effect of low Mach number steady fluid flow, modeled using incompressible potential flow theory. The finite element solution for the flow field is obtained first and then used in the acoustic finite element model. Higher order mode boundary conditions are considered in linking the junction or bend finite element models to anechoically terminated straight ducts containing uniform flow. The method is then tested by considering up to and including third cross mode propagation in a two-dimensional straight duct with a uniform flow at Mach 0.1. Models with three elements across the duct width gave accurate predictions up to a duct width to wavelength ratio of two.

The procedure is then used to study several duct bends and junctions. It is found that due to the complexity of the geometry and sound fields, with the largest numerical models that could be handled by the desk top computer, accurate

results could only be obtained for propagation of the plane wave and first cross mode up to a duct width to wavelength ratio approaching one. A 90° and a 45° side branch are considered. The effect of varying the side branch width and flow is demonstrated. It is found that, for inlet Mach numbers of 0.1 or less, the effect of flow on the bend and junction transmission losses is small.

ACKNOWLEDGEMENTS

The author would like to express his appreciation to Dr. A. Craggs and Dr. M.G. Faulkner for their guidance and supervision and also to his wife Claire for her support. Thanks are due also to Mr. E.H. Bolstad for the use of his computer and plotter. The author also gratefully acknowledges the Killam Scholarship committee and the National Research Council of Canada (grant A7431 - Craggs) for providing the funding that has enabled the author to undertake these studies.

TABLE OF CONTENTS

CHAPTER		PAGE
I	INTRODUCTION	1
	1.1 Scope of Work	1
	1.2 Review of Previous Research	2
	1.2.1 Literature Related to Duct and Duct Component Acoustics	2
	1.2.2 Literature Related to the Use of Finite Elements in Acoustics	5
	1.3 The Duct Network Problem	10
II	ISOHERM32 ELEMENT DEVELOPMENT	13
	2.1 Choosing the Element	13
	2.2 Element Shape Functions and Geometric Transformation	15
	2.2.1 Equation Development	15
	2.2.2 Continuity Between Elements	21
	2.2.3 The ISOHERM12 Element	22
	2.3 Testing the Element: The Acoustic Eigenvalue Problem	23
	2.3.1 Equation Development	23
	2.3.2 Modeling A Rectangular Enclosure	27
	2.3.2.1 Model with One Element	27
	2.3.2.2 Linking Several Elements in One Dimension	30
	2.3.2.3 Distortion of the Elements within a Rectangular Enclosure	33
	2.3.3 Modeling A Cylindrical Cavity	39

TABLE OF CONTENTS (continued)

CHAPTER PAGE

2.3.4 Modeling A Complex Shaped Enclosure 43

2.4 Testing the Element: Incompressible Potential Flow . . . 48

2.4.1 Equation Development 48

2.4.2 Uniform Flow in a Straight Duct 53

2.4.3 Uniform Radial Flow from a Point Source 54

III FEM MODEL DEVELOPMENT FOR ACOUSTICS WITH FLOW 63

3.1 Equation Development 63

3.1.1 Selecting a Flow Model 63

3.1.2 Basic Equations 66

3.1.3 The Convected Wave Equation 68

3.1.4 The Acoustic-Flow FEM Development 70

3.1.5 Solution with plane wave boundary conditions 72

3.1.5.1 A Specified Acoustic Particle Velocity 73

3.1.5.2 An Anechoic Termination 74

3.1.5.3 Incident Wave Specified 78

3.1.5.4 Equation Solution Using Real Quantities . . . 80

3.1.6 Solution with Higher Order Mode Boundary Conditions 81

3.1.6.1 Higher Order Modes in a Straight Duct with Uniform Flow 81

3.1.6.2 Higher Order Mode Anechoic Termination . . 83

TABLE OF CONTENTS (continued)

CHAPTER PAGE

3.1.6.3 Higher Order Mode Incident Wave Termination 84

3.1.6.4 Junction with Incident Wave and Anechoic Terminations 85

3.1.7 Sound Power Transmission 92

3.1.7.1 Sound Power Transmission in a Straight Duct . 93

3.1.7.2 Junction and Bend Sound Power Transmission and Reflection 95

3.2 Tests of the FEM for Plane Waves in Straight Ducts . . . 97

3.2.1 Propagation with the Inlet Acoustic Velocity Specified 97

3.2.2 Propagation with a Specified Incident Velocity Potential 103

3.3 Tests of the FEM Model Including Higher Order Modes . 107

3.3.1 Mode Shapes and Eigenfrequencies for Rectangular Ducts 107

3.3.2 Propagation in a Straight Duct with Uniform Flow 112

3.3.3 Propagation in a Duct Bend 126

IV PROPAGATION OF SOUND THROUGH DUCT BENDS AND JUNCTIONS 132

4.1 Introduction 132

4.2 A Mitred 90 Degree Bend 133

4.3 A Curved 90 Degree Bend with Turning Vane 139

TABLE OF CONTENTS (continued)

CHAPTER		PAGE
	4.4 Propagation Through Duct Junctions	146
	4.4.1 Low Frequency Approximations for Duct Junctions	148
	4.4.2 FEM Predictions for a 90 Degree Equal Width Side Branch	150
	4.4.3 FEM Predictions for a 90 Degree Half Width Side Branch	165
	4.4.4 FEM Predictions for a 45 Degree Side Branch . . .	166
V	CONCLUDING REMARKS	172
	5.1 Summary	172
	5.2 Areas of Further Research	175
BIBLIOGRAPHY		179

LIST OF TABLES

Table		Page
2.1	Eigenvalues for a Rectangular Rigid Walled Box with Dimensions $l_x = a$, $l_y = 0.6a$ and $l_z = 0.8a$, Modeled with One Element	29
2.2	Eigenvalues for a Two-element Box of Dimensions $l_x = a$, $l_y = 0.6a$ and $l_z = 0.8a$ with the Common Plane Rotated . . .	34
2.3	Eigenvalues for a Two-element Box of Dimensions $l_x = a$, $l_y = 0.6a$ and $l_z = 0.8a$ with the Common Plane Twisted . . .	36
2.4	Eigenvalues for a Two-dimensional Model of a Circular Cylinder	42
2.5	Natural Frequencies for Acoustic Modes in an Automobile Passenger Enclosure Model	47
2.6	Sector Flow Model Degrees of Freedom	57
2.7	Errors in Sector Flow Velocities with Geometrically Similar Elements	61
3.1	Convergence for Plane Wave Propagation in a Straight Duct with Uniform Flow	100
3.2	Comparison of Models for Plane Wave Propagation in a Straight Duct with Uniform Flow	102
3.3	Convergence for Plane Wave Propagation in a Straight Duct with the Incident Wave Specified	105
3.4	Total Sound Power Check for Plane Wave Propagation in a Straight Duct with the Incident Wave Specified	106
3.5	Eigenvalues and Modal Power Factors for Duct Cross-sections .	112
3.6	Convergence for First Cross Mode Propagation in a Straight Duct with the First Cross Mode Incident	124

LIST OF FIGURES

Figure		Page
2.1	The ISOHERM32 Finite Element	16
2.2	Convergence of the ISOHERM32 Element Models for the Prediction of the Eigenvalues for the Acoustic Modes in a One-dimensional Tube	31
2.3	Convergence of Different FEM Models for the Prediction of the Eigenvalue for the Mode [1,0,0] in a One-dimensional Tube . .	32
2.4	Convergence of Different FEM Models for the Prediction of the Eigenvalues for Higher Order Modes in a One-dimensional Tube	33
2.5	Element Distortion Within a Two-element Box	35
2.6	The Effect of Distortion of the Common Plane in an ISOHERM32 Two-element Box on the Eigenvalues ka	38
2.7	The Effect of Distortion of the Common Plane in a Two-element Box on the Eigenvalues for the [1,0,0] Mode	38
2.8	Finite Element Models for a Circular Cylinder	41
2.9	Model of an Automobile Enclosure	44
2.10	Finite Element Models of an Automobile Passenger Enclosure .	45
2.11	Flow Model of a Duct Junction	50
2.12	Two-element Models for Uniform Flow	54
2.13	Models for the Sector Flow Problem	56
2.14	Maximum Errors for the Sector Flow Models with Equal Length Elements	58
2.15	Maximum Errors for the Sector Flow Models with Geometrically Similar Elements	58
2.16	Comparison of Maximum Errors for the First and Last Elements of the Sector Flow Models with Geometrically Similar Elements	60

LIST OF FIGURES (continued)

Figure		Page
2.17	Maximum Element Errors for Sector Flow Velocities with the 67 DOF Models	60
3.1	Linking the FEM Model to a Straight Duct	76
3.2	Straight Duct with a Uniform Cross-section	82
3.3	Two-Element Model for Plane Wave Propagation in a Straight Duct	98
3.4	Rectangular Duct Cross-section Models	109
3.5	Finite Element Meshes for a Straight Duct	113
3.6	Plane Wave Acoustic Velocity Potential for a Straight Duct with no Flow	115
3.7	First Cross Mode Acoustic Velocity Potential for a Straight Duct with No Flow	116
3.8	Second Cross Mode Acoustic Velocity Potential for a Straight Duct with No Flow	116
3.9	Third Cross Mode Acoustic Velocity Potential for a Straight Duct with No Flow	118
3.10	Outlet Plane Wave Acoustic Velocity Potential for a Straight Duct with a Uniform Flow	119
3.11	Outlet First Cross Mode Acoustic Velocity Potential for a Straight Duct with a Uniform Flow	120
3.12	Outlet Second Cross Mode Acoustic Velocity Potential for a Straight Duct with a Uniform Flow	121
3.13	Outlet Third Cross Mode Acoustic Velocity Potential for a Straight Duct with a Uniform Flow	122
3.14	ISOHERM12 Finite Element Models for a Duct Bend	127
3.15	Bend Reflection and Transmission Coefficients with a Plane Wave Incident	128

LIST OF FIGURES (continued)

Figure		Page
3.16	Bend Reflection and Transmission Coefficients with the First Cross Mode Incident	129
4.1	ISOHERM12 Meshes for a 90 Degree Mitred Duct Bend . . .	134
4.2	Convergence of FEM Models of a 90 Degree Mitred Bend with No Flow and a Plane Wave Incident	135
4.3	Convergence of FEM Models of a 90 Degree Mitred Bend with No Flow and the First Cross Mode Incident	136
4.4	Propagation Characteristics of a 90 Degree Mitred Bend with Flow and a Plane Wave Incident	137
4.5	Propagation Characteristics of a 90 Degree Mitred Bend with Flow and the First Cross Mode Incident	138
4.6	ISOHERM12 Meshes for Curved 90 Degree Bends with an Inner Radius of $0.5a$ and an Outer Radius of $1.5a$	140
4.7	Convergence of FEM Models for a Curved 90 Degree Bend with a Turning Vane Radius of $0.875a$ and a Plane Wave Incident .	141
4.8	Convergence of FEM Models for a Curved 90 Degree Bend with a Turning Vane Radius of $1.125a$ and a Plane Wave Incident .	142
4.9	Comparison of the FEM with Experiment and the FDM of Reference [9] for the Plane Wave Transmission Loss of a Curved 90 Degree Bend with a Turning Vane at a Radius of $0.875a$ . . .	144
4.10	Comparison of the FEM with Experiment and the FDM of Reference [9] for the Plane Wave Transmission Loss of a Curved 90 Degree Bend with a Turning Vane at a Radius of $1.125a$ . . .	144
4.11	ISOHERM12 Meshes for a 90 Degree Side Branch with Equal Width Ducts	151
4.12	Convergence of FEM Models for a 90 Degree Side Branch with the Same Width as the Main Duct and a Plane Wave Incident with No Flow	152

LIST OF FIGURES (continued)

Figure		Page
4.13	Convergence of FEM Models for a 90 Degree Side Branch with the Same Width as the Main Duct and the First Cross Mode Incident with No Flow	153
4.14	Comparison with Other Approximate Solutions for a 90 Degree Side Branch with the Same Width as the Main Duct and a Plane Wave Incident with No Flow	154
4.15	The Effect of Flow on Sound Propagation for a 90 Degree Side Branch with the Same Width as the Main Duct and an Equal Flow Split with a Plane Wave Incident	157
4.16	The Effect of Flow on Sound Propagation for a 90 Degree Side Branch with the Same Width as the Main Duct and an Equal Flow Split with the First Cross Mode Incident	158
4.17	Change in RL and TL with respect to the No-flow Case for a 90 Degree Side Branch with the Same Width as the Main Duct and an Equal Flow Split with a Plane Wave Incident	159
4.18	Change in RL and TL with respect to the No-flow Case for a 90 Degree Side Branch with the Same Width as the Main Duct and 10% of the Flow Out the Side Branch with a Plane Wave Incident	160
4.19	Change in RL and TL with respect to the No-flow Case for a 90 Degree Side Branch with the Same Width as the Main Duct and 90% of the Flow Out the Side Branch with a Plane Wave Incident	161
4.20	Change in RL and TL with respect to the No-flow Case for a 90 Degree Side Branch with the Same Width as the Main Duct and an Equal Flow Slit with the First Cross Mode Incident . . .	162
4.21	Change in RL and TL with respect to the No-flow Case for a 90 Degree Side Branch with the Same Width as the Main Duct and 10% of the Flow Out the Side Branch with the First Cross Mode Incident	163
4.22	Change in RL and TL with respect to the No-flow Case for a 90 Degree Side Branch with the Same Width as the Main Duct and 90% of the Flow Out the Side Branch with the First Cross Mode Incident	164

LIST OF FIGURES (continued)

Figure		Page
4.23	ISOHERM12 Element Mesh for a 90 degree Side Branch with Half the Width of the Main Duct	166
4.24	The Effect of Flow on Sound Propagation for a 90 Degree Side Branch with Half the Width of the Main Duct and 1/3 of the Flow Out the Side Branch with a Plane Wave Incident . . .	167
4.25	The Effect of Flow on Sound Propagation for a 90 Degree Side Branch with Half the Width of the Main Duct and 1/3 of the Flow Out the Side Branch with the First Cross Mode Incident	168
4.26	ISOHERM12 Element Mesh for a Junction with a 45 Degree Side Branch	169
4.27	Propagation of Sound Through a Duct Junction with a 45 Degree Side Branch and No Flow for a Plane Wave Incident . .	171

CHAPTER I

INTRODUCTION

1.1 Scope of Work

The use of ducted systems for heating, ventilation and air conditioning is widespread in modern building practice. These systems commonly incur noise problems and thus there is a need for accurate prediction of noise generation and propagation within duct systems. Typically the major noise sources are the supply and return air fans, and other components such as dampers, outlet diffusers and duct bends where noise is generated by the movement of the air through the components. The sound field produced by these sources within the duct system depends on the geometric layout of the system, the characteristics of the duct walls (flexible, rigid or lined, for example, with a fibrous acoustically absorptive liner), and the manner in which the ducts are terminated. As well as generating noise, the air flow through the system can have the convective effect of increasing or decreasing the speed at which various transmitted and reflected sound waves travel through the system. This can lead to changes in phase and "bending" of the wave fronts.

This thesis has considered only a part of the problem—the propagation of sound through specific duct components such as bends and junctions. The problem of how or where the sound is generated has not been considered in this work. Also, the present work has been limited to the study of rigid walled components but could be extended to include locally reacting boundaries.

As part of this work, a new finite element has been developed which has certain advantages over previously used elements for duct acoustics. The propagation of plane waves and higher order modes has also been considered, including the convective effect of steady air flow on the acoustic propagation at low Mach number. The steady air flow has been modeled based on incompressible potential flow theory. The subject of internal flow generated noise sources has not been considered in this work.

With a goal of improved technology transfer, the numerical computer methods have been developed and used on a desk top computer.

1.2 Review of Previous Research

The analytical solution of problems in acoustics is generally only possible for very simple geometries. For more complicated geometries, numerical or experimental methods must generally be used. The Finite Element method (FEM), and other numerical methods, for example, the Finite Difference method (FDM) and more recently the Boundary Element method (BEM), have been implemented in many areas of acoustics and noise control including small room acoustics, loudspeaker design, and the study of sound propagation in mufflers and duct system components.

1.2.1 Literature Related to Duct and Duct Component Acoustics

The following paragraphs outline some of the analytical and numerical work related to sound propagation in ducts and duct system components. The review is not comprehensive but should give a reasonable indication of the research conducted in this field. In particular, since this thesis concentrates on problems with hard wall boundary conditions, much of the recent literature concerning lined and flexible walled ducts has not been included.

The propagation of sound through rigid right-angled joints and "T"-junctions with plane wave inputs and outputs and no flow was treated analytically by Miles [39] in 1939 using an electrical circuit analogy. In 1954, Lippert [37], [38] conducted some experimental work with bends in rectangular ducts with no flow. More recent analytical work on the analysis of straight rigid walled ducts includes work by Morfey [40] in 1971 on ducts with a uniform steady flow and the study of source distributions in ducts of finite length by Doak [26], [27] in 1973. Analytical work on sound propagation in curved ducts and bends with no flow includes that by Rostafinsky [47], [48], [49], Osbourne [43] and Cummings [24]. Fuller and Bies [33] considered analytically a 180 degree curved bend containing a turning vane. The work of Miles [39] on right-angle bends and "T"-junctions with no flow was extended by von Said [57] in 1975 to include higher order mode propagation. Cummings [25] gave an analytical solution to the problem of sound propagation in a 180 degree mitred bend with no flow in 1975. In 1982, Redmore et al [46], studied the propagation of sound into a duct side branch using a mode coupling theory.

Most of the analytical work outlined above considers geometries where the duct components can be broken down into rectangular or cylindrical segments, so that analytical solutions to the wave equation or the Helmholtz equation in rectangular or cylindrical coordinates can be employed. In curved ducts with flow, and generally in nonuniform ducts with and without flow one must resort to numerical methods. The sound transmission in nonuniform lined ducts with no flow was studied in 1975 by Eversman, Cook and Beckemeyer [32] using the method of weighted residuals (MWR) and Astley and Eversman [3] in 1978 with the FEM. Also in 1978, Sigman, Majjigi and Zinn [53] used the FEM to study a nonuniform hard walled duct with high subsonic flow as applied to turbofan inlet acoustics. The acoustic

eigenvalue problem of lined uniform two-dimensional and axisymmetric ducts with sheared flows was investigated by Astley and Eversman [4], [5] with the FEM. The acoustic transmission in nonuniform lined ducts with high subsonic flow was investigated in 1981 by Astley and Eversman using the MWR [31] and the FEM [6] and also by Ling, Hamilton and Allen [36] in 1982 using the FEM.

Curved rigid walled bends of various angles, with no flow, were modeled by Cabelli [9] in 1980 with the FDM including some examples with turning vanes. Cabelli and Shepherd [13], [51] studied the no flow transmission characteristics of higher order modes in various mitred and curved bends using the FEM. The acoustics of a duct bend with a subsonic compressible steady flow was investigated by Cabelli [10] in 1982 with the FEM. In 1984 Cabelli and Shepherd [14] also used a three-dimensional time dependent FDM to model a mitred bend with no flow. The time dependent FDM was also employed by Cabelli [11] in 1985 to study the acoustic and vibration interaction in a uniform duct in which one wall was modeled as a flexible plate.

Young and Crocker [58] found the four-pole parameters of a reactive muffler (rectangular expansion chamber) for no flow with the FEM in 1975. In 1976 Craggs [20] studied the plane wave transmission characteristics of axisymmetric reactive mufflers with no flow also using the FEM and extended the work to lined dissipative mufflers in reference [21]. Axisymmetric expansion chamber mufflers with no flow have also been modeled by Seybert and Cheng [50] using the BEM in 1987. The four-pole parameters of axisymmetric muffler expansion chambers with low Mach number steady flows were investigated with the FEM by Peat [45] in 1982.

1.2.2 Literature Related to the Use of Finite Elements in Acoustics

This section reviews in more detail, the use of the FEM to solve acoustic problems and is presented in approximate chronological order of development. One of the earliest works concerning the use of finite elements in acoustics was Gladwell [34] in 1965. In this work, acoustic energy variational or extremum principles were given which lead to the governing differential equations and boundary conditions. These variational principles were applied to the approximate finite element models using the Ritz variational method. Square elements with cubic polynomial shape functions, and the acoustic pressure and two spatial derivatives as corner node quantities, were employed to predict the resonant frequencies of a square two-dimensional room. A one-element and a four-element model were used.

In 1971 Craggs [17] used a three-dimensional cuboid element, with cubic Hermite polynomials and the acoustic velocity potential and spatial derivatives as nodal quantities, to model the acoustics of a rectangular room using a Ritz variational formulation. A one-element model predicted the eigenvalues for the first seven room modes to within 0.13 percent of the exact solution. Craggs [18], [19] also employed tetrahedral elements with linear shape functions and the acoustic pressure as the nodal quantity to model the acoustics of a complex shaped three-dimensional cavity. This element gave higher errors and lower rates of convergence than the cubic Hermitian element of reference [17], but could model complex geometries. Shuku and Ishihara [52] looked at a similar problem in two dimensions with a triangular element using cubic shape functions and the acoustic pressure and its spatial derivatives as the nodal quantities. When two of these cubic triangular elements were used to model a rectangular room, errors in the lowest mode eigenvalues were thirty times larger than obtained with the cubic Hermitian element of reference [17].

The acoustic pressure and its spatial derivatives were also employed in a rectangular cubic Hermitian element model by Young and Crocker [58] to model a two-dimensional rectangular expansion chamber. The chamber transmission loss was obtained from acoustic four-pole parameters derived from the FEM model. Propagation in the connecting ducts was restricted to plane waves and predictions made up to a chamber width to wavelength ratio of 1.2. Craggs [20], [21] studied axisymmetric reactive and dissipative mufflers using isoparametric hexahedral elements with linear Serendipity shape functions and the acoustic pressure as the nodal quantity, also restricting input and output connecting ducts to plane waves. Craggs and Stead [22] used two-dimensional rectangular cubic Hermitian elements in terms of acoustic pressure and its spatial derivatives (the variation in the third dimension prescribed) and plate elements to study the coupled response of two rectangular rooms separated by a flexible partition.

Astley and Eversman [3] studied the acoustic transmission in nonuniform ducts, including higher order modes in connecting straight ducts, using a Galerkin formulation with two-dimensional quadrilateral isoparametric elements, quadratic Serendipity shape functions and the acoustic pressure as the nodal quantity. They also implemented a formulation based on three linear differential equations in terms of the acoustic pressure and the acoustic velocities in two dimensions instead of the usual formulation in terms of a second order differential equation.

Sigman, Majjigi and Zinn [53] investigated the acoustics of a nonuniform duct with high subsonic irrotational flow with a Galerkin formulation with linear triangular elements in terms of the acoustic velocity potential. Astley and Eversman [4], [5] used one-dimensional quadratic Lagrangian elements and cubic Hermitian elements to study the soft walled duct cross-section eigenvalue problem

with a sheared steady flow. Astley and Eversman [6] then extended their work of reference [3] to include the effect of a high subsonic compressible steady flow in nonuniform ducts. A rotational steady flow model was employed which meant that the governing equations could not be reduced to a single equation in terms of the acoustic pressure or velocity potential. Instead a Galerkin formulation with the acoustic pressure and acoustic velocity components as dependent variables was used.

Cabelli and Shepherd [13], [51] considered the acoustic characteristics of duct bends with no flow using two-dimensional quadratic isoparametric quadrilateral element models in terms of acoustic pressure. Higher order mode propagation was considered and predictions given up to a duct width to wavelength ratios of 1.5. Cabelli [10] then extended this work to include an irrotational compressible steady flow. The steady flow solution was obtained using the FEM with six-noded triangular finite elements and the stream function and local density as nodal variables. The governing acoustic equations were solved with eight-noded quadrilateral isoparametric elements in terms of the acoustic velocity potential.

Ling, Hamilton and Allen [36] also looked at the problem of a nonuniform duct with flow. They used cubic quadrilateral isoparametric elements with Serendipity shape functions in a Galerkin formulation in terms of the acoustic pressure. The element was developed based on the convected wave equation with uniform flow along one axis of the element. The square parent elements were then distorted using an isoparametric transformation to fit between the streamlines of the approximate flow model.

Peat [45] evaluated the four-pole parameters of nonuniform axisymmetric duct components with an incompressible potential steady flow model applicable to

low Mach number flows. A Galerkin formulation with eight-noded quadrilateral isoparametric elements was used to first solve the Laplace equation for the steady flow velocity potential and then solve the governing acoustic equation for the acoustic velocity potential. The connecting ducts were restricted to plane waves and predictions made up to a diameter to wavelength ratio of 0.23.

Finite elements have also been employed to solve the problem of radiation of sound from a vibrating source into an unbounded space or half space. One major difficulty in using the FEM for this type of problem is that the computational domain must be of finite size. Astley [2] looks at this problem with the added complication of a moving flow using conventional 9-noded quadratic isoparametric quadrilateral Lagrangian elements in the region near the source and wave envelope elements in the outer region. Recently Kaizer and Leeuwestein [35] used linear triangular elements in terms of the acoustic velocity potential to study sound radiation from nonrigid loudspeaker diaphragms.

Some observations based on the work outlined above are summarized as follows:

- Most of this FEM work has been done with two-dimensional finite elements to solve two-dimensional problems or three-dimensional axisymmetric problems. Some work involving the acoustics of irregular shaped enclosures has used three-dimensional elements.
- The earlier work employed formulations based on variational principles. In later work, the Galerkin method has become more popular since it is applicable to a larger range of problems and gives the same formulation as the Ritz variational method for problems where variational principles exist.

- In the earliest work, rectangular brick elements were used to model problems with rectangular geometry. These elements utilized the acoustic pressure or velocity potential as a nodal quantity which gave C^0 continuity between elements, or also included the spatial derivatives of the dependent variable as nodal quantities in Hermitian type elements having C^1 continuity.
- Complex geometries were initially modeled with triangular or tetrahedral elements, or using these elements in combination with rectangular or cuboid elements. In later work, isoparametric elements having C^0 continuity with just the dependent variable as the nodal quantity have been widely used. This type of element has the advantage that the element boundaries can be distorted to model curved surfaces. However, with this type of element, involving coordinate transformations between element and global domains, element integrations must generally be carried out with numerical integration rules as opposed to the earlier non-distortable elements in which the polynomial shape functions could be integrated analytically.
- The cubic Hermitian brick element, employed to model rectangular acoustic enclosures and muffler expansion chambers, gave more accurate results and higher rates of convergence than elements with linear or quadratic shape functions and was also more accurate than the cubic triangular element of reference [52]. However this element could only model rectangular geometries and could not handle the more complex enclosures easily modeled with other types of elements.

1.3 The Duct Network Problem

Current engineering methods for noise prediction in a heating, ventilation and air conditioning (HVAC) duct system, for example [1], typically start at a noise source such as a fan and trace the sound power attenuation along a given path in the system to the outlet in a room. Reflected sound waves within the system are not considered and typically the division of the sound power at junctions or branches is based on the connecting duct volume flows or cross-section areas. No explicit consideration is given as to how various acoustical modes propagate within the system. These methods are to some extent empirical and in some cases based on limited data. In many cases the results are unreliable.

Prior to commencing the research for this thesis, the author was involved in research concerning sound propagation in duct networks—Craggs and Stredulinsky [23], and Stredulinsky, Craggs and Faulkner [55]. The work was an initial attempt at obtaining more accurate low frequency predictions. It was this work that established the direction and purpose of the present thesis research. In the previous work, a computer prediction method was developed and used on a desk top computer. This technique combined transfer matrix and finite element procedures to study sound propagation through duct networks. The method used analytical plane wave solutions in straight ducts and two-dimensional linear and quadratic isoparametric quadrilateral finite element models in bends, branch points and plenum sections where higher order mode propagation is important. In this work it was assumed that duct walls were rigid and there was no air flow through the system. As an extension of the above work, the present thesis research had the following goals:

- The possible development of a more efficient finite element to model bends, branch points and other components. Since the ultimate goal

of this research is to develop methods that can be used by engineers on desk top computers, it is desirable to use models which are more efficient in terms of computer memory usage and processing time.

- The investigation of the convective effects of steady air flow on the acoustic propagation, at flow rates typically occurring in HVAC systems. Although calculation of flow generated noise that commonly occurs in these types of systems is a significant part of any overall duct system noise prediction program, this has not been included in the scope of the present research.
- The extension of the model to higher frequencies by considering higher order mode propagation. The original network model considered only plane wave propagation in straight duct sections and constrained the finite element models to plane wave inputs and outputs to link to the straight ducts.

Only the sound propagation through isolated bend and branch components has been considered in the current work. The incorporation of the work into an overall network prediction scheme has not been included in the scope of this thesis.

In Chapter II, a hexahedral element is developed which is based on the cubic Hermitian brick element. This element has the added capability that it can be distorted to model curved boundaries and thus model more complex geometries. A two dimensional version of the element is also developed. This element is then tested by solving the acoustic enclosure eigenvalue problem for a rigid walled rectangular enclosure and for more complex enclosures. The element is also used to model the two-dimensional incompressible potential flow problem governed by the Laplace equation. In both problems the results are compared to standard linear and cubic isoparametric element models.

In Chapter III. the element developed in Chapter II is applied to the problem of sound propagation in the presence of a steady flow. Equations are developed for finite element modeling of duct bends and junctions or branch points. It is assumed that the bends and junctions connect to infinitely long or anechoically terminated straight ducts which can contain a uniform steady flow. The method was initially tested allowing only plane wave propagation in the connecting straight ducts and then extended to allow higher order mode propagation in the connecting ducts.

The method developed in Chapter III is then used in Chapter IV to predict the transmission and reflection characteristics of several duct bends and junctions. The effect of different geometries and flow at low Mach number is considered.

Concluding remarks and further potential research directions are considered in Chapter V.

CHAPTER II

ISOHERM32 ELEMENT DEVELOPMENT

2.1 Choosing the Element

In the duct network research discussed in Section 1.3, two-dimensional linear and quadratic isoparametric C^0 elements were used. No more than two quadratic elements could be used across the cross-section of typical duct bends or junctions, within a small network, if the program was to operate on a desk top computer (an HP9816) with one megabyte of memory. It was found that this was just borderline in achieving sufficient accuracy up to the cut-on frequency for the first cross mode propagation in straight duct sections of the network. The present work was aimed at investigating sound propagation in duct system components up to frequencies above the cut-on of the first cross mode, while still using a desk top computer. Thus it was hoped that a more efficient element could be developed to minimize computer memory requirements and increase computation speed. It was anticipated that this could be done by using a higher order element which would lead to a reduced number of global degrees of freedom (DOF) in the finite element models, while hopefully still maintaining acceptable accuracy of predictions.

As discussed in Section 1.2.2, rectangular brick elements, using cubic Hermitian interpolation polynomials in two-dimensional and three-dimensional forms, have been used in acoustics by several researchers, for example, [17], [22] and [58] and found to give accurate results and high rates of convergence as the number of

elements was increased [54]. In this element, which has C^1 continuity, the dependent variable and its spatial derivatives were used as corner nodal quantities. The three-dimensional version of this cubic rectangular brick element will subsequently be referred to as HERM32 and has 32 DOF. This element is limited to modeling rectangular geometries or to use in combination with other types of elements for modeling more complex geometries.

Isoparametric elements with Serendipity shape functions, using just the dependent variable as a nodal quantity, have been used extensively in many fields and have been used in acoustics by, for example, [2], [3], [6], [13], [20], [21], [36], [45], and [51]. This type of element is useful for modeling complex geometries since the boundaries of the parent elements can be distorted to approximate curved surfaces. This element has C^0 continuity. The three-dimensional, cubic version of the isoparametric hexahedral element using Serendipity shape functions, will subsequently be referred to as HEX32 and has 32 DOF. In the current work, for comparison purposes some results have been obtained with the three-dimensional hexahedral isoparametric element which uses linear Serendipity polynomials. This element has eight DOF and will subsequently be referred to as the HEX8 element.

Although both the HERM32 and HEX32 elements discussed above use cubic interpolation functions and have 32 element DOF, the HERM32 element gives a reduction of global DOF compared to the HEX32 element by two means:

- All nodes are at the corners of the HERM32 element which gives fewer global DOF when the elements are linked to form the global model.
- If at the boundaries of the model, the normal gradient of the dependent variable is specified, then nodal derivative quantities can be constrained. In hard walled ducts, for example, the normal acoustic velocity and the

normal acoustic pressure gradient at the duct surface are zero. In cases where the acoustic velocity potential or pressure are used as the dependent variable, the global DOF of the HERM32 model can be reduced by applying constraint equations to the nodal derivative quantities.

It was anticipated that this feature of the HERM32 element could be incorporated with the HEX32 element's distortion capability by developing a new isoparametric element using cubic Hermitian polynomials in conjunction with transformations which allow distortion of the parent element to model curved boundaries. This proposed element will be referred to subsequently as ISOHERM32.

The mathematical development of the proposed element shape functions and geometric transformation is considered in the next section. This is followed by sections concerning testing of the element—first for the acoustic eigenvalue problem in Section 2.3 and then for the incompressible potential flow problem in Section 2.4.

2.2 Element Shape Functions and Geometric Transformation

This section primarily discusses the development of the interpolation functions used within the ISOHERM32 element, the element isoparametric geometric transformation and continuity between elements. Development of the global finite element model equations is left to subsequent sections discussing particular applications.

2.2.1 Equation Development

The parent element used is a cube in local element coordinates ξ, γ, ζ which transforms to a general hexahedron in the global x, y, z coordinates as shown in Figure 2.1a. The basic shape functions employed in each dimension are cubic Hermite polynomials in the interval -1 to 1 given by

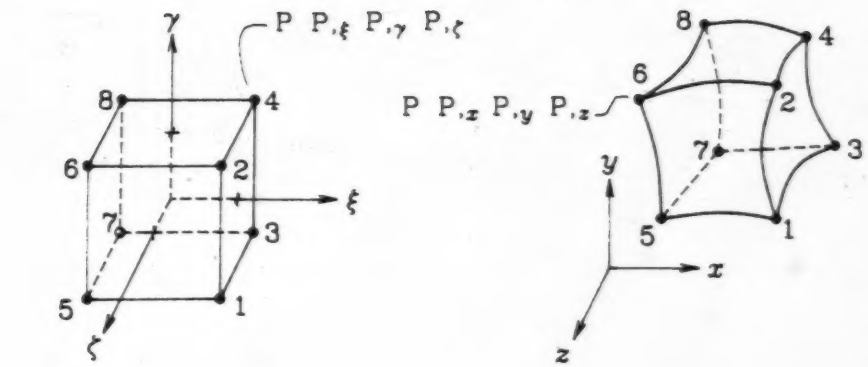

Local Element Coordinates
(ξ,γ,ζ)

Global Coordinates
(x,y,z)

a) Dependent variable nodes

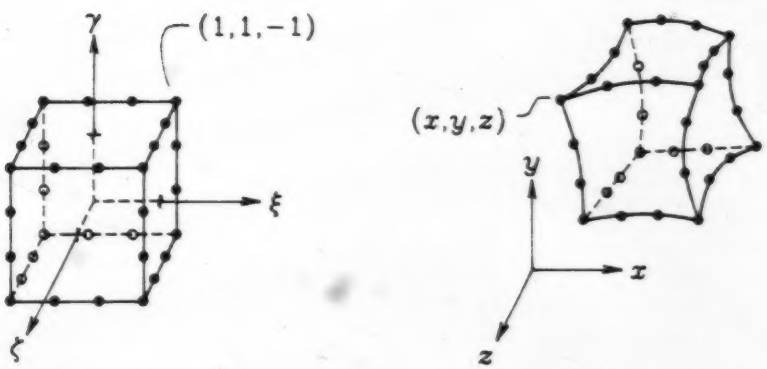

Local Element Coordinates

Global Coordinates

b) Geometric Nodes

Figure 2.1 The ISOHERM32 Finite Element

$$
\begin{aligned}
f_1(\eta) &= \tfrac{1}{2} - \tfrac{3}{4}\eta + \tfrac{1}{4}\eta^3 \\
f_2(\eta) &= \tfrac{1}{4} - \tfrac{1}{4}\eta - \tfrac{1}{4}\eta^2 + \tfrac{1}{4}\eta^3 \\
f_3(\eta) &= \tfrac{1}{2} + \tfrac{3}{4}\eta - \tfrac{1}{4}\eta^3 \\
f_4(\eta) &= -\tfrac{1}{4} - \tfrac{1}{4}\eta + \tfrac{1}{4}\eta^2 + \tfrac{1}{4}\eta^3
\end{aligned}
\tag{2.1}
$$

and have the following properties:

i	$f_i(-1)$	$f_i(1)$	$\frac{d}{d\eta}f_i(-1)$	$\frac{d}{d\eta}f_i(1)$
1	1	0	0	0
2	0	0	1	0
3	0	1	0	0
4	0	0	0	1

The value of the dependent variable P at a point (ξ, γ, ζ) in the element can then be obtained from

$$P(\xi, \gamma, \zeta) = \langle F \rangle \{P_e\} \tag{2.2}$$

where the i^{th} element of $\langle F \rangle$ is

$$F_i(\xi, \gamma, \zeta) = f_{l_i}(\xi)\, f_{m_i}(\gamma)\, f_{n_i}(\zeta) \tag{2.3}$$

and the 32 element row vector of corner node quantities $\{P_e\}^T$ is given by

$$\langle P_e \rangle = \left\langle P_1, \frac{\partial P_1}{\partial \xi}, \frac{\partial P_1}{\partial \gamma}, \frac{\partial P_1}{\partial \zeta}, P_2, \frac{\partial P_2}{\partial \xi}, \frac{\partial P_2}{\partial \gamma}, \frac{\partial P_2}{\partial \zeta}, \cdots, P_8, \frac{\partial P_8}{\partial \xi}, \frac{\partial P_8}{\partial \gamma}, \frac{\partial P_8}{\partial \zeta} \right\rangle. \tag{2.4}$$

The subscripts 1 to 8 refer to the eight corner nodes shown in Figure 2.1a. The values of l_i, m_i, n_i in the i^{th} element of $\langle F \rangle$ are chosen so that $P(\xi, \gamma, \zeta)$, $\partial P/\partial \xi$, $\partial P/\partial \gamma$, and $\partial P/\partial \zeta$ give the corner nodal quantities when evaluated at each corner. The following algorithm is used to set up the matrix of l, m and n values in the computer program for each corner node (the corner coordinate values are either 1 or -1):

- if $\xi = 1$ then $l = 3$ else $l = 1$ except if the element F_i is multiplied by a $\partial P/\partial \xi$ term then if $\xi = 1$ then $l = 2$ else $l = 4$

- similarly the γ and ζ coordinates are compared to select the m and n values of either 1 or 3 except when multiplied by $\partial P/\partial\gamma$ or $\partial P/\partial\zeta$ terms, respectively, in which case a value of 2 or 4 is selected.

The independent variable P is given in Equation 2.2 in terms of the corner nodal quantities $\{P_e\}$ which contain derivatives with respect to the element coordinates. The global nodal quantities are, however, in terms of derivatives with respect to the global coordinates. Let the vector of global nodal quantities $\{P_g\}$ be defined as

$$\langle P_g \rangle = \left\langle P_1, \frac{\partial P_1}{\partial x}, \frac{\partial P_1}{\partial y}, \frac{\partial P_1}{\partial z}, P_2, \frac{\partial P_2}{\partial x}, \frac{\partial P_2}{\partial y}, \frac{\partial P_2}{\partial z}, \cdots, P_8, \frac{\partial P_8}{\partial x}, \frac{\partial P_8}{\partial y}, \frac{\partial P_8}{\partial z} \right\rangle . \quad (2.5)$$

Then, as a function of the global nodal quantities, P is obtained from

$$P(\xi, \gamma, \zeta) = \langle N \rangle \{P_g\} \quad (2.6)$$

where

$$\langle N \rangle = \langle F \rangle [J_g] \quad (2.7)$$

and $[J_g]$ is a 32 by 32 matrix given by

$$[J_g] = \begin{bmatrix} 1 & & & & & & & \\ & [J]_1 & & & & \mathrm{O} & & \\ & & 1 & & & & & \\ & & & [J]_2 & & & & \\ & \mathrm{O} & & & \ddots & & & \\ & & & & & & [J]_8 & \end{bmatrix} . \quad (2.8)$$

All off-diagonal elements outside the $[J]_k$ sub-matrices are zeros. The sub-matrix $[J]_k$ is the Jacobian matrix of the transformation evaluated at the corner node k where the Jacobian matrix $[J]$ is defined by

$$[J] = \begin{bmatrix} \frac{\partial x}{\partial \xi} & \frac{\partial y}{\partial \xi} & \frac{\partial z}{\partial \xi} \\ \frac{\partial x}{\partial \gamma} & \frac{\partial y}{\partial \gamma} & \frac{\partial z}{\partial \gamma} \\ \frac{\partial x}{\partial \zeta} & \frac{\partial y}{\partial \zeta} & \frac{\partial z}{\partial \zeta} \end{bmatrix} . \quad (2.9)$$

The Jacobian matrix is dependent on the transformation between the global and element domains. The parent cube element is transformed to a hexahedral in the global coordinate domain using the same Hermite polynomial shape functions as used for the element dependent variable interpolation. The coordinate interpolation is given by

$$\langle x \quad y \quad z \rangle = \langle F \rangle [XYZ]_e \tag{2.10}$$

where $[XYZ]_e$ is the matrix of corner node coordinates and derivative quantities defined as

$$[XYZ]_e = \begin{bmatrix} x_1 & y_1 & z_1 \\ & [J]_1 & \\ x_2 & y_2 & z_2 \\ & [J]_2 & \\ & \vdots & \\ x_8 & y_8 & z_8 \\ & [J]_8 & \end{bmatrix}. \tag{2.11}$$

The corner Jacobian matrix values are not explicitly assigned. The actual hexahedral geometry is defined in terms of the corner coordinates and two additional points equally spaced along each edge of the element, the 32 geometric "G" nodes show in Figure 2.1b. Evaluating Equation 2.10 at each of the 32 "G" nodes gives the following matrix equation

$$[XYZ] = [FF][XYZ]_e \tag{2.12}$$

where $[XYZ]$ is the known matrix of coordinates of the 32 "G" nodes expanded as

$$[XYZ] = \begin{bmatrix} x_1 & y_1 & z_1 \\ x_2 & y_2 & z_2 \\ x_3 & y_3 & z_3 \\ \vdots & \vdots & \vdots \\ x_{32} & y_{32} & z_{32} \end{bmatrix} \tag{2.13}$$

and $[FF]$ is the matrix of shape functions $\langle F \rangle$ evaluated at each of the 32 "G" nodes

and written as

$$[FF] = \begin{bmatrix} \langle F \rangle_1 \\ \langle F \rangle_2 \\ \langle F \rangle_3 \\ \vdots \\ \langle F \rangle_{31} \\ \langle F \rangle_{32} \end{bmatrix}. \tag{2.14}$$

The matrix of corner node quantities $[XYZ]_e$ is then obtained by solving Equation 2.12 to give

$$[XYZ]_e = [FF]^{-1}[XYZ]. \tag{2.15}$$

Note that the matrix $[FF]^{-1}$ is only dependent on the parent element geometry and thus the inversion need only be evaluated once and used for all finite elements in the global model.

Substituting this result in Equation 2.10 gives the following interpolation for the global coordinates within the element

$$\langle x \quad y \quad z \rangle = \langle F \rangle [FF]^{-1}[XYZ]. \tag{2.16}$$

The Jacobian matrix can be obtained by differentiating this equation with respect to each of the element coordinates to give

$$[J] = [M][FF]^{-1}[XYZ] \tag{2.17}$$

where

$$[M] = \begin{bmatrix} \frac{\partial}{\partial \xi}\langle F \rangle \\ \frac{\partial}{\partial \gamma}\langle F \rangle \\ \frac{\partial}{\partial \zeta}\langle F \rangle \end{bmatrix}. \tag{2.18}$$

The term $\nabla\{F\} \bullet \nabla\langle F \rangle$ in the global system of coordinates is used later in the development of the FEM model equations and can be obtained from

$$\nabla\{F\} \bullet \nabla\langle F \rangle = \begin{bmatrix} \frac{\partial}{\partial x}\langle F \rangle \\ \frac{\partial}{\partial y}\langle F \rangle \\ \frac{\partial}{\partial z}\langle F \rangle \end{bmatrix}^T \begin{bmatrix} \frac{\partial}{\partial x}\langle F \rangle \\ \frac{\partial}{\partial y}\langle F \rangle \\ \frac{\partial}{\partial z}\langle F \rangle \end{bmatrix}. \tag{2.19}$$

Substituting

$$\begin{bmatrix} \frac{\partial}{\partial x}\langle F\rangle \\ \frac{\partial}{\partial y}\langle F\rangle \\ \frac{\partial}{\partial z}\langle F\rangle \end{bmatrix} = \left[J^{-1}\right][M] \tag{2.20}$$

where $\left[J^{-1}\right]$ is the inverse of $[J]$ gives the following equation

$$\nabla\{F\} \bullet \nabla\langle F\rangle = [M]^T\left[J^{-1}\right]^T\left[J^{-1}\right][M]. \tag{2.21}$$

Subparametric versions of the element using linear and quadratic Serendipity shape functions for the geometric transformation were also formulated. It was found that the assembly procedure with the isoparametric version was actually faster since this involved calculation of only one set of shape functions for both the dependent variable and the geometry.

2.2.2 Continuity Between Elements

The partial differential equations encountered in this work are of second order and a sufficient condition for convergence of the finite element solution is that the elements satisfy certain continuity and completeness criteria [8]. For second order differential equations the continuity condition states that only the dependent variable P must be continuous across the element boundaries. Thus it is sufficient to use a C^0 element such as the HEX32 element. The completeness condition for a second order differential equation states that at least a linear polynomial should be used for the element shape functions.

The rectangular brick HERM32 element discussed in section 2.1 has C^1 continuity, which means that the independent variable P and components of the gradient of P are continuous across element boundaries. The proposed ISOHERM32 element gives C^1 continuity at the corner nodes but generally has only C^0 continuity along element boundaries. It can be shown that the 1st partial spatial derivatives

of P tangential to the element boundary are dependent only on nodal quantities on the connecting boundary and are thus continuous. The normal gradient depends also on geometric coordinates of points not on the element boundary and is thus not generally continuous. In the special case that adjoining elements are rectangular (basically the HERM32 element) then C^1 continuity is achieved across element boundaries. Also it was observed that if the elements formed segments of a polar grid, then C^1 continuity was also achieved across element boundaries. This may apply to other configurations where elements have similar shapes and may warrant further investigation.

2.2.3 The ISOHERM12 Element

The computational models used in this thesis have been implemented on a desk top computer and it has been found that even with a more efficient element, some of the problems could only be handled in two dimensions and certainly computed much faster using two rather than three dimensional models. For these reasons, a two dimensional version of the ISOHERM32 element has also been programmed. This quadrilateral element has four corner nodes with three DOF at each corner—the dependent variable P and the spatial derivatives $\partial P/\partial x$ and $\partial P/\partial y$. This element thus has twelve DOF and will subsequently be referred to as ISOHERM12.

The mathematical formulation of this element is identical to that of the ISOHERM32 element with the exception that the shape functions are now a product of two, rather than three, one-dimensional Hermite polynomials and the element coordinates, derivatives, the Jacobian matrix and other matrices are given in two dimensions (ξ, γ) and (x, y). All quantities are taken to have no variation in the z direction.

2.3 Testing the Element: The Acoustic Eigenvalue Problem

The first test of the new element was to predict the acoustic resonant frequencies of a stationary compressible fluid within a rigid walled cavity for which the exact solution was known. Later, when looking at higher order mode propagation through duct bends and junctions, this type of problem is solved to find eigenfrequencies and mode shapes for connecting straight duct cross-sections.

2.3.1 Equation Development

The governing differential equation is the Helmholtz equation which can be derived starting from the equation for small amplitude wave propagation in a stationary inviscid isentropic compressible medium. In terms of the acoustic pressure (the non-steady pressure component) the wave equation is

$$\frac{\partial^2 p}{\partial t^2} - c^2 \nabla^2 p = 0 \tag{2.22}$$

where c is the speed of sound. The acoustic particle velocity can be related to the pressure gradient by

$$\frac{\partial \mathbf{u}}{\partial t} = -\frac{1}{\rho} \nabla p. \tag{2.23}$$

A harmonic time dependence $e^{i\omega t}$ is assumed so that the acoustic pressure p and particle velocity $\mathbf{u}$ are then given by

$$p = P e^{i\omega t} \quad \text{and} \quad \mathbf{u} = \mathbf{U} e^{i\omega t} \tag{2.24}$$

where ω is the angular frequency and t the time variable. Substituting this into Equation 2.22 leads to the Helmholtz equation

$$\nabla^2 P + k^2 P = 0 \tag{2.25}$$

and the particle velocity **U** given by

$$\mathbf{U} = \frac{\mathrm{i}\nabla P}{\omega\rho} = \frac{\mathrm{i}\nabla P}{k(\rho c)} \tag{2.26}$$

where the wave number $k = \omega/c$ and ρ is the density of the stationary medium. If the cavity has rigid walls then the velocity normal to the wall is zero and from Equation 2.26 the normal acoustic pressure gradient at the wall is also zero.

The Galerkin method [8] was used to develop the finite element formulation. For this problem an energy functional exists which can be used with the Ritz variational method to give the same finite element formulation. If the approximate finite element solution $\tilde{P}$ is substituted into the governing differential Equation 2.25 then the residual error R becomes

$$R = \nabla^2\tilde{P} + k^2\tilde{P}. \tag{2.27}$$

In the Galerkin method this error is minimized by making R orthogonal to the finite element model shape functions over the volume of the acoustic cavity according to the equation

$$\iiint_V \{N\}\left(\nabla^2\tilde{P} + k^2\tilde{P}\right)\,dv = \{0\}. \tag{2.28}$$

The order of the first term is then reduced by using Green's first identity to give

$$\iint_S \{N\}\frac{d\tilde{P}}{dn}\,ds - \iiint_V \nabla\{N\}\bullet\nabla\tilde{P}\,dv + k^2\iiint_V \{N\}\tilde{P}\,dv = \{0\}. \tag{2.29}$$

The normal derivative $d\tilde{P}/dn$ at the rigid walls of the cavity is zero so the surface area term drops out of the equation. The actual integrations are calculated on an element basis. Although the surface integral flux terms are not zero, surface terms from adjacent elements cancel since the normals are in opposite directions.

Substituting for $\tilde{P}$ using Equation 2.6 gives the equation

$$\iiint_V \left(\nabla\{N\} \bullet \nabla\langle N\rangle - k^2\{N\}\langle N\rangle\right) dv \, \{P_g\} = \{0\}. \tag{2.30}$$

This equation is integrated on an element basis and then assembled into a global matrix equation. The element equivalent "stiffness" matrix $[S_e]$ is defined as

$$\begin{aligned}[S_e] &= \iiint_{V_e} \nabla\{N\} \bullet \nabla\langle N\rangle \, dx\, dy\, dz \\ &= \iiint_{V_e} [J_g]^T \nabla\{F\} \bullet \nabla\langle F\rangle \, [J_g] \, dx\, dy\, dz\end{aligned} \tag{2.31}$$

which when substituting for $\nabla\{F\} \bullet \nabla\langle F\rangle$ using Equation 2.21 and integrating in the element coordinate system gives

$$[S_e] = [J_g]^T \int_{-1}^{1}\int_{-1}^{1}\int_{-1}^{1} [M]^T \left[J^{-1}\right]^T \left[J^{-1}\right] [M] \, |J| \, d\xi \, d\gamma \, d\zeta \, [J_g]. \tag{2.32}$$

The element equivalent "mass" matrix $[P_e]$ is defined by

$$[P_e] = \iiint_{V_e} \{N\}\langle N\rangle \, dx\, dy\, dz \tag{2.33}$$

which, integrated over the element volume, gives

$$[P_e] = [J_g]^T \int_{-1}^{1}\int_{-1}^{1}\int_{-1}^{1} \{F\}\langle F\rangle \, |J| \, d\xi \, d\gamma \, d\zeta \, [J_g]. \tag{2.34}$$

The element integrations were carried out using Gauss-Legendre quadrature, see for example [8]. Four Gauss points were used in each dimension thus requiring evaluation at 64 points within a three-dimensional element. The resulting equations used to calculate the element matrices $[S_e]$ and $[P_e]$ are given by

$$\begin{aligned}[S_e] &= [J_g]^T \left(\sum_{k=1}^{4}\sum_{l=1}^{4}\sum_{m=1}^{4} w_k \, w_l \, w_m \left([M]^T \left[J^{-1}\right]^T \left[J^{-1}\right] [M] \, |J| \right)_{(\xi_k, \gamma_l, \zeta_m)} \right) [J_g] \\ [P_e] &= [J_g]^T \left(\sum_{k=1}^{4}\sum_{l=1}^{4}\sum_{m=1}^{4} w_k \, w_l \, w_m \left(\{F\}\langle F\rangle \, |J| \right)_{(\xi_k, \gamma_l, \zeta_m)} \right) [J_g]\end{aligned} \tag{2.35}$$

where

$$\begin{aligned}
\xi_1, \gamma_1, \zeta_1 &= -\frac{\sqrt{15+2\sqrt{30}}}{\sqrt{35}} & w_1 &= \frac{49}{6\left(18+\sqrt{30}\right)} \\
\xi_2, \gamma_2, \zeta_2 &= -\frac{\sqrt{15-2\sqrt{30}}}{\sqrt{35}} & w_2 &= \frac{49}{6\left(18-\sqrt{30}\right)} \\
\xi_3, \gamma_3, \zeta_3 &= +\frac{\sqrt{15-2\sqrt{30}}}{\sqrt{35}} & w_3 &= \frac{49}{6\left(18-\sqrt{30}\right)} \\
\xi_4, \gamma_4, \zeta_4 &= +\frac{\sqrt{15+2\sqrt{30}}}{\sqrt{35}} & w_4 &= \frac{49}{6\left(18+\sqrt{30}\right)}
\end{aligned} \tag{2.36}$$

The element matrices for all elements in the acoustic cavity volume are assembled into a global matrix equation

$$\left([S] - k^2[P]\right)\{P_g\} = \{0\} \tag{2.37}$$

using the classical finite element assembly procedure [8].

This is an eigenvalue problem in which nontrivial solutions exist for values of k^2 which satisfy the equation

$$\det\left|[S] - k^2[P]\right| = 0. \tag{2.38}$$

At this point, using the hard wall boundary condition, the pressure gradient terms of $\{P_g\}$ at nodes on the boundary can be constrained to force the normal derivative of the acoustic pressure at these nodes equal to zero. If the wall is parallel to one of the global axes then the appropriate elements of $\{P_g\}$ can be set to zero.

When setting up the finite element model, all "zero" nodal quantities are assigned to the last element of $\{P_g\}$. Then in the element matrix assembly, terms contributing to the last row and column of $[S]$ and $[P]$ are ignored. If the boundary is curved or sloped, for example, in the x–y plane then the values of $\partial P/\partial x$ and $\partial P/\partial y$ at a node on the plane can be related by a linear constraint equation. A series of symmetric row and column operations can be used to eliminate the row

and column of $[S]$ and $[P]$ corresponding to one of these quantities, refer to [8], Chapter 4. In this manner, the sizes of the $[S]$ and $[P]$ matrices can be reduced before solving the eigenvalue problem given by Equation 2.37.

2.3.2 Modeling A Rectangular Enclosure

The first test of the undistorted element was to model a three-dimensional rigid walled rectangular enclosure. The exact solution for the eigenvalues in terms of the wave number k from [41] is

$$k = \pi \sqrt{\left(\frac{n_x}{l_x}\right)^2 + \left(\frac{n_y}{l_y}\right)^2 + \left(\frac{n_z}{l_z}\right)^2} \tag{2.39}$$

where n_x, n_y,and n_z are any integers and the dimensions of the enclosure are l_x, l_y and l_z. This can be expressed in terms of dimensionless parameters by

$$ka = \pi \sqrt{(n_x)^2 + \left(\frac{n_y}{r_y}\right)^2 + \left(\frac{n_z}{r_z}\right)^2} \tag{2.40}$$

where $l_x = a$, $r_y = l_y/a$ and $r_z = l_z/a$.

2.3.2.1 Model with One Element

A rectangular cavity with $r_y = 0.6$ and $r_z = 0.8$ was modeled using one ISOHERM32 element, and for comparison, one HEX32 element. Both elements have 32 DOF and can be used in a single element global model having 32 global DOF. The ISOHERM32 element, having nodal quantities in terms of the pressure gradient, can be constrained by explicitly satisfying the hard wall boundary condition at the corner nodes. Setting the components of the pressure gradient to zero at the corner nodes gives a global model with only 8 DOF. An additional comparison was made with a single HEX8 element which also gives a global model with 8 DOF.

The exact values of ka given by Equation 2.40 and the prediction errors for the four models are given in Table 2.1.

The modes are numbered in ascending numerical order in terms of the exact values of ka. Note that above the 16^{th} mode, many of the modes are missing, and not predicted with this model. The number of modes predicted by a given model (including the rigid body mode for which $ka = 0$) is equal to the global DOF.

The models gave values of ka for the first mode (rigid body mode) of approximately $ka = 10^{-7}$. Both 32 DOF models, the ISOHERM32 model unconstrained and HEX32 model, predicted the resonant frequency for the axial modes $[1,0,0]$, $[0,1,0]$ and $[0,0,1]$ with an error of 0.028 percent. The ISOHERM32 model predicted all the first order modes (n_x, n_y and n_z less than or equal one) with an error of 0.028 percent. However, with the HEX32 model, the error for the first tangential modes $[0,1,1]$, $[1,0,1]$ and $[1,1,0]$ was six times that for the first axial modes and the error for the first oblique mode $[1,1,1]$ was 0.296 percent, a factor of ten larger than the ISOHERM32 model error.

Errors for higher order modes were several hundred times larger than for the first order modes. The ISOHERM32 model unconstrained and the HEX32 model gave identical results for the higher order axial modes but the HEX32 model gave larger errors than the ISOHERM32 model for the tangential and oblique modes.

The ISOHERM32 model constrained and the HEX8 model, both having 8 DOF, predicted only the rigid body mode and the seven first order modes. The error in predicting all the first order modes was 0.064 percent with the ISOHERM32 model and 10.27 percent with the HEX8 model.

Table 2.1 Eigenvalues for a Rectangular Rigid Walled Box with Dimensions $l_x = a$, $l_y = 0.6a$ and $l_z = 0.8a$, Modeled with One Element

Mode No.	n_x	n_y	n_z	Exact ka	Percent Error			
					ISOHERM32		HEX32	HEX8
					con.	uncon.		
0	0	0	0	0.000				
1	1	0	0	3.142	0.0646	0.0278	0.0278	10.27
2	0	0	1	3.927	0.0646	0.0278	0.0278	10.27
3	1	0	1	5.029	0.0646	0.0278	0.1664	10.27
4	0	1	0	5.236	0.0646	0.0278	0.0278	10.27
5	1	1	0	6.106	0.0646	0.0278	0.1648	10.27
6	2	0	0	6.283		23.28	23.28	
7	0	1	1	6.545	0.0646	0.0278	0.1662	10.27
8	1	1	1	7.260	0.0646	0.0278	0.2960	10.27
9	2	0	1	7.409		17.22	19.77	
10	0	0	2	7.854		23.28	23.28	
11	2	1	0	8.179		14.34	18.38	
12	1	0	2	8.459		20.35	21.57	
13	2	1	1	9.073		11.80	16.69	
14	3	0	0	9.425		38.39	38.39	
15	0	1	2	9.439		16.63	19.43	
16	1	1	2	9.948		15.09	18.55	
18	3	0	1	10.210		33.42	34.56	
19	0	2	0	10.472		23.28	23.28	
20	3	1	0	10.782		30.37	32.26	
21	1	2	0	10.933		21.53	22.26	
22	0	2	1	11.184		20.66	21.75	
24	3	1	1	11.474		27.20	29.85	
25	1	2	1	11.617		12.65	20.95	
26	0	0	3	11.781		38.39	38.39	
27	1	0	3	12.193		36.18	36.72	
32	0	1	3	12.892		32.84	34.12	
35	1	1	3	13.269		31.21	32.91	
48	0	3	0	15.708		38.39	38.39	
54	1	3	0	16.019		37.12	37.42	
57	0	3	1	16.191		36.44	36.91	
60	1	3	1	16.493		35.29	36.03	

It is significant to note that in the constrained ISOHERM32 model with 8 DOF, the errors were only a factor of 2.3 times those of the unconstrained model with 32 DOF and still less than 0.1 percent. Also, in terms of computing time, the 32 DOF eigenvalue problem took 60 times longer than the 8 DOF problem . This indicates the advantages the new element may have for low frequency modeling of a duct system or component in three dimensions, while modeling the rectangular duct cross-section using one constrained ISOHERM32 element. This would give only 8 DOF per duct element compared to 20 DOF using a HEX32 element and still predict the frequencies of the $[0,1]$, $[1,0]$ and $[1,1]$ cross modes with less than 0.1 percent error.

It is interesting to note that the ISOHERM32 element gave the same error for all first order axial, tangential and oblique modes, while the HEX32 model gave significantly higher errors in the tangential and oblique modes. The solution to the governing differential equation for this problem is in separated variable form: similarly the shape functions for the ISOHERM32 element are a product of a Hermite polynomial in each dimension. The cubic Serendipity shape functions used in the HEX32 element are not in a separated variable form which probably explains the increased errors using this model to predict tangential and oblique modes.

2.3.2.2 Linking Several Elements in One Dimension

The convergence of the undistorted element was demonstrated by linking two to sixteen elements in a linear string along the x axis and constraining nodal values to give a one dimensional model of axial modes in a tube with rigid ends.

The convergence of the first five axial modes for the ISOHERM32 model is shown in Figure 2.2 where the logarithm to the base 10 of the percentage error in ka is plotted as a function of the global DOF. For a sufficiently large number

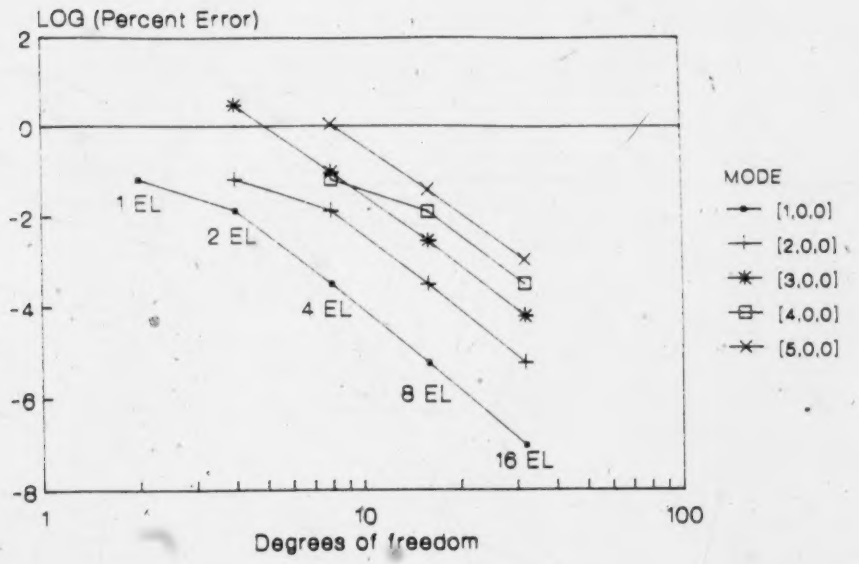

Figure 2.2 Convergence of the ISOHERM32 Element Models for the Prediction of the Eigenvalues for the Acoustic Modes in a One-dimensional Tube

of elements, the curves for all modes have close to the same slope, giving a rate of convergence proportional to between $1/\text{DOF}^5$ and $1/\text{DOF}^6$. Note, at the end of the string of elements, the hard wall boundary condition can be explicitly satisfied by constraining the dP/dx nodal quantity to zero in the ISOHERM32 model.

The errors for the first axial mode with the above model are compared to other element models in Figure 2.3. In this figure the legend text IH32C refers to the ISOHERM32 element model discussed above where the "C" refers to the constrained end nodes. The ISOHERM32 model was also run leaving the dP/dx nodal quantities at the ends of the tube unconstrained, referred to as IH32U in the figure. The HEX8 model shows much higher errors and a lower rate of convergence than the other three models. The other three models have similar errors and rates of convergence. On an element basis, the HEX32 model gives slightly better results

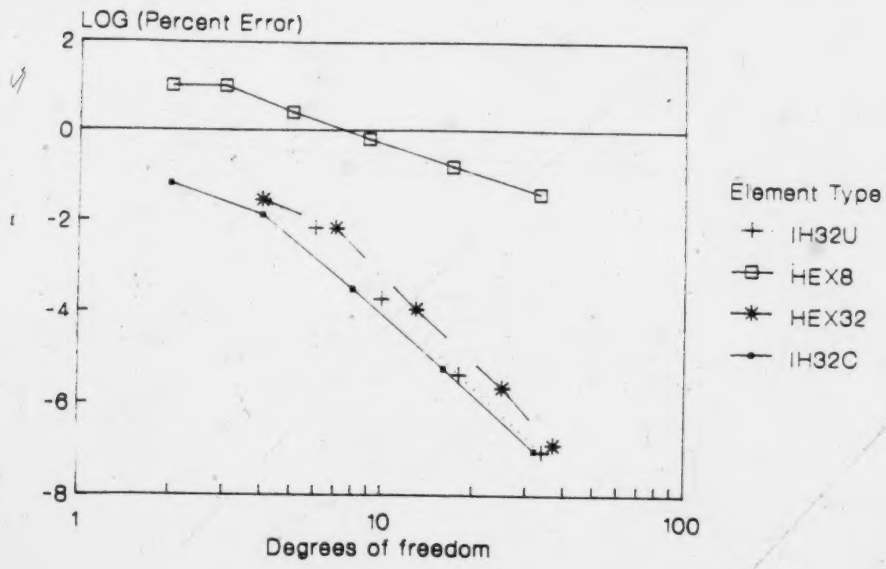

Figure 2.3 Convergence of Different FEM Models for the Prediction of the Eigenvalue for the Mode [1,0,0] in a One-dimensional Tube

than the ISOHERM32 models, but on a DOF basis, the constrained ISOHERM32 model is better with errors of typically 1/3 that obtained with the HEX32 model with a similar number of DOF.

The comparison of the different models for higher order modes is demonstrated in Figure 2.4, where ISOHERM32, HEX32 and HEX8 models with similar numbers of DOF are considered. Generally as the axial mode number is increased the error increased, with highest errors occurring with the HEX8 model. The HEX32 and ISOHERM32 models gave errors of five orders of magnitude smaller than the HEX8 model for the first axial mode but were only about one order of magnitude lower at the 16th mode. Comparing the ISOHERM32 and HEX32 models, both exhibited similar errors for the lowest mode, but the ISOHERM32 model gave progressively better results than the HEX32 model as the mode number was

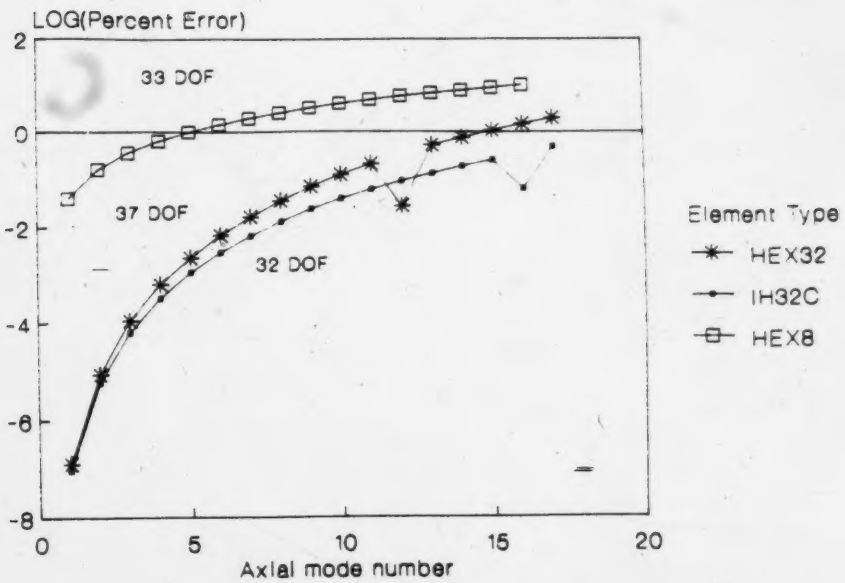

Figure 2.4 Convergence of Different FEM Models for the Prediction of the Eigenvalues for Higher Order Modes in a One-dimensional Tube

increased. The 12th mode and 16th mode for the ISOHERM32 and HEX32 elements respectively had smaller errors than the adjacent modes creating the notches in the graphs. These occurred when each element modeled exactly 1/2 wavelength.

2.3.2.3 Distortion of the Elements within a Rectangular Enclosure

The previous sections have looked at cases in which the elements are undistorted and maintained the shape of the parent cuboid elements. For these cases the ISOHERM32 element formulation reduced to that for the non-distortable HERM32 brick element. As an initial distorted-element test, the rectangular enclosure modeled in Section 2.3.2.1 with one element was modeled with two elements side by side along the x-axis. The eigenvalues ka were then predicted for various degrees of rotation and twisting of the common plane between the two elements as

Table 2.2 Eigenvalues for a Two-element Box of Dimensions $l_x = a$, $l_y = 0.6a$ and $l_z = 0.8a$ with the Common Plane Rotated

Mode No.	n_x	n_y	n_z	Percent Error in ka				
				Rotation angle in degrees				
				0	15	30	45	59
1	1	0	0	0.0130	0.0313	0.1439	0.7071	3.668
2	0	0	1	0.0646	0.0646	0.0646	0.0646	0.0646
3	1	0	1	0.0445	0.0516	0.0955	0.3158	1.486
4	0	1	0	0.0646	0.0639	0.0620	0.0593	0.0573
5	1	1	0	0.0509	0.2975	1.269	4.177	13.49
6	2	0	0	0.0646	0.3444	2.358	10.89	50.15
7	0	1	1	0.0646	0.0641	0.0629	0.0612	0.0599
8	1	1	1	0.0549	0.2294	0.9184	2.991	9.732
9	2	0	1	0.0646	6.2659	1.717	7.958	37.93
11	2	1	0	0.0646	1.333	5.919	17.25	43.86
13	2	1	1	0.0649	1.096	4.847	14.23	36.72
14	3	0	0	3.008	5.305	13.75	37.12	156.4
18	3	0	1	2.578	4.546	11.83	32.29	139.8
20	3	1	0	2.322	5.654	16.16	38.29	124.6
24	3	1	1	2.060	5.014	14.39	34.37	113.8

shown in Figure 2.5.

At each corner of the box the nodal quantities $\partial P/\partial x$, $\partial P/\partial y$ and $\partial P/\partial z$ were constrained to zero and also at the nodes common to both elements on the edges of the box the derivatives $\partial P/\partial y$ and $\partial P/\partial z$ were constrained to zero resulting in a 16 DOF ISOHERM32 model. This is a very significant reduction in DOF compared to 52 DOF if run using a HEX32 model and 48 DOF for the ISOHERM32 model unconstrained.

The results obtained for the rotation of the common plane between the two elements are given in Table 2.2. The results for twisting of this plane are given in Table 2.3. The angle of rotation β was taken with respect to the vertical $y-$axis. For the twisting of the common plane, the front edge of the plane was rotated clockwise

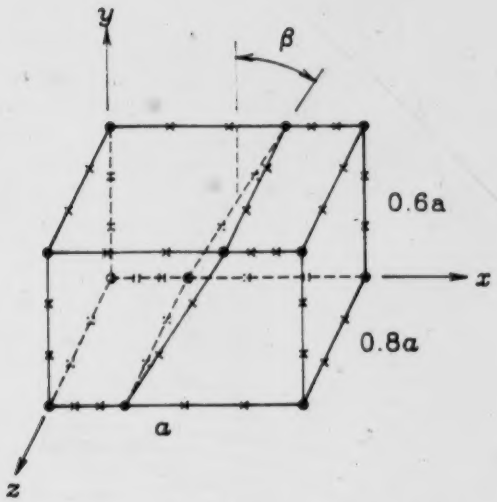

Rotation of the common plane

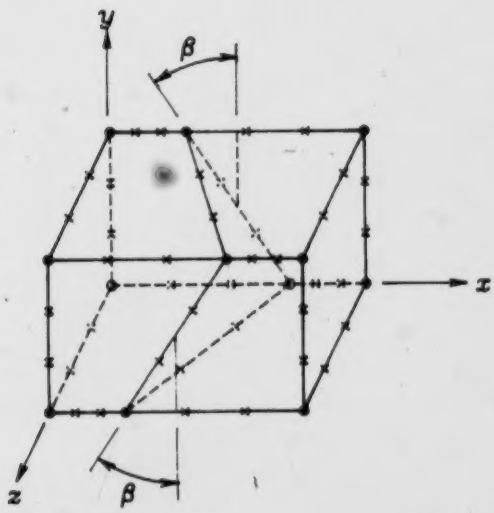

Twisting of the common plane

Figure 2.5 Element Distortion Within a Two-element Box

Table 2.3 Eigenvalues for a Two-element Box of Dimensions $l_x = a$, $l_y = 0.6a$ and $l_z = 0.8a$ with the Common Plane Twisted

Mode No.	n_x	n_y	n_z	Percent Error in ka				
				Rotation angle in degrees				
				0	15	30	45	59
1	1	0	0	0.0130	1.405	4.859	9.572	16.35
2	0	0	1	0.0646	0.0640	0.0627	0.0615	0.0611
3	1	0	1	0.0445	0.6566	2.233	4.942	11.16
4	0	1	0	0.0646	0.0634	0.0608	0.0562	0.0577
5	1	1	0	0.0509	0.7616	2.495	4.987	9.848
6	2	0	0	0.0646	0.3193	1.851	6.685	17.36
7	0	1	1	0.0646	0.0637	0.0631	0.0569	0.0598
8	1	1	1	0.0549	0.7048	2.374	5.898	20.08
9	2	0	1	0.0646	0.1232	1.183	4.754	14.68
11	2	1	0	0.0646	0.1229	1.121	4.293	14.52
13	2	1	1	0.0649	0.8284	3.693	11.55	38.59
14	3	0	0	3.008	3.366	8.658	20.04	38.70
18	3	0	1	2.578	5.560	13.60	28.68	67.79
20	3	1	0	2.322	6.577	18.73	33.97	94.71
24	3	1	1	2.060	4.519	13.78	41.10	122.8

by an angle β and the back edge of the plane was rotated counterclockwise by the same angle. An angle of 59 degrees brings the common plane almost to the corners of the box. For the case of rotation of the plane, this collapses one face of each element to a line, thus forming two wedge shape elements. The model gives results for the modes with $n_x = 1, 2, 3$ and $n_y = 1$ and $n_z = 1$.

Undistorted, the errors for the first eleven of the 15 predicted modes of 1st or 2nd order were less than 0.065 percent. The errors for the remaining four 3rd order modes ranged from 2.1 percent for the $[3,1,1]$ mode to 3 percent for the $[3,0,0]$ axial mode. The eigenvalues for the modes with $n_x = 0$ are virtually unaffected by these distortions. For the case of plane rotation, the $[0,0,1]$ mode is completely unaffected which is reasonable since the distortion is in the $x-y$ plane only. The errors in the $[0,1,0]$ and the $[0,1,1]$ modes actually decrease slightly as

the distortion is increased. For the undistorted case, each of the coordinates x, y or z is linearly related to one of the parent element coordinates ξ, γ or ζ. If the plane is rotated, in the transformation, the coordinate x becomes a linear function of both ξ and γ, however the transformation for y and z remain unchanged. This may explain why modes involving only the y and z directions are unchanged.

Comparing the rotational and twisting distortion, the most striking difference is the effect on the $[1,0,0]$ axial mode. This is shown in Figure 2.6. For the $[2,0,0]$ and $[3,0,0]$ modes, the rotation of the plane causes larger errors than twisting. However, the $[1,0,0]$ axial mode appears to be very sensitive to the twisting distortion with errors rapidly increasing to 10 to 50 times that for rotation of the plane, for angles between 5 and 15 degrees, and in fact becoming larger than the errors for the [2,0,0] mode. Fortunately, the rotation of an element plane is the most common distortion to be encountered, and for this the element behaves relatively well with errors in the 1st axial mode of less than one percent for rotation of up to 45 degrees.

In view of the high sensitivity of the $[1,0,0]$ to twisting distortions, it was decided to rerun this problem using the ISOHERM32 model unconstrained (48 DOF) and the HEX32 model (52 DOF). The comparison of results for the different models for the $[1,0,0]$ mode is given in Figure 2.7. All three models showed similar sensitivity to the rotational distortion. The ISOHERM32 unconstrained model shows a high sensitivity to the twisting distortion, similar to that found with the ISOHERM32 constrained model. The HEX32 model, on the other hand, gave lower errors for the twisting distortion than for the rotational distortion. This is consistent with the behavior of the ISOHERM32 constrained model for the $[2,0,0]$, and $[3,0,0]$ modes.

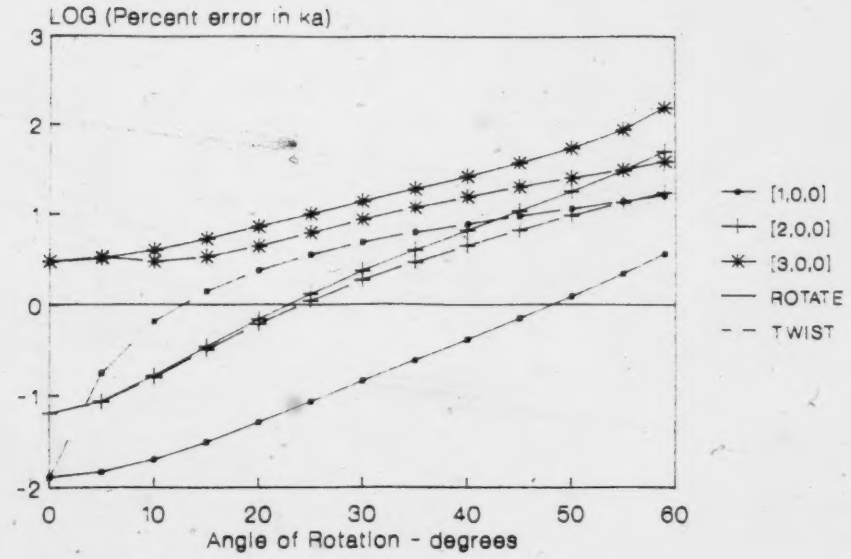

Figure 2.6 The Effect of Distortion of the Common Plane in an ISOHERM32 Two-element Box on the Eigenvalues ka

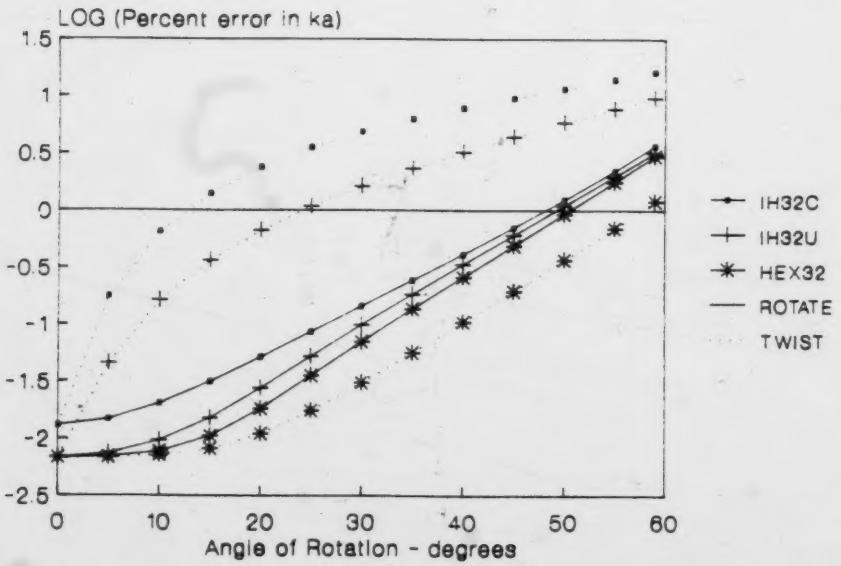

Figure 2.7 The Effect of Distortion of the Common Plane in a Two-element Box on the Eigenvalues for the [1,0,0] Mode

The two dimensional ISOHERM12 model was also run to check this element. For this model only the rotational distortion could be used in two dimensions. The constrained ISOHERM12 model has 8 DOF and predicted all the modes shown in Table 2.2 with $n_z = 0$ with results identical to those obtained with the ISOHERM32 model.

This work could be extended to look at other types of distortion and investigate why the $[1, 0, 0]$ is so sensitive to the twisting distortion. In the following section, the effect of curved boundaries is investigated.

2.3.3 Modeling A Cylindrical Cavity

The previous section dealt with a two- . . ment model in which an internal boundary between elements was distorted. A more realistic and commonly occurring problem is to model volumes within complex shaped boundaries. Probably the simplest volume with curved boundaries for which an analytical solution is obtainable is a cylindrical cavity.

The exact solution can be obtained by starting with the Helmholtz equation in cylindrical coordinates r, φ, z and using separation of variables (see for example [41]). This leads to the following equation for the eigenvalues for a hard walled cylindrical cavity with length l and radius a

$$ka = \pi\sqrt{(\alpha_{mn})^2 + \left(\frac{n_z}{r_z}\right)^2} \tag{2.41}$$

where $r_z = l/a$ and the characteristic value α_{mn} is obtained from the n^{th} root of the following equation in terms of the Bessel function J_m

$$\frac{d\,J_m}{d\alpha}(\pi\alpha) = 0. \tag{2.42}$$

For simplicity, this problem has been considered only in two dimensions using the ISOHERM12 and HEX12 quadrilateral elements. The geometric distortion of the parent elements to create a cylinder is only in two dimensions and as shown in the previous section for the case of $n_z = 0$, the three dimensional ISOHERM32 element model gave identical results to the 2 dimensional ISOHERM12 model. For the case of $n_z = 0$ the eigenvalues are given by $ka = \pi\alpha_{mn}$.

The finite element models used are shown in Figure 2.8 and the resulting prediction errors for the various models are given in Table 2.4. The first models run were single element models using the ISOHERM12 element constrained (IH12C), the ISOHERM12 element unconstrained (IH12U) and the HEX12 element. Except for modes with $m = 0$, each mode is doubly degenerate. Modes with $m = 0$ can be referred to as r-axial as the motion of these waves is entirely radial. Modes for which $n = 0$ can be referred to as φ-axial modes, although the wave motion is not entirely in the φ direction. The one-element ISOHERM12 constrained model predicted only the φ-axial modes $[1,0]$, $[2,0]$, $[3,0]$ and $[4,0]$. The ISOHERM12 unconstrained and HEX12 one-element models also predicted the $[0,1]$ r-axial mode and the $[1,1]$ and $[1,2]$ r,φ-tangential modes, but the errors for these additional modes as shown in Table 2.4 were very high. The errors for all modes are much higher than obtained with the undistorted one-element models of rectangular cavities. The HEX12 one-element model gave the smallest errors for all modes.

The four-element models gave much better results, particularly in the radial modes. For these models, the HEX12 element still gave smaller errors for the first two modes, but gave higher errors than the ISOHERM12 unconstrained element model for higher modes.

In the above models, the right-angle corners of the parent elements are severely distorted to almost 180 degrees. An alternative four-element model can

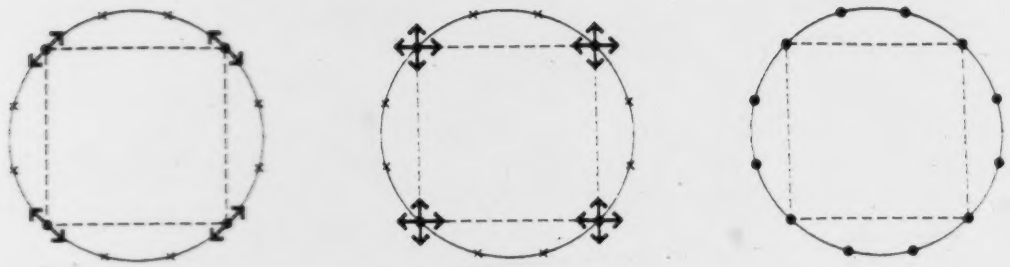

ISOHERM12
Constrained (8 DOF)

ISOHERM12
Unconstrained (12 DOF)

HEX12
(12 DOF)

a) Single Element Models

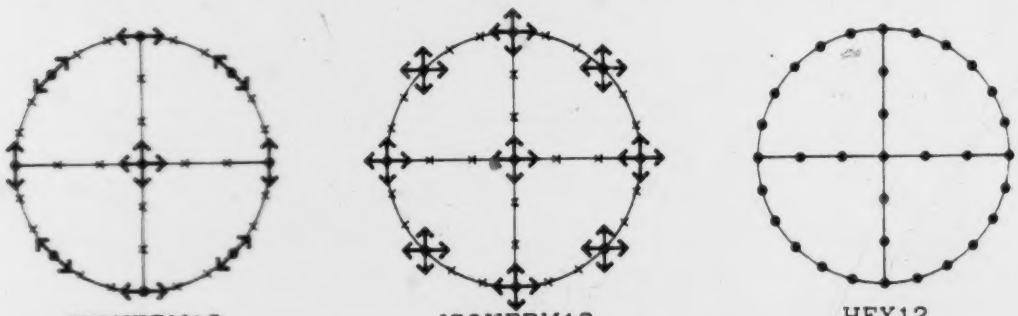

ISOHERM12
Constrained (19 DOF)

ISOHERM12
Unconstrained (27 DOF)

HEX12
(33 DOF)

b) Four-element models

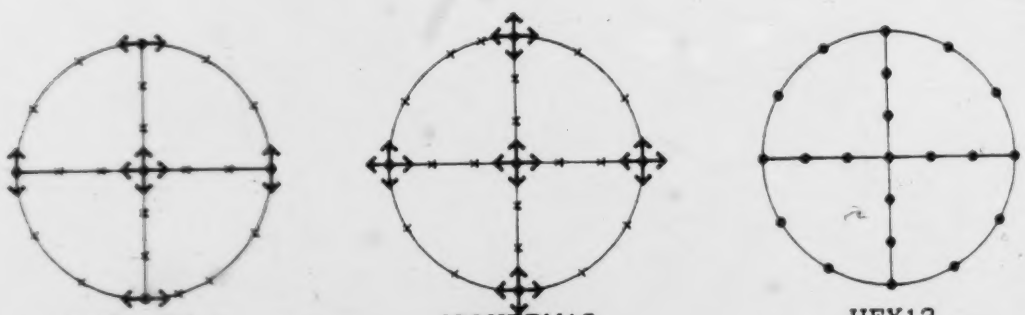

ISOHERM12
Constrained (11 DOF)

ISOHERM12
Unconstrained (15 DOF)

HEX12
(21 DOF)

c) Four-element models with one side of each element collapsed

Figure 2.8 Finite Element Models for a Circular Cylinder

Table 2.4 Eigenvalues for a Two-dimensional Model of a Circular Cylinder

Model	Element	DOF	Percent Error in ka					
			Mode $[m,n]$					
			[1.0]	[2.0]	[0.1]	[3.0]	[4.0]	[1.1]
1 EL	IH12C	8	8.855	33.57		54.97	52.99	
	IH12U	12	3.548	24.29	154.9	51.48	52.99	196.3
	HEX12	12	2.688	14.11	92.80	33.14	27.76	141.3
4 EL	IH12C	19	0.287	2.926	.168	5.215	2.762	3.447
	IH12U	27	0.200	2.815	.087	3.684	2.642	3.447
	HEX12	33	0.122	2.549	.136	4.174	4.330	5.770
4 EL Collapsed	IH12C	11	0.475	0.500	.769	4.533	6.391	8.259
	IH12U	15	0.437	0.490	.400	4.488	6.387	8.259
	HEX12	21	0.196	2.095	.006	8.071	4.971	12.21
Exact ka			1.841	3.054	3.832	4.201	5.318	5.331

be produced by collapsing one side of each element to a point at the centre of the circular outer boundary as show in Figure 2.8c. Lines of constant ξ and γ within the element then approximate a polar coordinate grid.

The four-element ISOHERM12 collapsed constrained model then has eleven DOF, and thus has fewer DOF and gives significantly lower errors than the one element HEX12 model and gives overall lower prediction errors than the four element HEX12 collapsed model.

Based on the above, a circular duct could be modeled using duct segments, each constructed with four collapsed constrained ISOHERM32 elements and give less than one percent error for the first three cross modes. This model would have 16 DOF per duct segment and would generally give lower errors than a four element collapsed HEX32 model which would have 29 DOF per segment.

2.3.4 Modeling A Complex Shaped Enclosure

As a test of the three-dimensional ISOHERM32 element to model a complex shaped enclosure, the problem of modeling an automobile passenger compartment has been considered. Experimental measurements on a one-half to two-thirds scale model of an automobile passenger compartment were made by Buma [7]. This reference also gives results based on a thirty-element HEX32 FEM model which was run on a mainframe computer. The construction of the scale model enclosure is shown in Figure 2.9.

Three-element and ten-element ISOHERM32 models were chosen to numerically model the problem as shown in Figure 2.10. Also shown is the thirty-element (378 DOF) model used in [7].

In the previous sections, constraint equations on the acoustic pressure gradient nodal quantities at rigid surfaces were used to reduce degrees of freedom in the models. This was applied at nodes on continuous surfaces and at corner nodes in rectangular enclosures. For the complex enclosure studied here, there are several corners and edges at oblique angles. At the corner or edge discontinuities, as the discontinuity is approached along different surfaces, the pressure gradient vector points in different directions and thus the pressure gradient components must be zero at the discontinuity. In the case of a rectangular enclosure, for example along a surface with y constant, the gradient component $\partial P/\partial y$ is zero at the corners of the enclosure and along the surface. Considering an oblique plane in a more complex model, $\partial P/\partial y$, for example, may be zero at the adjoining corners but becomes nonzero along the plane. In this case, particularly when a small number of elements is used, constraining the corner or edge gradient nodal quantities to zero may produce too severe a constraint on the model. This was tested by running the

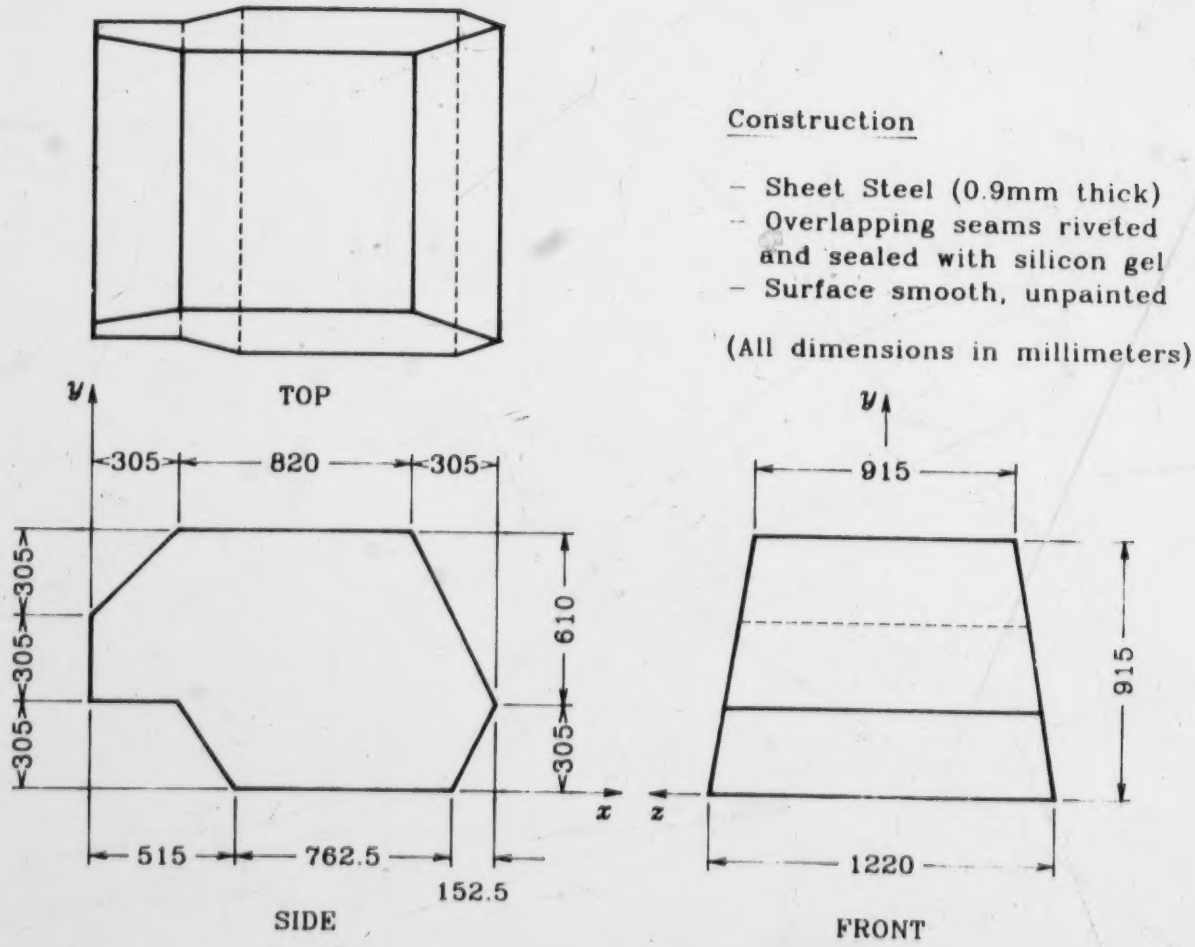

Figure 2.9 Model of an automobile enclosure

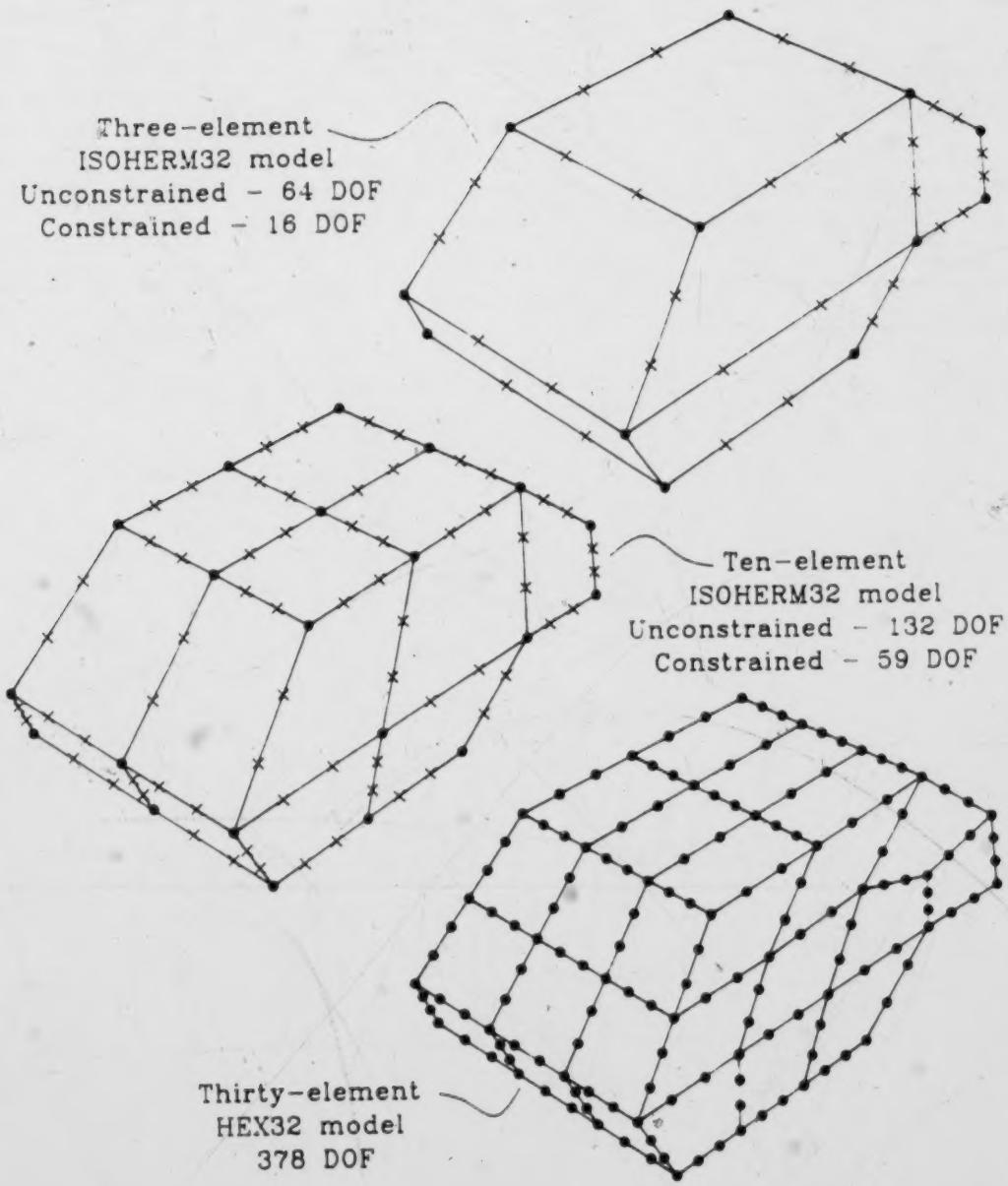

Figure 2.10 Finite Element Models of an Automobile Passenger enclosure

ISOHERM32 models unconstrained and then with the appropriate edge and corner nodal gradient quantities constrained to zero.

The measured enclosure natural frequencies are compared to the FEM predictions in Table 2.5. Note that the n_x, n_y and n_z indices have been used to provide a rough correspondence between the more complex modes found and the equivalent modes in a rectangular enclosure. The ISOHERM32 element models are identified as IH32C3, IH32U3, IH32C10 and IH32U10, where the "U" and "C" refer to the unconstrained and constrained models respectively and the suffix "3" and "10" refer to the three-element and ten-element models. The run time shown was for implementation on a Hewlett Packard HP9816 computer. There is good agreement between the unconstrained ten-element ISOHERM32 model and the thirty element HEX32 model (less than two percent difference between these models).

Comparison of the IH32U10 and HEX32 predictions with the measured natural frequencies shows that the predicted values were five to forty percent lower than the measured values. The walls of the experimental enclosure were constructed of 0.9 mm sheet steel with no stiffening members and were thus not very rigid whereas the predictions were based on a rigid walled enclosure. Craggs [19] showed that boundary flexibility can either increase or decrease the natural frequency of a given mode. A stiffness controlled boundary reduces the natural frequency and a mass controlled boundary increases the natural frequency compared to the rigid walled case.

Comparison of IH32U10, the ten-element ISOHERM32 model unconstrained, with IH32C10, the same model constrained, shows that constraining the model increased most of the natural frequencies by two to ten percent with the largest difference occurring in the axial mode $[2,0,0]$ between the front and back of

Table 2.5 Natural Frequencies for Acoustic Modes in an Automobile Passenger Enclosure Model

Mode			Resonant Frequency in Hz.					
n_x	n_y	n_z	Measured	IH32C3	IH32U3	IH32C10	IH32U10	HEX32
1	0	0	154.6	151.0	141.2	147.4	140.8	140.8
0	0	1	168.2	160.4	159.9	160.4	160.1	160.3
0	1	0	220.2	220.8	211.2	215.1	209.3	208.9
1	0	1	226.6	231.5	214.2	218.9	214.6	214.3
2	0	0	251.0	289.1	249.2	271.2	245.0	243.3
0	1	1	281.8	305.5	269.3	272.0	267.0	267.8
2	0	1	301.8	350.1	293.5	314.8	294.2	288.8
1	1	0	312.2	378.2	304.1	315.8	304.2	299.9
0	0	2	323.8	409.5	350.5	322.2	314.6	315.4
1	0	2	355.4	455.1	381.1	355.2	351.5	353.2
1	1	1	366.6	477.6	396.3	366.3	352.6	347.0
0	2	0	378.2	507.4	420.2	389.3	373.2	371.3
No. of elements				3	3	10	10	30
Degrees of freedom				16	64	59	132	378
Run time in hours				0.20	2.93	5.30	26.44	N/A

the enclosure. The exception was the axial mode $[0, 0, 1]$ between the sides of the enclosure which differed by no more than 0.3 percent for all the models. This is reasonable since the side walls are flat and approximately parallel and approach the case of parallel walls in a rectangular enclosure, in which even the single element constrained model gave high accuracy for this mode.

The unconstrained three-element model (IH32U3) has a similar number of DOF to the constrained ten-element model (IH32C10) but gives much closer results compared to the IH32U10 model for the first eight modes (within two percent). The constrained three-element model (IH32C3) gave results that were six to thirty-six percent higher than the IH32U10 model, with the exception of the $[0, 0, 1]$ mode discussed above which was within 0.2 percent of the IH32U10 model. By coincidence, several of the lower natural frequencies for the three element constrained model are close to the measured values—the increased prediction errors incurred

using the constrained smaller model offset the error introduced by the assumption of a rigid walled model.

In summary, the test of the ISOHERM32 element model unconstrained showed good agreement with results from [7] using the HEX32 element. However, even though at oblique corners and edges components of the pressure gradient are zero, using these as constraints, over constrained the models. This gave much higher errors than obtained when similar constraint equations were used in rectangular enclosures.

2.4 Testing the Element: Incompressible Potential Flow

In subsequent chapters, a model is developed for sound propagation in duct system components including the effect of steady flow through the components at low Mach number. The model chosen reduces to small amplitude acoustic wave propagation convected by an incompressible steady potential flow. The potential flow solution can be obtained first and then used in the solution of the equations governing the acoustic problem. In this section the FEM equations used to solve the incompressible potential flow problem are developed and used to test the ISOHERM12 element by modeling some simple flow problems for which exact solutions are known.

2.4.1 Equation Development

The governing differential equation for incompressible steady potential flow is the Laplace equation (see for example [44], Chapter 17) given by

$$\nabla^2 \bar{\phi}^* = 0 \tag{2.43}$$

where $\bar{\phi}^*$ is the steady flow velocity potential related to the flow velocity $\bar{u}^*$ by

$$\bar{u}^* = \nabla \bar{\phi}^*. \tag{2.44}$$

The bar over the variables indicates the steady or mean flow component as opposed to the acoustic fluctuating component to be introduced in subsequent chapters. The "*" indicates dimensional quantities. Equation 2.43 can be non-dimensionalized by defining a non-dimensional velocity potential $\phi = \phi^*/(Mc_0d)$ where M is a typical Mach number for the flow, c_0 is the ambient speed of sound (fluid at rest) and d is a typical dimension used to non-dimensionalize all lengths. Substituting into Equation 2.43 then yields

$$\nabla^2\bar{\phi} = 0 \tag{2.45}$$

and the dimensional velocities can then be obtained from

$$\bar{\mathbf{u}}^* = Mc_0\nabla\bar{\phi} \tag{2.46}$$

where the gradient and Laplacian operators are now in terms of non-dimensional coordinates. A general model of a duct component with several inlets and outlets has been considered. Figure 2.11 gives an example of a two dimensional model with unit depth and with a single inlet of width d_1 and two outlets with widths d_2 and d_3. It is assumed that the inlet and outlets are attached to straight ducts which have uniform velocity profiles. The boundary condition at the duct wall is that the flow velocity normal to the wall $\bar{u}_n^*$ is zero or $d\bar{\phi}/dn$ is zero along the duct walls. Usually the typical Mach number M has been taken as the inlet Mach number. The inlet boundary condition is then $d\bar{\phi}/dn = -1$ where the negative sign shows that the inlet velocity is in the opposite direction to the outward pointing normal. The boundary conditions at the outlet surfaces are then given by $d\bar{\phi}/dn = M_2/M_1$ and $d\bar{\phi}/dn = M_3/M_1$ where M_1 is the inlet Mach number and M_2 and M_3 are the outlet Mach numbers. The inlet and outlet velocities must be chosen to satisfy incompressible flow continuity. With these boundary conditions the problem is the

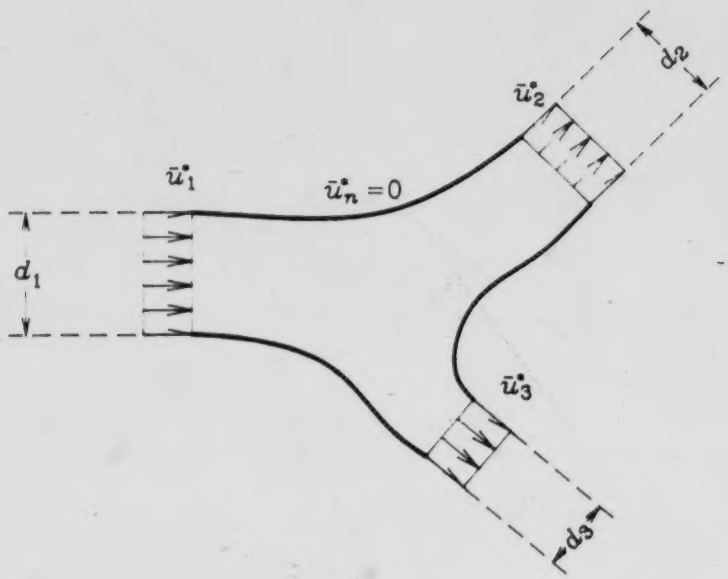

Figure 2.11 Flow Model of a Duct Junction

Neumann boundary value problem, and as posed, the velocity potential $\bar{\phi}$ can only be determined to within an additive constant. To make the solution unique, the value of the velocity potential was arbitrarily assigned to one point in the model.

In Section 2.3.1, the Galerkin method was used to set up the finite element formulation to solve the Helmholtz equation. The Laplace Equation 2.45 can be obtained by setting k equal to zero in the Helmholtz Equation 2.25 and replacing P by $\bar{\phi}$ in the development. This leads to an equation similar to Equation 2.29,

$$\iint_S \{N\} \frac{d\bar{\phi}}{dn}\, ds - \iiint_V \nabla\{N\} \bullet \nabla\bar{\phi}\, dv = \{0\}. \tag{2.47}$$

In the eigenvalue problem previously considered, the surface integral term was zero over the entire boundary. In the present problem this term has nonzero components at the inlet and outlet boundaries. Substituting

$$\bar{\phi} = \langle N \rangle \{\bar{\phi}_g\} \tag{2.48}$$

gives

$$\iiint_V \nabla\{N\} \bullet \nabla\langle N\rangle \, dv \, \{\bar{\phi}_g\} = \iint_S \{N\} \frac{d\bar{\phi}}{dn} \, ds. \tag{2.49}$$

This equation is integrated on an element basis and then assembled into a global matrix equation. The integral on the left hand side of the equation leads to the element stiffness matrix given by Equation 2.32. The right hand side of Equation 2.49 becomes a source vector which is integrated on an element basis and assembled into a global equation. Only the element integrals on the input and output surfaces give nonzero contributions to the global source vector—at wall surfaces $d\bar{\phi}/dn$ is zero and terms on interior surfaces between adjacent elements cancel. The element source vector $\{Q_e\}$ on the input and output surfaces is then given by

$$\{Q_e\} = \frac{M_j}{M} \iint_{S_e} \{N\} \, ds \tag{2.50}$$

where M_j is the Mach number on surface j (taken as positive when the flow is in the direction of the outward directed normal. Integrating in the element domain, for example, on the surface of constant ζ gives

$$\{Q_e\} = \frac{M_j}{M} [J_g]^T \int_{-1}^{1} \int_{-1}^{1} \{F\} J_s \, d\xi \, d\gamma \tag{2.51}$$

where J_s is the surface Jacobian given in this case by

$$J_s = \left\| \begin{matrix} \vec{i} & \vec{j} & \vec{k} \\ \frac{\partial x}{\partial \xi} & \frac{\partial y}{\partial \xi} & \frac{\partial z}{\partial \xi} \\ \frac{\partial x}{\partial \gamma} & \frac{\partial y}{\partial \gamma} & \frac{\partial z}{\partial \gamma} \end{matrix} \right\| \tag{2.52}$$

where the double vertical bars indicate the magnitude of the determinant.

In the two dimensional formulation the element stiffness matrix becomes

$$[S_e] = [J_g]^T \int_{-1}^{1} \int_{-1}^{1} [M]^T \left[J^{-1}\right]^T \left[J^{-1}\right] [M] \, |J| \, d\xi \, d\gamma \, [J_g] \tag{2.53}$$

where the Jacobian matrix $[J]$ is in terms of the global coordinates x and y and the element coordinates ξ and γ. The element source vector terms are then given by

$$\{Q_e\} = \frac{M_j}{M} [J_g]^T \int_{-1}^{1} \{F\} J_\xi \, d\xi \tag{2.54}$$

on a surface of constant γ and by

$$\{Q_e\} = \frac{M_j}{M} [J_g]^T \int_{-1}^{1} \{F\} J_\gamma \, d\gamma \tag{2.55}$$

on a surface of constant ξ where

$$J_\xi = \sqrt{(J_{11})^2 + (J_{12})^2} \quad \text{and} \quad J_\gamma = \sqrt{(J_{21})^2 + (J_{22})^2} \tag{2.56}$$

and where J_{11}, J_{12}, J_{21} and J_{22} are elements of the Jacobian matrix $[J]$.

The element integrations were carried out using Gauss-Legendre quadrature rules as discussed in Section 2.3.1 and the element matrices assembled into a global matrix equation

$$[S] \{\bar{\phi}_g\} = \{Q\}. \tag{2.57}$$

The matrix $[S]$ is singular which explains why an eigenvalue was found at $k = 0$ (the rigid body mode) when solving the Helmholtz equation in Section 2.3. Consistent with the previous discussion of the Neumann problem, the velocity potential at one of the nodes in $\{\bar{\phi}_g\}$ is constrained to an arbitrary value. As discussed in Section 2.3.1 in terms of the acoustic velocity or pressure gradient, additional constraint equations can also be used here to reduce the size of the above matrix equation based on the fact that the flow velocity at the boundary is parallel to the wall. The appropriate components of the velocity potential derivative quantities in $\{\bar{\phi}_g\}$ can be set to zero at boundaries parallel to the global coordinate axes. At sloped or curved boundaries, linear constraint equations can be used to eliminate some of the unknown nodal derivative quantities.

The interpreter Basic, on the computer used in this work, contained a machine language matrix inversion routine. For the size of the systems of equations encountered, it was found faster to use this matrix inversion routine rather than a Gauss-Jordan equation solver programmed in interpreter Basic. The unknown vector of nodal velocity potential and derivative quantities was then obtained from

$$\{\bar{\phi}_g\}_R = [S]_R^{-1}\{Q\}_R \tag{2.58}$$

where the subscript R refers to the reduced system of equations after applying the constraint equations.

After obtaining $\{\bar{\phi}_g\}_R$, the constraint equations could then be used to construct the entire nodal vector $\{\bar{\phi}_g\}$ and the following equations used to calculate the velocity potential and velocities at points within each element of the model.

$$\bar{\phi}(\xi,\gamma,\zeta) = \langle F \rangle [J_g] \{\bar{\phi}_g\} \tag{2.59}$$

$$\begin{Bmatrix} \frac{M_x}{M} \\ \frac{M_y}{M} \\ \frac{M_z}{M} \end{Bmatrix} = \begin{Bmatrix} \frac{\partial\bar{\phi}}{\partial x} \\ \frac{\partial\bar{\phi}}{\partial y} \\ \frac{\partial\bar{\phi}}{\partial z} \end{Bmatrix} = [J]^{-1}[M]\{\bar{\phi}_g\} \tag{2.60}$$

The quantities M_x, M_y and M_z are the local Mach numbers corresponding to the x, y and z components of the local flow velocity.

2.4.2 Uniform Flow in a Straight Duct

The first flow problem considered was uniform flow of Mach M through a straight duct of length d and width $0.3d$ with the longitudinal axis of the duct parallel to the x axis. The exact non-dimensional velocity potential for this problem is given by $\bar{\phi} = x + 1$ where the coordinates have been non-dimensionalized based on the length d and the additive constant has been chosen so that $\bar{\phi}(0) = 1$.

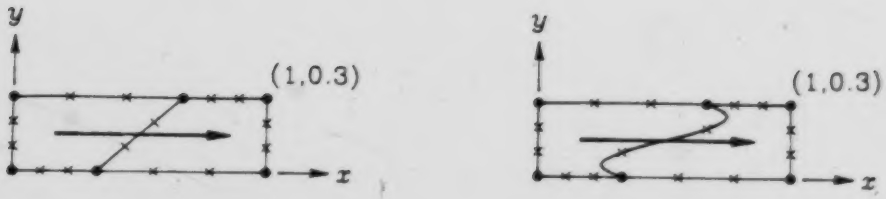

Figure 2.12 Two-element Models for Uniform Flow

The problem was modeled initially with one undistorted unconstrained ISOHERM12 two-dimensional quadrilateral element located between $x = 0$ and $x = 1$ and $y = 0$ and $y = 0.3$. This gave a model with eleven DOF since the velocity potential at the corner (0,0) was constrained to $\bar{\phi} = 1$. This finite element model predicted the velocity potential and velocities exactly (within the accuracy of the computer) for this case. The boundary conditions on the velocities can be used to constrain $\partial\bar{\phi}/\partial x = 1$ and $\partial\bar{\phi}/\partial y = 0$ at the four corner nodes of the element, reducing the model to three DOF. This model also predicted the velocity potential and velocities exactly at the corner nodes and within the element. This problem was also modeled using two elements to study the effect of distorting the element boundary. The common plane between elements was first tilted and then distorted to a curved surface as shown in Figure 2.12. The predictions were made using the ISOHERM12 model unconstrained (17 DOF) and constrained (7 DOF). In both cases the finite element model again, within the accuracy of the computer, predicted the velocity potential and velocities exactly, both at the element nodes and at randomly selected points within the model.

2.4.3 Uniform Radial Flow from a Point Source

A second ideal flow problem was considered to test the distorted element with curved boundaries. The problem selected was the two-dimensional radial flow

from a line source.

A sector of the flow from a radius $R_1 = 0.1$ to a radius $R_2 = 1$ and subtending an angle β was modeled. The geometry of the sector is shown in Figure 2.13. The non-dimensionalized velocity potential function for this flow (see for example [44], Chapter 18) is

$$\bar{\phi} = 1 + 0.1\ln(10r) \tag{2.61}$$

where r is the radial coordinate from the source origin, non-dimensionalized based on the outlet radius. The additive constant has been chosen to give a unity velocity potential at the inlet. The non-dimensional radial velocity $\bar{u}_r$ is then given by

$$\bar{u}_r = \frac{0.1}{r} \tag{2.62}$$

so that the inlet velocity $\bar{u}_r = 1$ and the outlet velocity $\bar{u}_r = 0.1$. The x and y components of the velocity are

$$\bar{u}_x = \frac{0.1x}{r^2} \qquad \text{and} \qquad \bar{u}_y = \frac{0.1y}{r^2}. \tag{2.63}$$

This problem was modeled using the unconstrained ISOHERM12 element, and also with the velocity potential gradient nodal quantities constrained, so that the nodal velocities were parallel to the radial walls of the sector. For comparison, a HEX12 model was also used. Models having one to sixteen elements were used, having the number of DOF shown in Table 2.6. The elements were joined in a radial string as shown for the four-element models in Figure 2.13. With each doubling of the number of elements, the angle β subtended by the sector was halved, thus geometrically simulating a doubling of the number of elements in the circumferential direction as well.

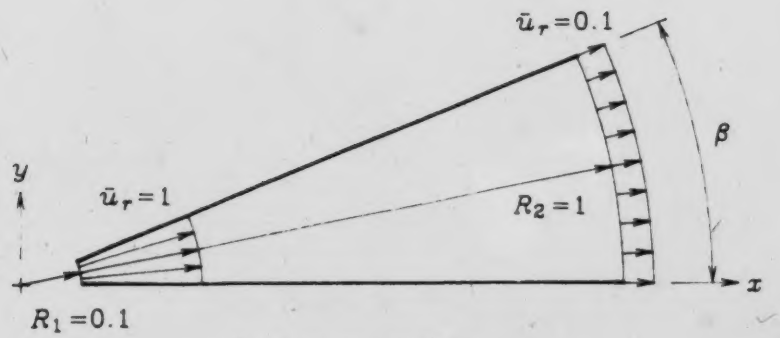

Sector geometry

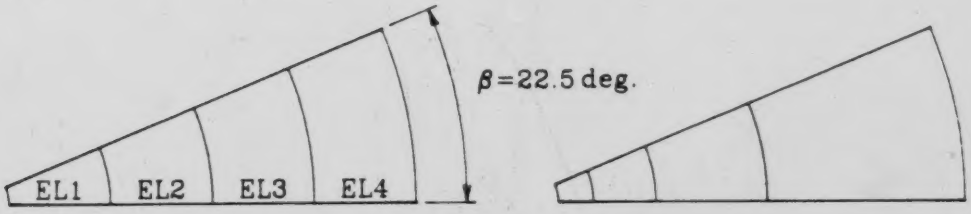

Equal length

Geometrically similar

Four-element sector models

ISOHERM12
Unconstrained

ISOHERM12
Constrained

HEX12
Element

Figure 2.13 Models for the Sector Flow Problem

Table 2.6 Sector Flow Model Degrees of Freedom

Number of Elements	Sector Angle β degrees	Number of degrees of freedom		
		ISOHERM12 constrained	ISOHERM12 unconstrained	HEX12
1	90	7	11	11
2	45	11	17	19
4	22.5	19	29	35
8	11.25	35	53	67
16	5.625	67		

The first models used consisted of elements of equal radial length. For this case it was found that much higher errors occurred in the element closest to the inlet than for the element at the outlet. Additional results were then obtained using geometrically similar elements—that is elements in which the ratio of the element inlet radius to the element outlet radius was the same for all elements.

In the eigenvalue problem considered in Section 2.3, the accuracy of the predictions could be considered in terms of the eigenvalues—a parameter depending on the entire model. In the flow problem the velocity potential, the velocity components and the prediction errors in these quantities can vary from point to point in the model. After obtaining the vector of nodal quantities $\{\bar{\phi}_g\}$, the velocity potential and local x and y flow velocity components were calculated over a grid of 10×10 points in each element of the model using Equation 2.59 and Equation 2.60. The errors in the velocity potential and radial velocity were then calculated at each of the 100 points and searched to obtain the maximum error in each element.

Figure 2.14 shows the convergence of the three models with equal length elements in terms of the velocity potential and the radial velocity. The errors in the velocity predictions are approximately two orders of magnitude higher than the errors in velocity potential. The legend entries IH12C and IH12U refer to the

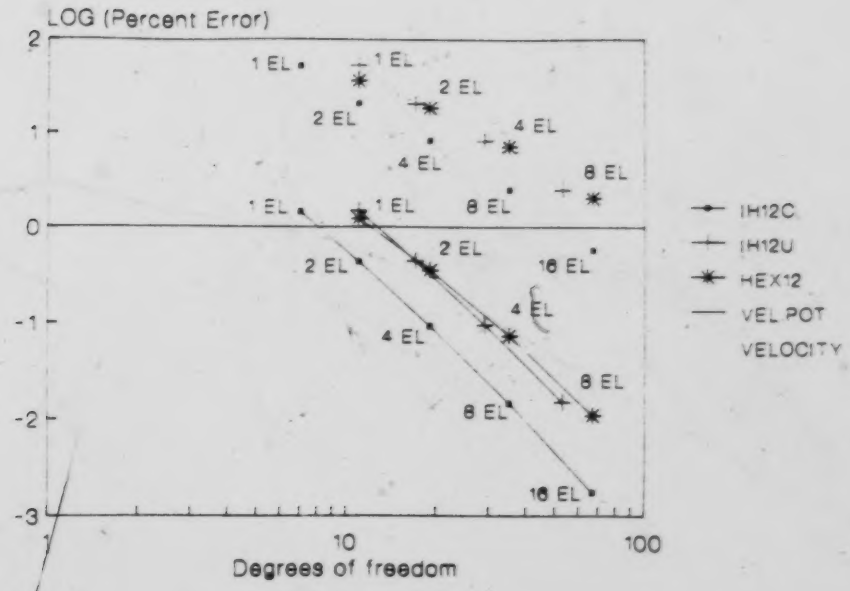

Figure 2.14 Maximum Errors for the Sector Flow Models with Equal Length Elements

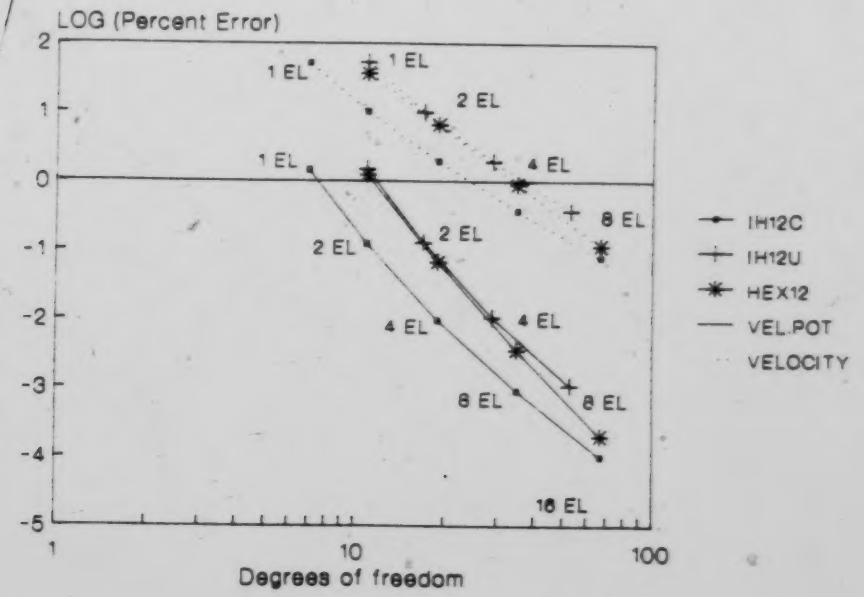

Figure 2.15 Maximum Errors for the Sector Flow Models with Geometrically Similar Elements

ISOHERM12 models constrained and unconstrained respectively. On an element basis, the three models have similar maximum errors. Note however, that the ISOHERM12 constrained model has half the DOF of the HEX12 model with the same number of elements, so that on a DOF basis the ISOHERM12 constrained model shows significantly lower maximum errors. Also the ISOHERM12 models show slightly higher rates of convergence than the HEX12 model.

The results for the models with geometrically similar elements are shown in Figure 2.15. This graph shows higher rates of convergence compared to the results obtained with the equal length element models in Figure 2.14. In this case the maximum errors for the 8-element and 16-element models are an order of magnitude lower than for the equal length element models. For the geometrically similar element case, the HEX12 element shows a higher rate of convergence than the ISOHERM12 models. The maximum errors in the HEX12 eight-element model, in fact, approach that of the ISOHERM12 constrained 16-element model which has the same number of DOF.

The above results are presented in terms of the maximum errors in the overall model. Comparison of the errors in different elements of the models shows some other significant differences, most noticeable in terms of the velocities. Figure 2.16 compares the maximum error in velocities in the first element (inlet) and last element (outlet) of the ISOHERM12 constrained and the HEX12 equal length element models. For the HEX12 model, curves for the first and last elements diverge considerably, giving errors in the last element of two hundred times smaller than for the first element in the eight element model. The curves for the ISOHERM12 constrained model are much closer, with errors in the last element only one tenth the error in the first element. For the case of geometrically similar elements, the

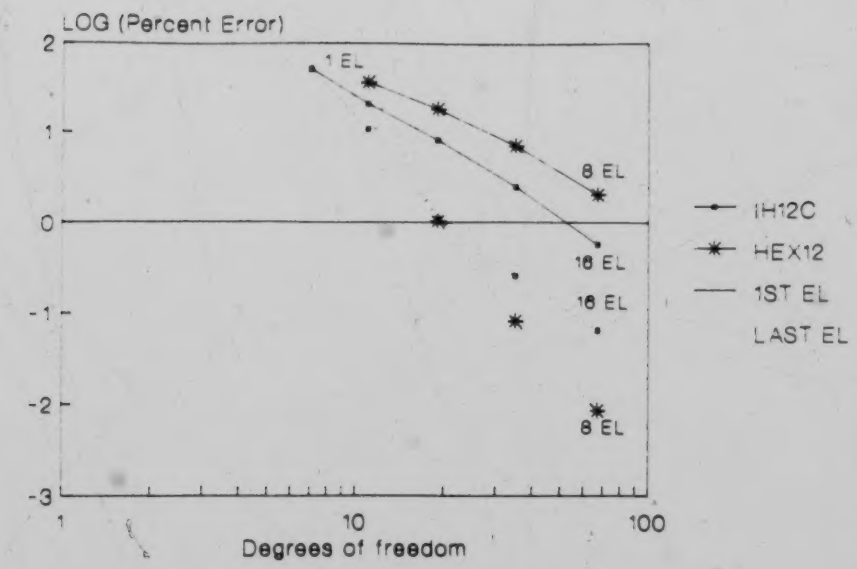

Figure 2.16 Comparison of Maximum Errors for the First and Last Elements of the Sector Flow Models with Geometrically Similar Elements

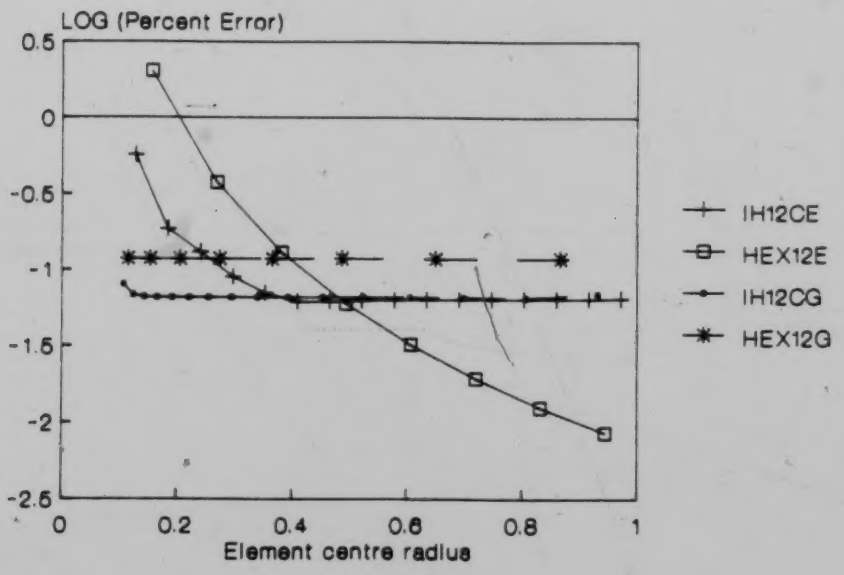

Figure 2.17 Maximum Element Errors for Sector Flow Velocities with the 67 DOF Models

Table 2.7 Errors in Sector Flow Velocities with Geometrically Similar Elements

Number of Elements	Maximum percent error in radial velocity					
	ISOHERM12con			HEX12		
	DOF	1st EL	Last EL	DOF	1st EL	Last EL
1	7	51.954	51.954	11	36.806	36.806
2	11	10.208	10.338	19	6.6984	6.6991
4	19	1.9768	1.8416	35	0.92316	0.92318
8	35	0.38284	0.34009	67	0.11826	0.11826
16	67	0.08010	0.06922			

maximum errors in each element of a given model were almost equal, as shown in Table 2.7. For the HEX12 model, for the eight-element case, the maximum percent errors in velocity for each of the eight elements were in fact identical to six significant digits. This is in contrast to the ISOHERM12 model where the errors between the first and last elements differed by one percent for the two-element model and increased to thirteen percent for the 16-element model.

The variation in maximum element error within the models is shown for the 67 DOF cases in Figure 2.17. Here the maximum percent error in each element is plotted as function of the radius to the centre of each element. The suffix "E" and "G" refer respectively to the "Equal length element" and "Geometrically similar element" models. The HEX12 equal length element model gave maximum errors at the inlet element. The errors then decreased continuously to a minimum in the last element at the outlet. When using geometrically similar HEX12 elements, equal maximum percentage errors were obtained in each element. The ISOHERM12 constrained equal length element model gave maximum errors at the inlet element leveling off at an approximate plateau for elements at a radius greater than 0.4. The ISOHERM12 constrained geometrically similar element model shows a similar

error plateau over most of the elements, with slightly higher errors at the inlet element and outlet element. A similar pattern was observed for the unconstrained ISOHERM12 models.

In summary, on a DOF basis, the ISOHERM12 constrained model gave the lowest maximum errors, and the maximum error was reduced significantly by using geometrically similar elements rather than equal length elements. This is reasonable since the use of geometrically similar elements gives a greater density of elements in the region where the logarithmic velocity potential function varies most rapidly. For the equal length element models, the greatest errors occurred in the element nearest the inlet. The maximum element error then decreased continuously to the outlet for the HEX12 model, but decreased to a plateau in the ISOHERM12 models and then increased again in the last element at the outlet. In the HEX12 models with geometrically similar elements, the maximum errors were equal in all elements. In the ISOHERM12 geometrically similar models, the errors were approximately the same in most elements, with slightly higher errors occurring in the inlet and at the outlet elements.

CHAPTER III

FEM MODEL DEVELOPMENT FOR ACOUSTICS WITH FLOW

3.1 Equation Development

In this chapter the finite element model used to study the acoustic propagation in duct components, including the effect of a steady incompressible flow, is developed and tested. This section of the chapter considers the theoretical development of the acoustic-flow model. Subsequent sections deal with the testing of the model for problems with known analytical solutions and numerical solutions of other researchers.

3.1.1 Selecting a Flow Model

Much of the work concerning acoustic propagation in the presence of flow has dealt with flow at high subsonic Mach numbers. The presence of a mean flow complicates the acoustic problem in several ways as discussed by Eversman and Astley [31]:

- Computation of the flow field alone, in nonuniform ducts, constitutes a very significant problem, and in some cases approximate flow solutions have been adopted.
- In the absence of flow, the acoustic equations admit only solutions without vorticity. With flow present the linearized acoustic equations can still admit solutions with vorticity. If the mean flow is irrotational then

the acoustic perturbations can be assumed irrotational and the velocity potential can be introduced.

- If the equations are used in primitive form (that is in terms of the acoustic pressure and acoustic velocity components), for both rotational and irrotational flow, irrotational acoustic perturbations and rotational "hydrodynamic modes", which are convected with the flow, can occur.

Sigman et al [53] considered high subsonic compressible irrotational flow of an inviscid, non-heat-conducting medium to study turbofan inlet acoustics. The flow in the duct was described by a nonlinear partial differential equation with the flow velocity potential as the dependent variable. This velocity potential was then considered as a sum of a mean flow potential and an acoustic potential. It was then assumed that the mean flow was undisturbed by the presence of the acoustic perturbations. This allowed separation of the equations into a mean flow equation involving just the mean flow potential and a linearized acoustic equation involving both the mean flow and the acoustic velocity potentials. In [53] the approximate flow potential was obtained by using an integral technique to calculate the incompressible potential flow with a correction to account for compressibility effects.

Eversman and Astley [6], [31] also considered the effect of high subsonic flow on the acoustic transmission in nonuniform ducts. They used an approximate flow model based on a one dimensional isentropic nozzle flow with a kinematic adjustment requiring the flow to be tangent to the wall. The flow model was rotational so that an acoustic velocity potential could not be used. Instead a formulation with the acoustic pressure and acoustic velocity components as dependent variables was used. The resulting equations admitted both acoustic perturbations and rotational "hydrodynamic" perturbations which were convected by the flow.

Cabelli [10] considered the influence of flow on the acoustic characteristics of a duct bend with inlet Mach numbers of 0.25 and 0.4. A compressible potential flow model was used in terms of the mean flow potential and the acoustic velocity potential. Solution of the steady flow equations was implemented using a Galerkin FEM with the stream function and the local density as dependent variables. The resulting system of two equations was solved iteratively, updating the values of local density with each iteration. Six-noded triangular elements were used in the FEM flow solution.

Ling et al [36] took a somewhat different approach to developing a finite element model for acoustic-flow problems. Their development started with the convected wave equation (in terms of acoustic pressure) for uniform flow along the axis of the duct and assumed there was no direct coupling between the acoustic field and flow velocity field. The convected wave equation was used to formulate the element matrix equations for cubic isoparametric Serendipity elements taking the uniform flow parallel to one axis of the square parent element. The duct domain was then divided into elements in a grid consisting of the streamlines of a given flow model and lines perpendicular to the duct axis.

Peat [45] approached the problem starting with the compressible potential flow equations in a similar manner to [53] above, but made the additional assumption that Mach numbers were small. This lead to the incompressible potential flow equation which was solved first and the result used in solving the linearized acoustic equation. A Galerkin FEM with eight-node quadrilateral isoparametric elements was used to solve both the flow and acoustic equations.

The present work is concerned with the propagation of sound in HVAC duct systems in which flows generally have Mach numbers of less than 0.1. The

method used by Peat [45] seemed to be best suited for this problem. The method can be used generally for any geometric configuration and does not depend on an approximate flow solution for a given geometric configuration. The method of Ling et al [36] has the disadvantage that the acoustic finite element mesh must fit between the streamlines of previously determined flow field. This is not likely to give a very efficient mesh for the acoustic modeling of complex duct bends or branch points, particularly if it is desired to use a small number of high order elements.

Peat [45] only considered plane wave propagation in the connecting inlet and outlet ducts to the finite element model domain. In the present work the formulation of Peat [45] has been extended to include higher order mode propagation in straight ducts connected to the bend or junction FEM models. A procedure for higher order modes has been used which is in principle similar to that of Cabelli [10] although the complete details of his method are not known to the author. Cabelli's work involved problems with a single inlet and outlet. In the present work, this has been extended to include three or more connecting ducts so that junctions can be modeled. It is acknowledged that an ideal potential flow model in many cases does not give a very good representation of a real flow in which viscous effects are important, but hopefully will give some indication of the effects of the flow on the acoustic propagation at low Mach number.

3.1.2 Basic Equations

It is assumed that the flow in the duct system component is inviscid, non-heat-conducting and irrotational and that body forces can be neglected. The equations of continuity, momentum and speed of sound can then be combined to give [45],[53]

$$\nabla^2\phi^* - \frac{1}{c^2}\left[\frac{\partial^2\phi^*}{\partial t^{*2}} + \frac{\partial}{\partial t^*}(\nabla\phi^* \bullet \nabla\phi^*) + \frac{1}{2}\nabla\phi^* \bullet \nabla(\nabla\phi^* \bullet \nabla\phi^*)\right] = 0 \qquad (3.1)$$

where ϕ^* is the velocity potential and t^* is the time. The local speed of sound c can be obtained from the Bernoulli equation for isentropic potential flow and is given by

$$c^2 + (\Gamma - 1)\left[\frac{\partial \phi^*}{\partial t^*} + \frac{1}{2}(\nabla \phi^* \bullet \nabla \phi^*)\right] = c_0^2 \tag{3.2}$$

where Γ is the ratio of specific heats and c_0 is the speed of sound in ambient conditions. Note that Γ has been used for the ratio of specific heats rather than the usual γ to distinguish it from the symbol used earlier as a finite element domain spatial coordinate.

Consistent with the incompressible potential flow equation development of Section 2.4.1, Equations 3.1 and 3.2 can be non-dimensionalized by defining a non-dimensional velocity potential $\phi = \phi^*/(Mc_0 d)$ and $t = t^* c_0/d$ where M is a typical Mach number for the flow, and d is a typical dimension used to non-dimensionalize all lengths. Substituting into Equations 3.1 and 3.2 then leads to

$$\nabla^2 \phi - \frac{c_0^2}{c^2}\left[\frac{\partial^2 \phi}{\partial t^2} + M\frac{\partial}{\partial t}(\nabla \phi \bullet \nabla \phi) + \frac{1}{2}M^2 \nabla \phi \bullet \nabla (\nabla \phi \bullet \nabla \phi)\right] = 0 \tag{3.3}$$

and

$$\frac{c^2}{c_0^2} = 1 - (\Gamma - 1)\left[M\frac{\partial \phi}{\partial t} + \frac{1}{2}M^2 (\nabla \phi \bullet \nabla \phi)\right]. \tag{3.4}$$

The total potential ϕ can be split into the steady flow potential $\bar{\phi}$ and an acoustic potential ϕ''. It is assumed that the acoustic potential ϕ'' varies harmonically with time and is an order of magnitude smaller than $\bar{\phi}$ giving

$$\phi = \bar{\phi} + \phi'' = \bar{\phi} + \alpha \phi' e^{i\omega t} \tag{3.5}$$

where $\alpha << 1$, $\omega = \omega^* d/c_0$ and ω^* is the acoustic angular frequency. Note that the non-dimensional frequency parameter $\omega = kd$ where k is the commonly used acoustic wave number parameter. Also $\omega t = \omega^* t^*$.

In the present work steady flows with low Mach numbers (less than 0.1) are considered, so it can be assumed that $M^2 = O[\alpha]$. Substituting into Equation 3.3 and neglecting terms of $O[\alpha^2]$ gives

$$\nabla^2\bar{\phi} + \alpha\nabla^2\phi' e^{i\omega t} + \alpha\omega^2\phi' e^{i\omega t} - 2iM\omega\alpha\left(\nabla\bar{\phi}\bullet\nabla\phi'\right)e^{i\omega t} - \frac{1}{2}M^2\nabla\bar{\phi}\bullet\nabla\left(\nabla\bar{\phi}\bullet\nabla\bar{\phi}\right) = 0. \tag{3.6}$$

For the steady flow, if only the highest order term is retained then

$$\nabla^2\bar{\phi} = 0 \tag{3.7}$$

which is the Laplace equation governing incompressible potential flow discussed in Section 2.4. Subtracting the steady flow from Equation 3.6 gives

$$\nabla^2\phi' + \omega^2\phi' - 2iM\omega\nabla\bar{\phi}\bullet\nabla\phi' = 0. \tag{3.8}$$

Note that if the fluid is at rest, $\nabla\bar{\phi} = 0$ and Equation 3.8 reduces to the Helmholtz equation. The complete solution to the problem can be obtained by first solving Equation 3.7 for the steady flow and then using this result in Equation 3.8 to obtain the acoustic velocity potential.

The acoustic pressure P^* can be obtained from the terms remaining after the steady flow terms are subtracted from the Bernoulli equation for isentropic potential flow to give

$$P = -\left(i\omega\phi' + M\nabla\bar{\phi}\bullet\nabla\phi'\right) \tag{3.9}$$

where $P = P^*/(\rho M c_0^2)$ and ρ is the fluid density.

3.1.3 The Convected Wave Equation

Before proceeding with the development of the finite element model based on the above acoustic-flow equations, it is of interest to look at the convected wave

equation with uniform flow in a straight duct. For the case of three-dimensional waves propagating within the duct, the equations of continuity and momentum and the isentropic pressure-density relation can be combined to give the convected wave equation (reference [42], Chapter 1)

$$\left(\frac{D^2}{Dt^{*2}} - c_0^2\nabla^2\right) p^* = 0 \tag{3.10}$$

where $p*$ is the acoustic pressure defined as $P^* e^{i\omega^* t^*}$. The material derivative D/Dt^* is defined by

$$\frac{D}{Dt^*} = \frac{\partial}{\partial t^*} + \bar{U}^* \frac{\partial}{\partial x^*} \tag{3.11}$$

and $\bar{U}^*$ is the uniform flow velocity in the x direction—taken along the longitudinal axis of the duct. A similar equation can be derived in terms of the velocity potential

$$\left(\frac{D^2}{Dt^{*2}} - c_0^2\nabla^2\right) \phi''^* = 0. \tag{3.12}$$

Using the non-dimensional quantities defined in Section 3.1.2 and again assuming a harmonic time dependence leads to the equation

$$\nabla^2\phi' - M^2\frac{\partial^2\phi'}{\partial x^2} + \omega^2\phi' - 2iM\omega\frac{\partial\phi'}{\partial x} = 0. \tag{3.13}$$

In this equation M is not necessarily small. The non-dimensional flow velocity potential for uniform flow in the duct can be given by $\bar{\phi} = x + 1$ (refer to Section 2.4.2) so that $\nabla\bar{\phi}$ is then just the unit vector in the x direction. Substituting this into Equation 3.8 gives

$$\nabla^2\phi' + \omega^2\phi' - 2iM\omega\frac{\partial\phi'}{\partial x} = 0. \tag{3.14}$$

Equation 3.13 contains one additional term not found in Equation 3.14. Expanding the $\nabla^2\phi'$ terms then shows that the $\partial^2\phi'/\partial x^2$ term has the coefficient $1 - M^2$ in Equation 3.13 which was derived from the uniform flow convected wave equation.

This same term has a coefficient of unity in Equation 3.14 obtained from Equation 3.8 in the potential flow derivation of Section 3.1.2. Examination of the terms of $O[\alpha^2]$ which were neglected in obtaining Equation 3.8 and Equation 3.14 revealed a term

$$-M^2\nabla\left(\nabla\bar{\phi}\bullet\nabla\phi'\right)\bullet\nabla\bar{\phi} \tag{3.15}$$

which indeed does reduce to the missing term in Equation 3.14 for uniform flow in a straight duct. For Mach numbers of 0.1, there will only be a one percent difference in the coefficient of the $\partial^2\phi'/\partial x^2$ term in Equations 3.13 and 3.14. The inclusion of the above higher order term and other terms of the same order would significantly increase the complexity of the resulting equation. Thus Equation 3.8, as used by Peat [45], has been used here to develop the finite element acoustic-flow model. Within the connecting straight ducts, however, analytical solutions based on the convected wave equation for uniform flow have been used.

3.1.4 The Acoustic-Flow FEM Development

The development of the FEM model for the steady potential flow problem governed by Equation 3.7 has been considered in Section 2.4. In this section the FEM solution to the acoustic problem governed by Equation 3.8 is developed. As in Chapter 2, the Galerkin method is used here, and the approximate finite element solutions are

$$\bar{\phi} = \langle N\rangle\left\{\bar{\phi}_g\right\} \qquad \text{and} \qquad \phi' = \langle N\rangle\left\{\phi'_g\right\} \tag{3.16}$$

where $\left\{\phi'_g\right\}$ is the vector of nodal acoustic velocity potential and derivative quantities and $\left\{\bar{\phi}_g\right\}$ is the vector of known nodal flow velocity potential and derivative quantities calculated using the FEM developed in Section 2.4. Substituting this approximate solution into Equation 3.8 gives the residual error

$$R = \nabla^2\phi' + \omega^2\phi' - 2\mathrm{i}M\omega\nabla\bar{\phi}\bullet\nabla\phi'. \tag{3.17}$$

The residual error is then minimized by making R orthogonal to the finite element shape functions which yields

$$\iiint_V \{N\} \left(\nabla^2\phi' + \omega^2\phi' - 2iM\omega\nabla\bar{\phi} \bullet \nabla\phi'\right) dv = \{0\}. \tag{3.18}$$

The order of the first term is reduced by using Green's first identity to give

$$\iint_S \{N\}\frac{d\phi'}{dn}\, ds - \iiint_V \nabla\{N\} \bullet \nabla\phi'\, dv + \iiint_V \left(\omega^2\{N\}\phi' - 2iM\omega\{N\}\nabla\bar{\phi} \bullet \nabla\phi'\right) dv = \{0\}. \tag{3.19}$$

If the approximate FEM solutions given by Equation 3.16 are substituted into the volume terms this becomes

$$\iiint_V \left(\nabla\{N\} \bullet \nabla\langle N\rangle - \omega^2\{N\}\langle N\rangle + 2iM\omega\{N\}\langle\bar{\phi}\rangle\nabla\{N\} \bullet \nabla\langle N\rangle\right) dv \left\{\phi'_g\right\} = \iint_S \{N\}\frac{d\phi'}{dn}\, ds. \tag{3.20}$$

The right hand side of this equation will be treated later for specific boundary conditions. This equation is integrated on an element basis and the resulting element matrices assembled into a global matrix equation.

The element matrices for the first two terms of Equation 3.20 were developed in Section 2.3.1 when looking at the acoustic eigenvalue problem with no flow, but for completeness will be included here. The element acoustic "stiffness" matrix $[S_e]$, the acoustic "mass" matrix $[P_e]$ and the flow "damping" matrix $[C_e]$ are defined by

$$\begin{aligned}
[S_e] &= \iiint_{V_e} \nabla\{N\} \bullet \nabla\langle N\rangle\, dx\, dy\, dz \\
[P_e] &= \iiint_{V_e} \{N\}\langle N\rangle\, dx\, dy\, dz \\
[C_e] &= \iiint_{V_e} \{N\}\langle\bar{\phi}\rangle\nabla\{N\} \bullet \nabla\langle N\rangle\, dx\, dy\, dz.
\end{aligned} \tag{3.21}$$

In terms of the ISOHERM32 element shape functions (refer to Section 2.2) integrated in the element domain gives

$$[S_e] = [J_g]^T \int_{-1}^{1}\int_{-1}^{1}\int_{-1}^{1} [M]^T \left[J^{-1}\right]^T \left[J^{-1}\right] [M] \, |J| \; d\xi \, d\gamma \, d\zeta \; [J_g]$$

$$[P_e] = [J_g]^T \int_{-1}^{1}\int_{-1}^{1}\int_{-1}^{1} \{F\} \langle F \rangle \, |J| \; d\xi \, d\gamma \, d\zeta \; [J_g] \tag{3.22}$$

$$[C_e] = [J_g]^T \int_{-1}^{1}\int_{-1}^{1}\int_{-1}^{1} \{F\} \langle \tilde{\phi} \rangle [J_g]^T [M]^T \left[J^{-1}\right]^T \left[J^{-1}\right] [M] \, |J| \; d\xi \, d\gamma \, d\zeta \; [J_g]$$

Almost identical equations apply to the two-dimensional case using the quadrilateral ISOHERM12 element, with the exception that only double integrations are used, dropping $d\zeta$ and one integral from the above equations. Gauss-Legendre quadrature was used to carry out the element integrations. Four Gauss points were used in each dimension thus giving a 64 point scheme for the three-dimensional ISOHERM32 element and a 16 point scheme for the two-dimensional ISOHERM12 element. Refer to Section 2.3.1 for more detail.

The element matrices were assembled into a global matrix equation

$$\left([S] - \omega^2[P] + 2\mathrm{i}M\omega[C]\right) \left\{\phi'_g\right\} = \{Q\} \tag{3.23}$$

were the vector $\{Q\}$ comes from the surface integral term of Equation 3.20 and will be discussed subsequently for different boundary conditions.

3.1.5 Solution with Plane Wave Boundary Conditions

An example flow model of a duct junction is given in Figure 2.11, which shows a junction with a single flow inlet and two outlets connected to straight ducts assumed to be infinitely long or anechoically terminated. This model could represent a duct bend or nonuniform duct section if only one outlet was used. The acoustic-flow model development to be considered here is restricted to plane acoustic waves

propagating within the connecting straight ducts. This model is applicable when the frequencies of the sound are below the cut-on frequency at which higher order modes will propagate and where the finite element model interfaces to connecting ducts are far enough from the junction or bend so that any evanescent modes generated have decayed to negligible values. This cut-on frequency will be discussed in the subsequent section concerning higher order mode propagation.

At one of the connecting duct boundaries it will be assumed that the acoustic velocity, or the incident wave is specified. At the others, which are anechoically terminated, only an outward propagating wave will occur, moving away from the component under consideration. The present work will consider only rigid walled components so that $d\phi'/dn$ will be zero at the duct walls. The surface integral term on the right hand side of Equation 3.20 will thus be zero along the duct walls. Nonzero surface integral terms will occur at the connecting straight duct interfaces.

3.1.5.1 A Specified Acoustic Particle Velocity

The simplest plane wave boundary condition to specify is a constant normal acoustic velocity or constant $d\phi'/dn$ over the interface surface. For example, say the acoustic particle velocity normal to the surface is U^*. Then

$$\frac{d\phi'}{dn} = U = \frac{U^*}{Mc_0} \tag{3.24}$$

where U is defined as the non-dimensional acoustic particle velocity. The element vector $\{Q_e\}$ contributing to the source vector $\{Q\}$ in the global model (Equation 3.23) is given by

$$\{Q_e\} = U \iint_{S_e} \{N\}\, ds. \tag{3.25}$$

Integrating in the element domain with the three-dimensional ISOHERM32 element, on a surface of constant ζ for example, gives

$$\{Q_e\} = U\,[J_g]^T \int_{-1}^{1}\int_{-1}^{1} \{F\}\, J_s\, d\xi\, d\gamma \tag{3.26}$$

where J_s is the surface Jacobian given by Equation 2.52. In a subsequent paragraph the global matrix equation given by Equation 3.23 is split into real and imaginary parts. If $\{Q_e\} = \{Q_e^r\} + \mathrm{i}\{Q_e^i\}$ where $\{Q_e^r\}$ and $\{Q_e^i\}$ have all real elements then

$$\begin{aligned} \{Q_e^r\} &= U^r\,[J_g]^T \int_{-1}^{1}\int_{-1}^{1} \{F\}\, J_s\, d\xi\, d\gamma \\ \{Q_e^i\} &= U^i\,[J_g]^T \int_{-1}^{1}\int_{-1}^{1} \{F\}\, J_s\, d\xi\, d\gamma \end{aligned} \tag{3.27}$$

where U^r and U^i are the real and imaginary components of U.

In the two-dimensional formulation using the ISOHERM12 element, the real and imaginary parts of the element source vector are

$$\begin{aligned} \{Q_e^r\} &= U^r\,[J_g]^T \int_{-1}^{1} \{F\}\, J_\xi\, d\xi \\ \{Q_e^i\} &= U^i\,[J_g]^T \int_{-1}^{1} \{F\}\, J_\xi\, d\xi \end{aligned} \tag{3.28}$$

on a surface of constant γ where J_ξ was defined in Equation 2.56.

3.1.5.2 An Anechoic Termination

In order to obtain the boundary condition for an anechoically terminated straight duct interfaced to the finite element model, it is first necessary to develop the solution for plane wave propagation in a straight duct with flow. The equation governing plane wave propagation in the straight ducts can be obtained from Equation 3.13 by allowing quantities to only vary in the x direction (along the

longitudinal axis of the duct). This gives the second order ordinary differential equation

$$(1 - M^2)\frac{d^2\phi'}{dx^2} - 2iM\omega\frac{d\phi'}{dx} + \omega^2\phi' = 0. \tag{3.29}$$

The general solution to this equation is

$$\phi' = A_1 e^{-i\omega x/(1+M)} + A_2 e^{+i\omega x/(1-M)} \tag{3.30}$$

where A_1 and A_2 are undetermined constants depending on the boundary conditions. The first term represents a plane wave travelling in the positive x direction with a speed of Mach $1 + M$ (where M is positive if the flow is in the positive x direction). The second term represents a plane wave travelling in the negative x direction with a speed of Mach $1 - M$.

Equation 3.29 was derived from the convected wave equation. It is of interest to also look at the solution of Equation 3.8, the potential flow equation with small Mach numbers which was used in the FEM model development. Reduced to plane wave propagation with uniform flow in a straight duct, the resulting equation is the same as Equation 3.29 with the exception that M^2 is dropped from the first term. The solution to this equation is given by

$$\phi' = A_1 e^{-i\omega\left(\sqrt{M^2+1}-M\right)x} + A_2 e^{+i\omega\left(\sqrt{M^2+1}+M\right)x} \tag{3.31}$$

For Mach numbers of 0.1 or less, the difference in the solutions given by Equation 3.30 and Equation 3.32 should be small. This will be considered further in a subsequent section on testing the FEM model.

Figure 3.1 shows the j^{th} straight duct attached to a finite element model. The equations in the finite element domain have been non-dimensionalized based on the Mach number M and the dimension d. The straight duct solution has been

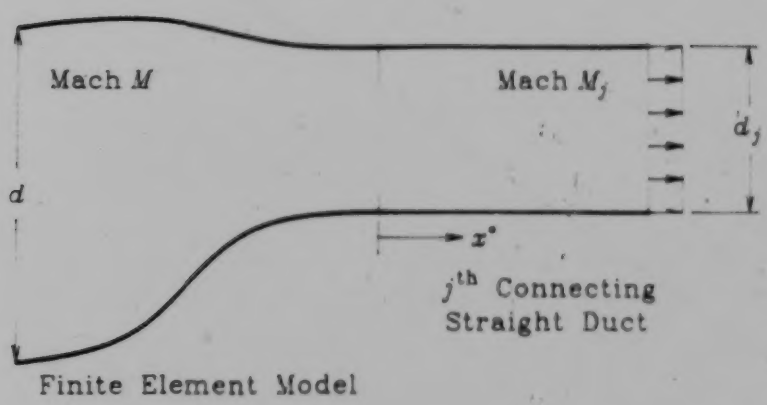

Figure 3.1 Linking the FEM Model to a Straight Duct

non-dimensionalized based on the Mach number M_j within the straight duct and the dimension d_j. In the following discussion the subscript s will indicate quantities non-dimensionalized based on the straight duct parameters. The non-dimensional acoustic velocity potential in the straight duct based on Equation 3.30 is then

$$\phi' = A_1 e^{-i\omega_s x_s/(1+M_j)} + A_2 e^{+i\omega_s x_s/(1-M_j)}. \tag{3.32}$$

The non-dimensional quantities in the finite element model and the connecting straight duct are related to the dimensional quantities

$$x^* = x_s d_j = x\, d, \quad \omega^* = \frac{c_0}{d_j}\omega_s = \frac{c_0}{d}\omega \quad \text{and} \quad \phi'^* = M_j c_0 d_j \phi'_s = M c_0 d \phi'. \tag{3.33}$$

The non-dimensional quantities in the two domains are then related by

$$x_s = \frac{d}{d_j}x, \quad \omega_s = \frac{d_j}{d}\omega \quad \text{and} \quad \phi' = \frac{M_j d_j}{Md}\phi'_s \tag{3.34}$$

Substituting the expressions for x_s and ω_s into Equation 3.32 and then solving for the acoustic velocity potential ϕ' based on the FEM parameters gives

$$\phi' = \frac{M_j d_j}{Md}\left(A_1 e^{-i\omega x/(1+M_j)} + A_2 e^{+i\omega x/(1-M_j)}\right) \tag{3.35}$$

The multiplicative term outside the brackets can be combined with the constants A_1 and A_2 to obtain

$$\phi' = B_1 e^{-i\omega x/(1+M_j)} + B_2 e^{+i\omega x/(1-M_j)} \tag{3.36}$$

which can be used to develop the linking duct boundary conditions in terms of the finite element model non-dimensional quantities.

If the j^{th} connecting duct has an anechoic termination, then a plane wave will propagate in the duct away from the finite element model and there will be no wave reflected back down the straight duct into the finite element model. For this case the velocity potential in the straight duct shown in Figure 3.1 reduces to

$$\phi' = B_1 e^{-i\omega x/(1+M_j)} \tag{3.37}$$

where M_j is taken as positive in the direction of the outward directed normal. The normal derivative to the surface is given by

$$\frac{d\phi'}{dn} = \frac{d\phi'}{dx} = -\frac{i\omega\phi'}{1+M_j}. \tag{3.38}$$

The surface integral term at the interface with the j^{th} connecting straight duct, for the specified acoustic velocity boundary condition, contributed to the source vector Q in the global matrix equation given by Equation 3.23. For the case of an anechoic termination this surface integral term is now

$$\iint_{S_i} \{N\} \frac{d\phi'}{dn}\, ds = -\frac{i\omega}{1+M_j} \iint_{S_i} \{N\}\langle N\rangle\, ds \left\{\phi'_g\right\}. \tag{3.39}$$

In this case the term contains the unknown nodal acoustic velocity and derivative vector $\left\{\phi'_g\right\}$ and contributes to a new matrix $[A]$ which is a boundary damping matrix to be added to the left hand side of Equation 3.23. The element matrix $[A_e]$ will be defined by

$$[A_e] = \frac{1}{1+M_j} \iint_{S_e} \{N\}\langle N\rangle\, ds. \tag{3.40}$$

Integrating in the element domain with the three-dimensional ISOHERM32 element, on a surface of constant ζ for example, gives

$$[A_e] = \frac{1}{1+M_j}[J_g]^T \int_{-1}^{1}\int_{-1}^{1} \{F\}\langle F\rangle J_s \, d\xi \, d\gamma \, [J_g] \tag{3.41}$$

where J_s was defined in Equation 2.52. In the two-dimensional formulation using the ISOHERM12 element, the element boundary damping matrix for the anechoic termination is given by

$$[A_e] = \frac{1}{1+M_j}[J_g]^T \int_{-1}^{1} \{F\}\langle F\rangle J_\xi \, d\xi \, [J_g] \tag{3.42}$$

on a surface of constant γ where J_ξ was defined in Equation 2.56.

3.1.5.3 Incident Wave Specified

The last plane wave boundary condition to be considered is that of a specified incident plane wave within an anechoically terminated straight duct. This type of boundary condition is used when finding the plane wave transmission loss of a given component. Again considering the geometry shown in Figure 3.1, the velocity potential for this case is

$$\phi' = B_{\text{refl}} e^{-i\omega x/(1+M_j)} + B_{\text{inc}} e^{+i\omega x/(1-M_j)} \tag{3.43}$$

where the subscripts refer to the incident and reflected waves. The normal derivative of ϕ' at the connecting interface is then

$$\frac{d\phi'}{dn} = \frac{d\phi'}{dx} = -\frac{i\omega}{1+M_j} B_{\text{refl}} e^{-i\omega x/(1+M_j)} + \frac{i\omega}{1-M_j} B_{\text{inc}} e^{+i\omega x/(1-M_j)}. \tag{3.44}$$

Evaluating Equation 3.43 and Equation 3.44 at the interface ($x = 0$) gives

$$\begin{aligned} \phi' &= B_{\text{refl}} + B_{\text{inc}} \\ \frac{d\phi'}{dn} &= -\frac{i\omega}{1+M_j} B_{\text{refl}} + \frac{i\omega}{1-M_j} B_{\text{inc}} \end{aligned} \tag{3.45}$$

Eliminating B_{refl} from these equations results in

$$\frac{d\phi'}{dn} = -\frac{i\omega\phi'}{1+M_j} + i\omega\left(\frac{1}{1-M_j} + \frac{1}{1+M_j}\right) B_{\text{inc}}. \tag{3.46}$$

The surface integral term on the right hand side of Equation 3.20 integrated over the interface with the j^{th} straight duct then becomes

$$\begin{aligned}\iint_{S_j} \{N\}\frac{d\phi'}{dn}\, ds = &-\frac{i\omega}{1+M_j}\iint_{S_j} \{N\}\langle N\rangle\, ds\, \{\phi'_g\} \\ &+ i\omega\left(\frac{1}{1-M_j} + \frac{1}{1+M_j}\right) B_{\text{inc}} \iint_{S_j} \{N\}\, ds.\end{aligned} \tag{3.47}$$

The first term on the right hand side of this equation is identical to that obtained for the anechoic termination and leads to an element boundary damping matrix $[A_e]$ identical to that given by Equation 3.42. The second term gives a contribution to the source vector Q in the global matrix equation. Integrating this term in the element domain with the three-dimensional ISOHERM32 element, on a surface of constant ζ for example, gives real and imaginary components

$$\begin{aligned}\{Q_e^r\} &= -\omega\left(\frac{1}{1-M_j} + \frac{1}{1+M_j}\right) B_{\text{inc}}^i [J_g]^T \int_{-1}^{1}\int_{-1}^{1} \{F\} J_s\, d\xi\, d\gamma \\ \{Q_e^i\} &= \omega\left(\frac{1}{1-M_j} + \frac{1}{1+M_j}\right) B_{\text{inc}}^r [J_g]^T \int_{-1}^{1}\int_{-1}^{1} \{F\} J_s\, d\xi\, d\gamma\end{aligned} \tag{3.48}$$

of the element source vector $\{Q_e\}$ for the specified incident wave boundary condition where B_{inc}^r and B_{inc}^i are the real and imaginary parts of B_{inc}. In the two-dimensional formulation using the ISOHERM12 element, the real and imaginary parts of the element source vector for this boundary condition are then given by

$$\begin{aligned}\{Q_e^r\} &= -\omega\left(\frac{1}{1-M_j} + \frac{1}{1+M_j}\right) B_{\text{inc}}^i [J_g]^T \int_{-1}^{1} \{F\} J_\xi\, d\xi \\ \{Q_e^i\} &= \omega\left(\frac{1}{1-M_j} + \frac{1}{1+M_j}\right) B_{\text{inc}}^r [J_g]^T \int_{-1}^{1} \{F\} J_\xi\, d\xi\end{aligned} \tag{3.49}$$

on a surface of constant γ.

3.1.5.4 Equation Solution Using Real Quantities

The complete global matrix equation for the acoustic-flow problem with plane wave inputs and outputs and rigid walled ducts is obtained by adding the connecting duct boundary damping matrix $[A]$ to Equation 3.23 to give

$$\left([S] - \omega^2[P] + 2\mathrm{i}M\omega[C] + \mathrm{i}\omega[A]\right)\left\{\phi'_g\right\} = \{Q\} \tag{3.50}$$

The computer language used for this work did not support the use of complex arithmetic, so that the complex equations had to be reformed in terms of real quantities. By splitting the acoustic velocity potential vector $\left\{\phi'_g\right\}$ and the source vector $\{Q\}$ into real and imaginary parts, Equation 3.50 can be separated into real and imaginary terms to give the following equations

$$\begin{aligned} \left([S] - \omega^2[P]\right)\left\{\phi'_g\right\}^{\mathrm{r}} - \left(2M\omega[C] + \omega[A]\right)\left\{\phi'_g\right\}^{\mathrm{i}} &= \{Q^{\mathrm{r}}\} \\ \left(2M\omega[C] + \omega[A]\right)\left\{\phi'_g\right\}^{\mathrm{r}} + \left([S] - \omega^2[P]\right)\left\{\phi'_g\right\}^{\mathrm{i}} &= \{Q^{\mathrm{i}}\} \end{aligned} \tag{3.51}$$

which can be combined to give the matrix equation

$$\begin{bmatrix} \left([S] - \omega^2[P]\right) & \left(-2M\omega[C] - \omega[A]\right) \\ \left(2M\omega[C] + \omega[A]\right) & \left([S] - \omega^2[P]\right) \end{bmatrix} \begin{Bmatrix} \left\{\phi'_g\right\}^{\mathrm{r}} \\ \left\{\phi'_g\right\}^{\mathrm{i}} \end{Bmatrix} = \begin{Bmatrix} \{Q^{\mathrm{r}}\} \\ \{Q^{\mathrm{i}}\} \end{Bmatrix} \tag{3.52}$$

The matrices in this global equation are formed by assembling the element volume and surface matrices using the conventional FEM assembly procedure. In the ISOHERM32 and ISOHERM12 element models separate connectivity matrices must be used to assign the global geometric nodes and the velocity potential nodes to the elements within the model. This has the advantage that on a plane wave boundary termination, several geometric nodes can be assigned to a single velocity potential node since the acoustic and flow velocity potentials are constant over the uniform flow, plane wave interface. Further reductions in the DOF can also be made by

applying constraint equations to force the acoustic and flow velocities at nodes on the rigid boundaries to be parallel to the boundaries.

3.1.6 Solution with Higher Order Mode Boundary Conditions

In order to extend the solution to frequencies above the cut-on frequency for higher order modes it is necessary to consider higher order mode propagation within the connecting straight ducts. The present work considers only rigid walled connecting ducts and uniform flow within these ducts. The exact solution within the straight ducts will be developed first.

3.1.6.1 Higher Order Modes in a Straight Duct with Uniform Flow

This section looks at the propagation of higher order modes within a straight duct with a uniform cross-section of arbitrary shape and uniform flow. The geometry of the model is show in Figure 3.2 with the $x-$axis along the longitudinal axis of the duct. The governing equation for this problem was developed in Section 3.1.3 and is given by Equation 3.13 which was derived from the convected wave equation assuming a harmonic time dependence. A separation of variables solution of form

$$\phi' = X(x)\Phi(y,z) \tag{3.53}$$

can be used. This leads to two equations, the first is given by

$$\frac{\partial^2\Phi}{\partial y^2} + \frac{\partial^2\Phi}{\partial z^2} + \omega_c^2\Phi = 0 \tag{3.54}$$

which is the two-dimensional Helmholtz equation for the duct cross-section. The FEM solution of this equation was considered in Section 2.3.1. The mode shape and eigenvalue for the m^{th} mode are defined respectively as $\Phi_m(y,z)$ and ω_{c_m} with the eigenvalues ordered from smallest to largest with increasing m. The second equation can be used to find X and is given by

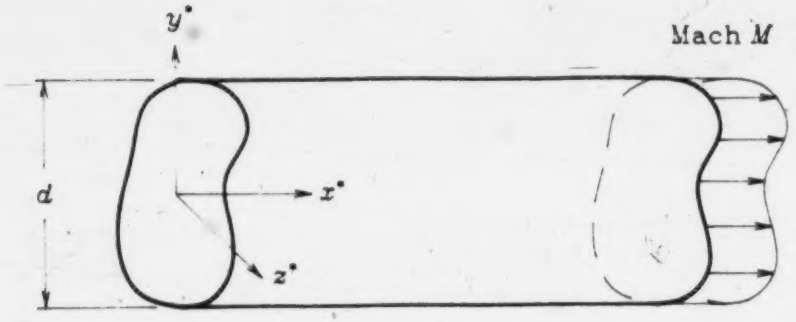

Figure 3.2 Straight Duct with a Uniform Cross-section

$$(1-M^2)\frac{d^2X}{dx^2} - 2iM\omega\frac{dX}{dx} + (\omega^2 - \omega_{c_m}^2)\,X = 0. \tag{3.55}$$

Letting $X = e^{-i\omega_m x}$ and substituting into Equation 3.55 then yields a quadratic equation which can be solved for the values of ω_m given by

$$\omega_m = \frac{-\omega M \mp \sqrt{\omega^2 - (1-M^2)\,\omega_{c_m}^2}}{1-M^2}. \tag{3.56}$$

The general solution can then be given as

$$\phi' = \sum_{m=0}^{\infty} \Phi_m(y,z)\left(A_{1m}e^{-i\omega_m^+ x} + A_{2m}e^{+i\omega_m^- x}\right) \tag{3.57}$$

where

$$\omega_m^{\pm} = \frac{\mp\omega\,(M \mp \alpha_m)}{1-M^2} \quad \text{and} \quad \alpha_m = \sqrt{1-(1-M^2)\frac{\omega_{c_m}^2}{\omega^2}}. \tag{3.58}$$

For the lowest mode ($m = 0$) the frequency parameter $\omega_{c_0} = 0$ and Φ_0 is constant over the cross-section. The terms of Equation 3.57 with $m = 0$ then reduce to the solution for plane wave propagation given by Equation 3.30. For the higher order modes ($m > 0$), if α_m is real then the terms of Equation 3.57 correspond to progressive waves which propagate unattenuated. This occurs when the frequency is above the cut-on frequency given by

$$\omega = \omega_{c_m}\sqrt{1-M^2} \tag{3.59}$$

which decreases as the flow velocity increases and is independent of the direction of flow. If there is no flow ($M = 0$), then the cut-on frequency for the m^{th} mode is ω_{c_m}. Below the cut-on frequency $\omega_m^{\pm}$ are complex (entirely imaginary if there is no flow) and the modes are then referred to as evanescent waves which decay with distance along the duct. The terms of Equation 3.57 with ω_m^+ in the exponent decay exponentially in the negative x direction and terms with ω_m^- in the exponent decay exponentially in the positive x direction. The rate of decay increases as the driving frequency ω becomes smaller.

3.1.6.2 Higher Order Mode Anechoic Termination

The right hand side of the governing acoustic equation for the FEM acoustic-flow model (Equation 3.20) is a surface integral containing the normal derivative of the acoustic velocity potential $d\phi'/dn$. To evaluate this integral, $d\phi'/dn$ must be determined at the interfaces of the connecting straight ducts to the FEM model. Consider the j^{th} duct connecting to the model shown in Figure 3.1. As was done in looking at plane wave boundary conditions, the acoustic velocity potential within the straight duct, based on the connecting duct non-dimensional coordinates and frequency, must be converted to a formulation based on the quantities used in the FEM model. Above the cut-on frequency (α_m real) the outward propagating or transmitted wave is associated with the terms of Equation 3.57 with ω_m^+ in the exponent so that for the anechoically terminated j^{th} straight duct

$$\phi' = \sum_{m=0}^{\infty} \Phi_m(y_s, z_s) B_m^{\text{trans}} e^{-i\omega_m^+ x} \tag{3.60}$$

where

$$\omega_m^+ = -\frac{\omega(M_j - \alpha_m)}{1 - M_j^2} \quad \text{and} \quad \alpha_m = \sqrt{1 - \left(1 - M_j^2\right) \frac{\omega_{c_m}^2 d^2}{\omega^2 d_j^2}}. \tag{3.61}$$

Below the cut-on frequency (α_m imaginary), so that the evanescent mode decays moving outward from the FEM model, the terms of Equation 3.57 with ω_m^- in the exponent must be used. This is equivalent to using Equation 3.60 with

$$\begin{aligned} \omega_{m_r}^+ &= -\frac{\omega M_j}{1-M_j^2} \\ \omega_{m_i}^+ &= -\frac{\omega}{1-M_j^2}\sqrt{\left(1-M_j^2\right)\frac{\omega_{c_m}^2 d^2}{\omega^2 d_j^2}-1} \end{aligned} \tag{3.62}$$

where $\omega_{m_r}^+$ and $\omega_{m_i}^+$ are the real and imaginary parts of ω_m^+. The normal derivative of ϕ' is then

$$\frac{d\phi'}{dn} = \frac{d\phi'}{dx} = \sum_{m=0}^{\infty} \Phi_m(y_s, z_s)\left(-\mathrm{i}B_m^{\mathrm{trans}}\omega_m^+\right) e^{-\mathrm{i}\omega_m^+ x}. \tag{3.63}$$

At the FEM model interface to the straight duct ($x = 0$) the acoustic velocity potential reduces to

$$\phi' = \sum_{m=0}^{\infty} \Phi_m(y_s, z_s) B_m^{\mathrm{trans}} \tag{3.64}$$

and the normal derivative

$$\frac{d\phi'}{dn} = \frac{d\phi'}{dx} = \sum_{m=0}^{\infty} \Phi_m(y_s, z_s)\left(-\mathrm{i}B_m^{\mathrm{trans}}\omega_m^+\right) \tag{3.65}$$

The last two equations will be used in Section 3.1.6.4 in the development of the FEM model of a duct junction with higher order mode boundary conditions.

3.1.6.3 Higher Order Mode Incident Wave Termination

Again consider the j^{th} duct connecting to the FEM model shown in Figure 3.1. For the specified incident wave termination, the terms of Equation 3.57 with ω_m^- in the exponent form the incident wave and the terms with ω_m^+ in the exponent form the reflected wave. The acoustic velocity potential in the straight duct is then

$$\phi' = \sum_{m=0}^{\infty} \Phi_m(y_s, z_s)\left(B_m^{\mathrm{refl}} e^{-\mathrm{i}\omega_m^+ x} + B_m^{\mathrm{inc}} e^{+\mathrm{i}\omega_m^- x}\right) \tag{3.66}$$

where ω_m^+ is real and given by Equation 3.61 above the cut-on frequency. Below the cut-on frequency, ω_m^+ is complex and given by Equation 3.62. Similarly ω_m^- is real above the cut-on frequency and given by

$$\omega_m^- = \frac{\omega\left(M_j + \alpha_m\right)}{1 - M_j^2}. \tag{3.67}$$

Below the cut-on frequency the real and imaginary parts of ω_m^- are

$$\begin{aligned} \omega_{m_r}^- &= \frac{\omega M_j}{1 - M_j^2} \\ \omega_{m_i}^- &= \frac{\omega}{1 - M_j^2}\sqrt{\left(1 - M_j^2\right)\frac{\omega_{c_m}^2 d^2}{\omega^2 d_j^2} - 1}. \end{aligned} \tag{3.68}$$

The solutions below the cut-on frequency have been selected so that the incident evanescent modes decay moving toward the FEM model and the reflected modes decay moving away from the model. The normal derivative of the acoustic velocity potential is then

$$\frac{d\phi'}{dn} = \frac{d\phi'}{dx} = \sum_{m=0}^{\infty} \Phi_m(y_s, z_s)\left(-\mathrm{i}\omega_m^+ B_m^{\mathrm{refl}} e^{-\mathrm{i}\omega_m^+ x} + \mathrm{i}\omega_m^- B_m^{\mathrm{inc}} e^{+\mathrm{i}\omega_m^- x}\right). \tag{3.69}$$

Evaluating the equation for ϕ' and $\frac{d\phi'}{dn}$ at the connecting duct interface to the model ($x = 0$) gives

$$\phi' = \sum_{m=0}^{\infty} \Phi_m(y_s, z_s)\left(B_m^{\mathrm{refl}} + B_m^{\mathrm{inc}}\right) \tag{3.70}$$

and

$$\frac{d\phi'}{dn} = \frac{d\phi'}{dx} = \sum_{m=0}^{\infty} \Phi_m(y_s, z_s)\left(-\mathrm{i}\omega_m^+ B_m^{\mathrm{refl}} + \mathrm{i}\omega_m^- B_m^{\mathrm{inc}}\right) \tag{3.71}$$

These last two equations are used to develop the FEM models of a duct junction in the following section.

3.1.6.4 Junction with Incident Wave and Anechoic Terminations

Consider the FEM model of a duct junction shown in Figure 2.11. In this model it is assumed that there is a known incident wave in a straight connecting duct

at Station 1 and anechoic straight duct terminations at Station 2 and Station 3. This model will be used to illustrate the equation development. The resulting equations have also been programmed with only one outlet to solve duct bend problems. The equations developed could easily be extended to model junctions with four or more connecting ducts. Station 1 does not necessarily have to be the flow inlet. The directions of flow can be selected arbitrarily, provided the resulting flow boundary conditions satisfy mass continuity.

The modal matrix $[\Phi]_1$ of FEM model mode shapes will be used for the incident wave termination at Station 1 and defined as

$$[\Phi]_1 = [\{q_0\}\{q_1\}\{q_2\}\cdots\{q_n\}]_1. \tag{3.72}$$

The vectors $\{q_0\}, \{q_1\}, \{q_2\}\cdots\{q_n\}$ are the eigenvectors of nodal quantities for the terminating duct cross-section acoustic modes determined from the FEM solution of the eigenvalue problem. This problem is governed by the two-dimensional Helmholtz equation given by Equation 3.53 and was considered for two and three-dimensional problems in Section 2.3. The vector for the acoustic velocity potential and derivative nodal quantities at this termination is then given by

$$\{\phi'_g\}_1 = [\Phi]_1(\{a\} + \{b\}) \tag{3.73}$$

where $\{a\}$ is a vector defining the assumed known incident wave modal mixture and $\{b\}$ is the vector defining the unknown reflected wave modal mixture at the termination.

This discretized formulation is then used in Equation 3.70 and Equation 3.71 which leads to an equation for the acoustic velocity potential at any point on the terminating cross-section given by

$$\phi' = \langle N\rangle\{\phi'_g\}_1 = \langle N\rangle[\Phi]_1(\{a\} + \{b\}) \tag{3.74}$$

and the normal derivative of ϕ' by

$$\frac{d\phi'}{dn} = \mathbf{i}\langle N\rangle[\Phi]_1\left(\{\omega^- a\} - \{\omega^+ b\}\right) \tag{3.75}$$

where

$$\{\omega^+ a\} = \begin{Bmatrix} \omega_0^+ a_0 \\ \omega_1^+ a_1 \\ \omega_2^+ a_2 \\ \vdots \\ \omega_n^+ a_n \end{Bmatrix} \text{ and } \{\omega^- b\} = \begin{Bmatrix} \omega_0^- b_0 \\ \omega_1^- b_1 \\ \omega_2^- b_2 \\ \vdots \\ \omega_n^- b_n \end{Bmatrix}. \tag{3.76}$$

The wave number parameters $\omega_0^-, \omega_1^-, \omega_2^- \ldots \omega_n^-$ can be obtained using Equation 3.66 and Equation 3.67 and $\omega_0^+, \omega_1^+, \omega_2^+ \ldots \omega_n^+$ can be obtained using Equation 3.61, and Equation 3.62.

The source terms in the global matrix equation, given by Equation 3.20, associated with this termination are then

$$\{Q_1\} = \int_{S_1} \{N\}\frac{d\phi'}{dn}ds = \mathbf{i}\int_{S_1} \{N\}\langle N\rangle ds\,[\Phi]_1(\{\omega^- a\} - \{\omega^+ b\}). \tag{3.77}$$

Let

$$[\Phi\omega^+] = \left[\omega_1^+\{q_1\} \quad \omega_2^+\{q_2\} \quad \cdots \quad \omega_n^+\{q_n\}\right] \tag{3.78}$$

and

$$[\Phi\omega^-] = \left[\omega_1^-\{q_1\} \quad \omega_2^-\{q_2\} \quad \cdots \quad \omega_n^-\{q_n\}\right] \tag{3.79}$$

then

$$\{Q_1\} = \mathbf{i}[A_1]\left([\Phi\omega^-]_1\{a\} - [\Phi\omega^+]_1\{b\}\right) \tag{3.80}$$

where $[A_1] = \int_{S_1}\{N\}\langle N\rangle ds$. Similarly at the anechoic termination at Station 2, $\{\phi'_g\}_2 = [\Phi]_2\{c\}$ where $\{c\}$ is the vector defining the unknown transmitted modal mixture and Equation 3.65 gives $\{Q_2\} = -\mathbf{i}[A_2][\Phi\omega^+]_2\{c\}$. Also at the anechoic termination at Station 3, $\{\phi'_g\}_3 = [\Phi]_3\{d\}$ and $\{Q_3\} = -\mathbf{i}[A_3][\Phi\omega^+]_3\{d\}$ where $\{d\}$ defines the unknown transmitted modal mixture at this boundary. The matrices

$[A_1]$, $[A_2]$, $[A_3]$ are obtained by integrating on an element basis over each surface and assembling the element matrices into the associated global surface matrix. The element matrix is given by

$$[A_e] = [J_g]^T \int_{-1}^{1}\int_{-1}^{1} \{F\}(F) J_s \, d\xi \, d\gamma \, [J_g] \tag{3.81}$$

when integrated in the element domain over a surface of constant ζ using the three-dimensional ISOHERM32 element, and by

$$[A_e] = [J_g]^T \int_{-1}^{1} \{F\}(F) J_\xi \, d\xi \, [J_g] \tag{3.82}$$

when integrated along the edge of the two-dimensional ISOHERM12 element along a line of constant γ.

Note that $\{a\}$, $\{b\}$, $\{c\}$, $\{d\}$, $[M\omega^+]$ and $[M\omega^-]$ can be complex. The global matrix equation for the finite element model given by Equation 3.23 for hard walled ducts can be split into real and imaginary parts to give

$$\left([B^r] + i[B^i]\right)\left(\{\phi'_g\}^r + i\{\phi'_g\}^i\right) = \{Q^r\} + i\{Q^i\} \tag{3.83}$$

where $[B^r] = [S] - \omega^2[P]$ and $[B^i] = 2M\omega[C]$. In terms of all real quantities this can be expanded to obtain the equation

$$\begin{bmatrix} [B^r] & [-B^i] \\ [B^i] & [B^r] \end{bmatrix} \begin{Bmatrix} \{\phi'_g\}^r \\ \{\phi'_g\}^i \end{Bmatrix} = \begin{Bmatrix} \{Q^r\} \\ \{Q^i\} \end{Bmatrix}. \tag{3.84}$$

The vector $\{\phi'_g\}$ can be separated into internal node quantities $\{\phi_{int}\}$ and connecting boundary quantities $\{\phi_{bnd}\}$. Similarly $\{Q\}$ can be separated into internal and boundary quantities resulting in the equation

$$[BB] \begin{Bmatrix} \{\phi^r_{int}\} \\ \{\phi^r_{bnd}\} \\ \{\phi^i_{int}\} \\ \{\phi^i_{bnd}\} \end{Bmatrix} = \begin{Bmatrix} \{0\} \\ \{Q^r_{bnd}\} \\ \{0\} \\ \{Q^i_{bnd}\} \end{Bmatrix} \tag{3.85}$$

where the matrix $[BB]$ is defined as

$$[BB] = \begin{bmatrix} [B^r] & [-B^i] \\ [B^i] & [B^r] \end{bmatrix} \tag{3.86}$$

The order of the equations can be changed and partitioned between internal and boundary quantities to give

$$\begin{bmatrix} [D_{11}] & [D_{12}] \\ [D_{21}] & [D_{22}] \end{bmatrix} \begin{Bmatrix} \begin{Bmatrix} \phi^r_{int} \\ \phi^i_{int} \end{Bmatrix} \\ \begin{Bmatrix} \phi^r_{bnd} \\ \phi^i_{bnd} \end{Bmatrix} \end{Bmatrix} = \begin{Bmatrix} \begin{Bmatrix} 0 \\ 0 \end{Bmatrix} \\ \begin{Bmatrix} Q^r_{bnd} \\ Q^i_{bnd} \end{Bmatrix} \end{Bmatrix}. \tag{3.87}$$

This is equivalent to the following equations:

$$\begin{aligned} [D_{11}] \begin{Bmatrix} \phi^r_{int} \\ \phi^i_{int} \end{Bmatrix} + [D_{12}] \begin{Bmatrix} \phi^r_{bnd} \\ \phi^i_{bnd} \end{Bmatrix} &= \begin{Bmatrix} 0 \\ 0 \end{Bmatrix} \\ [D_{21}] \begin{Bmatrix} \phi^r_{int} \\ \phi^i_{int} \end{Bmatrix} + [D_{22}] \begin{Bmatrix} \phi^r_{bnd} \\ \phi^i_{bnd} \end{Bmatrix} &= \begin{Bmatrix} Q^r_{bnd} \\ Q^i_{bnd} \end{Bmatrix}. \end{aligned} \tag{3.88}$$

The first equation can be solved for the internal unknowns to yield

$$\begin{Bmatrix} \phi^r_{int} \\ \phi^i_{int} \end{Bmatrix} = -[D_{11}]^{-1}[D_{12}] \begin{Bmatrix} \phi^r_{bnd} \\ \phi^i_{bnd} \end{Bmatrix}, \tag{3.89}$$

which can be used in the second equation to eliminate the internal unknowns giving

$$[E] \begin{Bmatrix} \phi^r_{bnd} \\ \phi^i_{bnd} \end{Bmatrix} = \begin{Bmatrix} Q^r_{bnd} \\ Q^i_{bnd} \end{Bmatrix} \tag{3.90}$$

where

$$[E] = [D_{22}] - [D_{21}][D_{11}]^{-1}[D_{12}]. \tag{3.91}$$

The boundary vectors can be expanded to give

$$[E] \begin{Bmatrix} \{\phi'_g\}^r_1 \\ \{\phi'_g\}^r_2 \\ \{\phi'_g\}^r_3 \\ \{\phi'_g\}^i_1 \\ \{\phi'_g\}^i_2 \\ \{\phi'_g\}^i_3 \end{Bmatrix} = \begin{Bmatrix} \{Q^r_1\} \\ \{Q^r_2\} \\ \{Q^r_3\} \\ \{Q^i_1\} \\ \{Q^i_2\} \\ \{Q^i_3\} \end{Bmatrix}. \tag{3.92}$$

The vectors $\{\phi'_g\}_j$ can be replaced using the following equations in terms of $\{a\}$, $\{b\}$, $\{c\}$, and $\{d\}$:

$$\begin{aligned} \{\phi'_g\}^r_1 &= [\Phi]_1\{a^r\} + [\Phi]_1\{b^r\} & \{\phi'_g\}^i_1 &= [\Phi]_1\{a^i\} + [\Phi]_1\{b^i\} \\ \{\phi'_g\}^r_2 &= [\Phi]_2\{c^r\} & \{\phi'_g\}^i_2 &= [\Phi]_2\{c^i\} \\ \{\phi'_g\}^r_3 &= [\Phi]_3\{d^r\} & \{\phi'_g\}^i_3 &= [\Phi]_3\{d^i\}. \end{aligned} \tag{3.93}$$

Using Equation 3.80, the real and imaginary parts of the source vector $\{Q_1\}$ can be given by

$$\begin{aligned} \{Q^r_1\} &= [A_1]\left(-[\Phi\omega^-]^r_1\{a^i\} - [\Phi\omega^-]^i_1\{a^r\} + [\Phi\omega^+]^r_1\{b^i\} + [\Phi\omega^+]^i_1\{b^r\}\right) \\ \{Q^i_1\} &= [A_1]\left(+[\Phi\omega^-]^r_1\{a^r\} - [\Phi\omega^-]^i_1\{a^i\} - [\Phi\omega^+]^r_1\{b^r\} + [\Phi\omega^+]^i_1\{b^i\}\right). \end{aligned} \tag{3.94}$$

If the following matrices are defined

$$\begin{aligned} [D^+_1]^r &= [A_1][\Phi\omega^+]^r_1 & [D^+_1]^i &= [A_1][\Phi\omega^+]^i_1 \\ [D^-_1]^r &= [A_1][\Phi\omega^-]^r_1 & [D^-_1]^i &= [A_1][\Phi\omega^-]^i_1 \end{aligned} \tag{3.95}$$

then the real and imaginary parts of $\{Q_1\}$ become

$$\begin{aligned} \{Q^r_1\} &= -[D^-_1]^r\{a^i\} - [D^-_1]^i\{a^r\} + [D^+_1]^r\{b^i\} + [D^+_1]^i\{b^r\} \\ \{Q^i_1\} &= [D^-_1]^r\{a^r\} - [D^-_1]^i\{a^i\} - [D^+_1]^r\{b^r\} + [D^+_1]^i\{b^i\}. \end{aligned} \tag{3.96}$$

In a similar manner the real and imaginary parts of $\{Q_2\}$ and $\{Q_3\}$ can be given by

$$\begin{aligned} \{Q^r_2\} &= [D^+_2]^r\{c^i\} + [D^+_2]^i\{c^r\} \\ \{Q^i_2\} &= -[D^+_2]^r\{c^r\} + [D^+_2]^i\{c^i\} \\ \{Q^r_3\} &= [D^+_3]^r\{d^i\} + [D^+_3]^i\{d^r\} \\ \{Q^i_3\} &= -[D^+_3]^r\{d^r\} + [D^+_3]^i\{d^i\}. \end{aligned} \tag{3.97}$$

If the expressions for $\{\phi'_g\}_j$ from Equation 3.93 and for $\{Q_j\}$ from Equation 3.96 and Equation 3.97 are substituted into Equation 3.92 and the matrix E partitioned then

$$\begin{bmatrix} [E_{11}] & [E_{12}] & [E_{13}] & [E_{14}] & [E_{15}] & [E_{16}] \\ [E_{21}] & [E_{22}] & [E_{23}] & [E_{24}] & [E_{25}] & [E_{26}] \\ [E_{31}] & [E_{32}] & [E_{33}] & [E_{34}] & [E_{35}] & [E_{36}] \\ [E_{41}] & [E_{42}] & [E_{43}] & [E_{44}] & [E_{45}] & [E_{46}] \\ [E_{51}] & [E_{52}] & [E_{53}] & [E_{54}] & [E_{55}] & [E_{56}] \\ [E_{61}] & [E_{62}] & [E_{63}] & [E_{64}] & [E_{65}] & [E_{66}] \end{bmatrix} \begin{Bmatrix} [\Phi]_1\{a^r + b^r\} \\ [\Phi]_2\{c^r\} \\ [\Phi]_3\{d^r\} \\ [\Phi]_1\{a^i + b^i\} \\ [\Phi]_2\{c^i\} \\ [\Phi]_3\{d^i\} \end{Bmatrix}$$

$$= \begin{Bmatrix} -[D_1^-]^r\{a^i\} - [D_1^-]^i\{a^r\} + [D_1^+]^r\{b^i\} + [D_1^+]^i\{b^r\} \\ +[D_2^+]^r\{c^i\} + [D_2^+]^i\{c^r\} \\ +[D_3^+]^r\{d^i\} + [D_3^+]^i\{d^r\} \\ +[D_1^-]^r\{a^r\} - [D_1^-]^i\{a^i\} - [D_1^+]^r\{b^r\} + [D_1^+]^i\{b^i\} \\ -[D_2^+]^r\{c^r\} + [D_2^+]^i\{c^i\} \\ -[D_3^+]^r\{d^r\} + [D_3^+]^i\{d^i\} \end{Bmatrix}. \quad (3.98)$$

A matrix $[F]$ can the be defined by

$$[F] = [E] \begin{bmatrix} [\Phi]_1 & & & & & \\ & [\Phi]_2 & & & O & \\ & & [\Phi]_3 & & & \\ & & & [\Phi]_1 & & \\ & O & & & [\Phi]_2 & \\ & & & & & [\Phi]_3 \end{bmatrix} \quad (3.99)$$

where the elements outside the $[\Phi]_j$ sub-matrices in matrix on the right hand side of this equation are zeros.

If the matrix $[F]$ is partitioned and the terms containing the unknown vectors $\{b\}$, $\{c\}$ and $\{d\}$ moved to the left hand side of the equation and the terms

containing the known vector $\{a\}$ moved to the right hand side of the equation then

$$\begin{bmatrix} [F_{11}]-[D_1^+]^i & [F_{12}] & [F_{13}] & [F_{14}]-[D_1^+]^r \\ [F_{21}] & [F_{22}]-[D_2^+]^i & [F_{23}] & [F_{24}] \\ [F_{31}] & [F_{32}] & [F_{33}]-[D_3^+]^i & [F_{34}] \\ [F_{41}]+[D_1^+]^r & [F_{42}] & [F_{43}] & [F_{44}]-[D_1^+]^i \\ [F_{51}] & [F_{52}]+[D_2^+]^r & [F_{53}] & [F_{54}] \\ [F_{61}] & [F_{62}] & [F_{63}]+[D_3^+]^r & [F_{64}] \end{bmatrix}$$

$$\begin{bmatrix} [F_{15}] & [F_{16}] \\ [F_{25}]-[D_2^+]^r & [F_{26}] \\ [F_{35}] & [F_{36}]-[D_3^+]^r \\ [F_{45}] & [F_{46}] \\ [F_{55}]-[D_2^+]^i & [F_{56}] \\ [F_{65}] & [F_{66}]-[D_3^+]^i \end{bmatrix} \begin{Bmatrix} \{b^r\} \\ \{c^r\} \\ \{d^r\} \\ \{b^i\} \\ \{c^i\} \\ \{d^i\} \end{Bmatrix}$$

$$= \begin{Bmatrix} -[F_{11}]\{a^r\}-[F_{14}]\{a^i\}-[D_1^-]^r\{a^i\}-[D_1^-]^i\{a^r\} \\ -[F_{21}]\{a^r\}-[F_{24}]\{a^i\} \\ -[F_{31}]\{a^r\}-[F_{34}]\{a^i\} \\ -[F_{41}]\{a^r\}-[F_{44}]\{a^i\}+[D_1^-]^r\{a^r\}-[D_1^-]^i\{a^i\} \\ -[F_{51}]\{a^r\}-[F_{54}]\{a^i\} \\ -[F_{61}]\{a^r\}-[F_{64}]\{a^i\} \end{Bmatrix}$$

$$= -\begin{bmatrix} [F_{11}]+[D_1^-]^i & [F_{14}]+[D_1^-]^r \\ [F_{21}] & [F_{24}] \\ [F_{31}] & [F_{34}] \\ [F_{41}]-[D_1^-]^r & [F_{44}]+[D_1^-]^i \\ [F_{51}] & [F_{54}] \\ [F_{61}] & [F_{64}] \end{bmatrix} \begin{Bmatrix} \{a^r\} \\ \{a^i\} \end{Bmatrix}. \qquad (3.100)$$

This system of equations can then be solved to find the real and imaginary parts of $\{b\}$, $\{c\}$ and $\{d\}$ and thus determine the unknown reflected and transmitted modal mixtures.

3.1.7 Sound Power Transmission

The last topic to be discussed, to complete this section on the equation development, is the subject of sound power transmission. The basis of present

engineering methods for noise prediction in HVAC duct systems is to trace the sound power transmitted through the system. In the present work, on bends and duct junctions, many of the results are given in terms of the sound transmission loss of a duct component.

The presence of flow considerably complicates the equations for sound intensity. In the present work the generalized definition of acoustic intensity of Morfey [40] has been used. This definition can be used for irrotational isentropic flow in hard walled ducts and was used by Cabelli [10] when looking at the influence of flow on the acoustic characteristics of duct bends. As pointed out by Eversman [30], this definition does not give correct results for ducts with absorptive walls in the presence of flow.

3.1.7.1 Sound Power Transmission in a Straight Duct

For the case of uniform flow along the longitudinal x-axis of a straight duct Morfey's definition reduces to

$$I_x = \langle\langle \mathrm{Re}\,(p^*)\,\mathrm{Re}\,(u_x^*)\rangle\rangle + \frac{M}{\rho c_0}\langle\langle \mathrm{Re}\,(p^*)\,\mathrm{Re}\,(p^*)\rangle\rangle + M^2\langle\langle \mathrm{Re}\,(p^*)\,\mathrm{Re}\,(u_x^*)\rangle\rangle + \rho c_0 M\langle\langle \mathrm{Re}\,(u_x^*)\,\mathrm{Re}\,(u_x^*)\rangle\rangle \quad (3.101)$$

where $\langle\langle\ \rangle\rangle$ indicates the time average over the period of the harmonically varying quantity and Re( ) indicates the real part of the quantity. In the absence of flow, the last three terms of this equation are zero and the equation reduces to the standard definition of acoustic intensity—the time average of the product of the real acoustic pressure and acoustic particle velocity. The complex acoustic pressure $p*$ and acoustic particle velocity u_x^* can be written as

$$p^* = P^* e^{i\omega^* t^*} \quad \text{and} \quad u_x^* = U_x^* e^{i\omega^* t^*}. \quad (3.102)$$

For the case of uniform flow, the acoustic pressure can be related to the non-dimensional velocity potential using Equation 3.9 to give

$$P^* = -\rho M c_0^2 \left(\mathrm{i}\omega\phi' + M\frac{\partial \phi'}{\partial x} \right). \tag{3.103}$$

The mode shape functions are orthogonal so that the sound intensity can be calculated for each mode and added to give the total intensity at a given frequency. Substitution of Equation 3.103 and $U_x^* = Mc_0\partial\phi'/\partial x$ and the solutions for forward and backward propagating waves from Equation 3.57, after considerable algebraic manipulation, gives the relatively simple relations

$$I_m^+ = \frac{1}{2}\rho c_0 (Mc_0)^2 \alpha_m \omega^2 \Phi_m^2 |A_{1m}|^2 \quad \text{and} \quad I_m^- = -\frac{1}{2}\rho c_0 (Mc_0)^2 \alpha_m \omega^2 \Phi_m^2 |A_{2m}|^2 \tag{3.104}$$

respectively for the intensities of the forward wave (positive x direction) and backward wave for the m^{th} mode when α_m is real. For the evanescent modes (α^m imaginary) the intensities can be shown to be zero. In deriving Equation 3.104 use was made of the relation

$$\langle\langle \mathrm{Re}(a)\,\mathrm{Re}(b) \rangle\rangle = \frac{1}{2}\left(A^r B^r + A^i B^i \right) \tag{3.105}$$

for the time average of the product of two harmonically varying quantities where $a = Ae^{\mathrm{i}\omega t}$ and $b = Be^{\mathrm{i}\omega t}$.

The transmitted sound power W_m^+ for the forward wave, can then be obtained by integrating the sound intensity I_m^+ over the cross-sectional area of the duct to give

$$\begin{aligned} W_m^+ &= \iint_A I_m^+ \, dA \\ &= \frac{1}{2}\rho c_0 (Mc_0)^2 \alpha_m \omega^2 |A_{1m}|^2 \iint_A \Phi_m^2 \, dA \\ &= \frac{1}{2}\rho c_0 (Mc_0)^2 \alpha_m \omega^2 |A_{1m}|^2 F_m A \end{aligned} \tag{3.106}$$

where F_m can be called the modal power factor and is defined by

$$F_m = \frac{\iint_A \Phi_m^2 \, dA}{\iint_A dA} \tag{3.107}$$

and A is the cross-sectional area of the duct. A similar expression can be derived for the backward wave.

3.1.7.2 Junction and Bend Sound Power Transmission and Reflection

The equations for transmitted sound power, developed in the previous section, can be applied to the straight ducts connected to the FEM model of a duct junction considered in Section 3.1.6.4. Equation 3.106 was based on quantities non-dimensionalized with the straight duct Mach number and characteristic dimension. This can be applied to the straight duct at Station 1, in which the incident modal mixture was specified and the reflected modal mixture determined, to give the total incident and reflected sound powers based on the FEM model quantities as

$$\begin{aligned} W^{\text{inc}_1} &= \frac{1}{2}\rho c_0 (Mc_0)^2 \omega^2 A_1 \sum_{m=0}^{n_1} (\alpha_m)_1 (F_m)_1 \left[(a_m^r)^2 + (a_m^i)^2\right] \\ W^{\text{refl}_1} &= \frac{1}{2}\rho c_0 (Mc_0)^2 \omega^2 A_1 \sum_{m=0}^{n_1} (\alpha_m)_1 (F_m)_1 \left[(b_m^r)^2 + (b_m^i)^2\right] \end{aligned} \tag{3.108}$$

where the subscript 1 refers to quantities evaluated at Station 1 and A_1 is the cross-sectional area of the connecting duct. Also a_m^r, a_m^i, b_m^r and b_m^i are the real and imaginary parts of the m^{th} elements of the modal mixture vectors $\{a\}$ and $\{b\}$ used in Section 3.1.6.3. Similarly the transmitted sound powers in the straight ducts connected at Station 2 and Station 3 are

$$\begin{aligned} W^{\text{trans}_2} &= \frac{1}{2}\rho c_0 (Mc_0)^2 \omega^2 A_2 \sum_{m=0}^{n_2} (\alpha_m)_2 (F_m)_2 \left[(c_m^r)^2 + (c_m^i)^2\right] \\ W^{\text{trans}_3} &= \frac{1}{2}\rho c_0 (Mc_0)^2 \omega^2 A_3 \sum_{m=0}^{n_3} (\alpha_m)_3 (F_m)_3 \left[(d_m^r)^2 + (d_m^i)^2\right] \end{aligned} \tag{3.109}$$

Based on the above, sound power reflection and transmission coefficients for individual modes can be written as

$$\begin{aligned} R_m^1 &= \frac{W_m^{\text{refl}_1}}{W^{\text{inc}_1}} = \frac{1}{W^{\text{inc}_1}}(\alpha_m)_1(F_m)_1\left[(b_m^r)^2+(b_m^i)^2\right] \\ T_m^2 &= \frac{W_m^{\text{trans}_2}}{W^{\text{inc}_1}} = \frac{A_2}{A_1 W^{\text{inc}_1}}(\alpha_m)_2(F_m)_2\left[(c_m^r)^2+(c_m^i)^2\right] \\ T_m^3 &= \frac{W_m^{\text{trans}_3}}{W^{\text{inc}_1}} = \frac{A_3}{A_1 W^{\text{inc}_1}}(\alpha_m)_3(F_m)_3\left[(d_m^r)^2+(d_m^i)^2\right] \end{aligned} \tag{3.110}$$

The modal power factors F_m for each connecting duct were calculated based on the FEM model cross-section modal functions. The finite element approximation to the mode shape function Φ_m is

$$\Phi_m = \langle N\rangle\{q_m\} = \langle q_m\rangle\{N\} \tag{3.111}$$

which substituted into Equation 3.107 gives

$$\begin{aligned} F_m &= \frac{\langle q_m\rangle \iint_A \{N\}\langle N\rangle\, dy\, dz\{q_m\}}{\iint_A dy\, dz} \\ &= \langle q_m\rangle[P]\{q_m\}/A \end{aligned} \tag{3.112}$$

where $[P]$ is the acoustic "mass" matrix for the duct cross-section eigenvalue problem obtained by assembling the element matrices $[P_e]$ and A is the cross-section area obtained by adding the element areas A_e. The integrations in the element domain using the two-dimensional ISOHERM12 element are given by

$$\begin{aligned} [P_e] &= [J_g]^T \int_{-1}^{1}\int_{-1}^{1} \{F\}\langle F\rangle\, |J|\, d\xi\, d\gamma\, [J_g] \\ A_e &= \int_{-1}^{1}\int_{-1}^{1} |J|\, d\xi\, d\gamma \end{aligned} \tag{3.113}$$

In dealing with components with a single input and output the concept of transmission loss is commonly used. In this work, this concept will be extended to junctions with more than one output and will also include the reflected modes in

the duct with the specified incident modal mixture as an output. The transmission losses for the m^{th} reflected mode and the m^{th} transmitted modes in the output ducts have been defined as

$$TL_m^1 = -10\log_{10}R_m^1, \quad TL_m^2 = -10\log_{10}T_m^2 \quad \text{and} \quad TL_m^3 = -10\log_{10}T_m^3 \quad (3.114)$$

In most cases the incident modal mixture is restricted to a single mode and the transmission losses for all the individual output modes calculated. Also the combined output sound powers of all modes given by Equation 3.109 can be used to calculate an overall transmission loss for each duct outlet.

3.2 Tests of the FEM for Plane Waves in Straight Ducts

This section discusses tests of the finite element model to predict plane wave propagation in straight ducts with uniform flow using the FEM formulation developed in Section 3.1.5.

3.2.1 Propagation with the Inlet Acoustic Velocity Specified

The first problem to be considered, was a straight duct of length a modeled using ISOHERM12 quadrilateral elements. A duct width of a was used, however the model was constrained to a one dimensional problem, so that any width could be arbitrarily chosen. Models with one, two and four elements in a linear string were used. The same element mesh was used for both the flow and the acoustic problems and is shown as an example for the two element model in Figure 3.3. The group of the three global degrees of freedom at each corner of the elements corresponds to the velocity potential ϕ (acoustic or flow) and the partial derivatives $\partial\phi/\partial x$ and $\partial\phi/\partial y$ respectively. With reference to the velocity potential nodes of Figure 3.3, the constraint equations "[3]" = "[6]" = "[9]" = 0.0 were used to constrain the $\partial\bar{\phi}/\partial y$ and $\partial\phi'/\partial y$ to zero at nodes along the top and bottom edges of

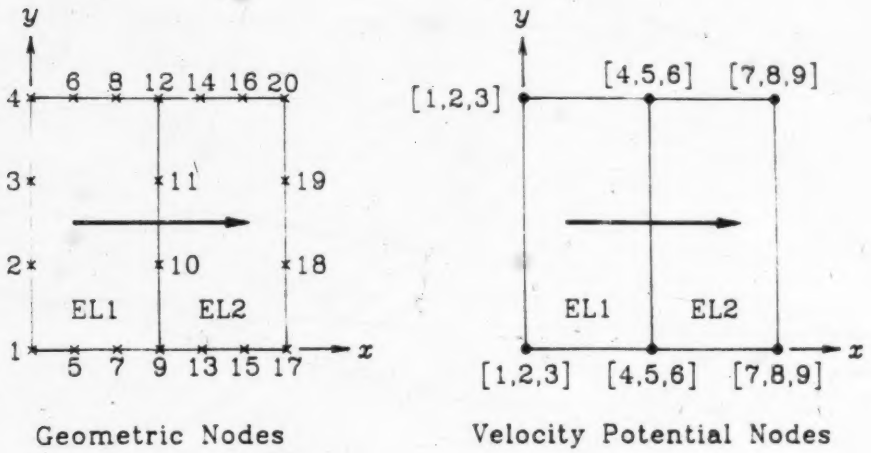

Figure 3.3 Two-Element Model for Plane Wave Propagation in a Straight Duct

the duct. For the flow problem an additional constraint equation "[1]" = 1.0 was used to assign a value of one to $\bar{\phi}$ at this node. Note that the same global degree of freedom has been assigned to nodes on the top and bottom of the duct with the same x coordinate, reducing the model to one-dimensional flow and plane wave propagation. Flow boundary conditions giving an inlet Mach ratio $M_{\text{inlet}}/M = -1$ and outlet Mach ratio $M_{\text{outlet}}/M = 1$ were used. An acoustic velocity of $U = 1$ was specified at the inlet (refer to Section 3.1.5.1) and anechoic termination at the outlet (refer to Section 3.1.5.2).

The flow problem was solved first (in this case giving the same result as the analytical solution) and the global vector $\{\bar{\phi}_g\}$ of flow velocity potential and derivative quantities then used in the solution of the flow-acoustic problem as described in Section 3.1.5.4.

The analytical solution of this problem can be obtained by using the above boundary conditions in the general solution (Equation 3.30) of the governing differential equation (Equation 3.29), which was derived from the convected wave

equation, and is given by

$$\phi'_{\text{conv.}} = \frac{M+1}{\omega} e^{-i\omega x/(1+M)} \tag{3.115}$$

The resulting FEM model acoustical velocity potential ϕ'_{FEM} at the outlet ($x = 1$) is compared to the above analytical solution in Table 3.1 for the one, two and four-element models, for a range of values of the non-dimensional frequency parameter ω (which equals ka) and Mach numbers of zero, 0.1 and -0.1. The magnitude and phase refer to the complex quantity given by the ratio of the FEM acoustic velocity potential and the convected wave equation velocity potential. The magnitude ratio (in decibels) was calculated on a logarithmic scale and is given by $10\log_{10}\left(|\phi'_{\text{FEM}}|/|\phi'_{\text{conv}}|\right)$.

For the case of no flow the errors generally increased with increasing ka and decreased as the number of elements in the model was increased. The one element model gave magnitude errors of less than 0.1 dB and phase errors of less than one degree up to a value of ka between 3 and 4. Two elements gave similar errors up to a value of ka between 6 and 8 and three elements gave magnitude errors of less than 0.1 dB at $ka = 12$. This would indicate that each element can model reasonably accurately one-half of a wavelength.

For the case of flow, Table 3.1 shows that the FEM models converged to nonzero error values and that the phase errors were generally higher at higher frequencies. It was suspected that this was due to the small Mach number approximation made in deriving the governing differential equation in terms of velocity potential used in the FEM model. The case of negative Mach numbers (the flow in the opposite direction to the acoustic propagation) exhibited higher phase errors than the positive Mach number case.

Table 3.1 Convergence for Plane Wave Propagation in a Straight Duct with Uniform Flow

ka	One element		Two elements		Four elements	
	Magnitude Error dB	Phase Error deg.	Magnitude Error dB	Phase Error deg.	Magnitude Error dB	Phase Error deg.
			$M = 0.0$			
0.5	0.0000	0.00	0.0000	0.00	0.0000	0.00
2	0.0021	0.02	0.0000	0.00	0.0000	0.00
4	-0.1220	1.08	0.0003	0.09	0.0000	0.00
6	-0.7219	29.34	0.0164	0.21	0.0001	0.03
8	0.2405	92.55	-0.2228	5.31	0.0017	0.18
10	3.1838	146.33	-0.0677	14.97	0.0026	0.72
12	1.7390	167.90	-1.9300	46.25	0.0590	0.70
			$M = 0.1$			
0.5	0.0050	0.24	0.0050	0.24	0.0050	0.24
2	0.0202	0.36	0.0177	0.36	0.0177	0.36
4	-0.1334	0.64	0.0132	1.12	0.0128	1.08
6	-0.8211	23.30	0.0198	0.90	0.0015	1.35
8	0.2280	79.23	-0.2491	4.69	0.0231	1.92
10	4.8110	128.58	-0.0562	8.56	0.0112	2.90
12	2.2140	98.55	-2.0196	27.70	0.0736	2.12
			$M = -0.1$			
0.5	0.0050	0.30	0.0050	0.30	0.0050	0.30
2	0.0194	0.65	0.0177	0.59	0.0177	0.59
4	-0.0865	5.29	0.0131	1.71	0.0128	1.55
6	-0.5807	42.68	0.0137	3.27	0.0014	2.09
8	0.1506	117.69	-0.1633	13.28	0.0223	3.10
10	1.9865	189.12	-0.0374	36.33	0.0098	4.98
12	1.2201	246.71	-1.5313	82.60	0.0509	6.75

The general solution to the small Mach number, potential flow equation for plane wave propagation with uniform flow was given by Equation 3.31 which for a wave propagating in the positive x-direction and $\partial\phi'/\partial x = 1$ at $x = 0$ reduces to

$$\phi'_{\text{vel.pot.}} = \frac{e^{-i\omega\left(\sqrt{M^2+1}-M\right)x}}{\omega\left(\sqrt{M^2+1}-M\right)} \tag{3.116}$$

With no flow, this solution is identical to the solution given in Equation 3.115. The magnitude and phase of this solution at $x = 1$ is compared to the convected wave equation solution of Equation 3.115 for Mach numbers of ± 0.1 in the first columns

of Table 3.2. The magnitude errors are shown to be independent of frequency and slightly higher for the negative Mach number case but less than one-fortieth of a decibel. The phase error is a linear function of frequency, again higher for the negative Mach number case, and reaching approximately two degrees at $ka = 6$. This is one aspect of the selected approximate flow model that was not initially appreciated. Even though the Mach number may be small, the resulting phase error can be significant if a large value of ka is used.

The FEM results given in Table 3.1 still do not converge exactly to the analytical small Mach number velocity potential solution given in Table 3.2. The finite element model was based on the same governing differential equation, however, there was a difference in boundary conditions used. The FEM model used the convected wave boundary condition to obtain the anechoic termination element matrix given by Equation 3.41 and Equation 3.42. The anechoic boundary condition could also be obtained by using the small Mach number potential flow solution of Equation 3.31. This leads to equations for the element matrix $[A_e]$ identical to Equation 3.41 and Equation 3.42 with the exception that the term $1/(1 + M_j)$ is replaced by $\sqrt{M_j^2 + 1} - M_j$. These terms differ by approximately half of one percent for M less than 0.1. The last four columns of Table 3.2 compare the FEM models with four elements using the small Mach number velocity potential anechoic termination to the analytical convected wave equation and small Mach number velocity potential solutions. For these cases the FEM model now converges to the analytical solutions. The results also show more clearly the effect of the flow on the accuracy of the phase error in the finite element solutions. The phase error increases with frequency and is larger for the negative Mach numbers. This is reasonable since the negative flow effectively decreases the speed of wave propagation, thus

Table 3.2 Comparison of Models for Plane Wave Propagation in a Straight Duct with Uniform Flow

	Exact vel.pot. compared to Exact conv.wave		FEM(vel.pot.b.c.) compared to Exact conv.wave		FEM(vel.pot.b.c.) compared to Exact vel.pot.	
ka	Magnitude Error dB	Phase Error deg.	Magnitude Error dB	Phase Error deg.	Magnitude Error dB	Phase Error deg.
			$M = 0.1$			
0.5	0.0196	0.12	0.0196	0.12	0.0000	0.00
2	0.0196	0.47	0.0196	0.47	0.0000	0.00
4	0.0196	0.94	0.0197	0.94	0.0000	0.00
6	0.0196	1.41	0.0198	1.42	0.0001	0.01
8	0.0196	1.88	0.0218	1.97	0.0022	0.09
10	0.0196	2.35	0.0237	2.77	0.0041	0.42
12	0.0196	2.82	0.0878	2.24	0.0682	-0.58
			$M = -0.1$			
0.5	0.0240	0.18	0.0240	0.18	0.0000	0.00
2	0.0240	0.70	0.0240	0.70	0.0000	0.00
4	0.0240	1.40	0.0240	1.40	0.0000	0.00
6	0.0240	2.11	0.0241	2.16	0.0001	0.06
8	0.0240	2.81	0.0255	3.15	0.0014	0.35
10	0.0240	3.51	0.0268	4.85	0.0028	1.33
12	0.0240	4.21	0.0695	6.88	0.0455	2.67

decreasing the wavelength so that each element is relatively longer compared to the wavelength.

At this stage one might suggest that it would be better to use the small Mach number velocity potential solution boundary condition. This can be easily done for plane wave propagation. For higher order mode propagation the solutions become more complicated and it was thought best to use the well known convected wave equation solutions for connecting ducts rather than deriving solutions to the approximate low Mach number potential flow equations. Also comparison of the FEM solutions with the two different boundary condition models in Table 3.1 and Table 3.2 shows that the difference between the two FEM models is small.

One consequence of choosing to use the convected wave equation in the

connecting ducts and the small Mach number velocity potential governing differential equation in the FEM domain is that the termination will not be truly anechoic. There will be a small reflection at the termination since the acoustic impedances at the connecting boundary will not match exactly if there is flow in the duct. This will be investigated in the following section.

3.2.2 Propagation with a Specified Incident Velocity Potential

The same straight duct with uniform flow modeled in Section 3.2.1 has been considered here. However, instead of a specified inlet acoustic velocity, the incident wave velocity potential has been specified at the inlet and implemented with the FEM using ISOHERM12 elements as discussed in Section 3.1.5.3. For convenience, a unit value was assigned to the incident acoustic velocity potential at the inlet ($B_{\text{inc}} = 1$ in Section 3.1.5.3). After solving for the FEM model nodal velocity potentials, the reflected velocity potential at the inlet, ϕ'_{refl} can be obtained by solving Equation 3.45 to give $\phi'_{\text{refl}} = \phi'_{\text{inlet}} - 1$ where ϕ'_{inlet} is the total velocity potential at the inlet obtained from the FEM model solution. Also the velocity potential for the transmitted wave at the outlet can be taken as ϕ'_{outlet}, the velocity potential at the outlet from the FEM solution. Applying the sound power definitions discussed in Section 3.1.7 to the plane wave mode leads to the following equations for the FEM model sound power reflection coefficient R and transmission coefficient T

$$R = |\phi'_{\text{inlet}} - 1|^2 \quad \text{and} \quad T = |\phi'_{\text{outlet}}|^2 \tag{3.117}$$

If the reflected wave is treated as a transmission path then the transmission loss TL of the FEM model and for lack of a better word, the reflection loss RL are then

$$TL = -10\log_{10}T \quad \text{and} \quad RL = -10\log_{10}R \tag{3.118}$$

In theory the total reflected and transmitted sound power should equal the incident sound power since there is no other dissipation within the rigid walled model. To compare the total reflected plus transmitted sound power to the incident sound power of the FEM model, a quantity called the total sound power loss PL will be defined, based on the ratio of the transmitted plus reflected sound power to the incident sound power and is given by

$$PL = -10\log_{10}(R+T) \tag{3.119}$$

Table 3.3 shows the reflection loss RL and the transmission TL for the straight duct of length a modeled with a string of one, two and four ISOHERM12 quadrilateral elements. Ideally the incident wave should propagate unattenuated with no reflected wave created so that $TL = 0$ and $RL = \infty$. The one element model gave errors in the transmission loss TL of less than 0.1 dB up to a value of ka between 4 and 6. Two elements give similar errors for a value of ka between 10 and 12. These are higher values of ka than observed for similar magnitude errors from Table 3.1 for the specified acoustic velocity problem of Section 3.2.1.

For the case of no flow, as the number of elements is increased, the TL does appear to converge to zero and the reflected wave becomes negligible. With flow, the models converge to a residual error value, presumably due to the small Mach number approximation in the governing differential equation in conjunction with using the convected wave equation boundary condition. For $M = \pm 0.1$ the residual error in TL was less than 10^{-4} decibels. The RL values converge to values of the order of 45 decibels or less for $M = \pm 0.1$ which means that the reflected wave sound power is less than 0.003 percent of the incident sound power. It was observed that the positive and negative Mach number cases give identical errors in TL but different errors in RL.

Table 3.3 Convergence for Plane Wave Propagation in a Straight Duct with the Incident Wave Specified

ka	One element		Two elements		Four elements	
	RL in dB	TL in dB	RL in dB	TL in dB	RL in dB	TL in dB
			$M = 0.0$			
0.5	148.3	0.000000	179.6	0.000000	212.7	0.000000
2	65.5	0.000001	99.0	0.000000	132.6	0.000000
4	28.5	0.006184	79.9	0.000000	127.0	0.000000
6	12.9	0.231286	37.5	0.000772	81.2	0.000000
8	6.4	1.136354	25.8	0.011462	67.9	0.000000
10	3.6	2.456823	25.9	0.011070	58.9	0.000006
12	2.3	3.797621	7.4	0.861033	32.0	0.002717
			$M = 0.1$			
0.5	54.2	0.000025	54.2	0.000025	54.2	0.000025
2	47.5	0.000110	48.6	0.000089	48.7	0.000088
4	29.4	0.004733	49.8	0.000068	50.1	0.000064
6	13.2	0.210475	36.7	0.000954	59.1	0.000008
8	6.5	1.096154	26.4	0.009410	47.1	0.000122
10	3.7	2.416534	28.4	0.006151	48.7	0.000078
12	2.4	3.759139	8.2	0.709997	31.2	0.003461
			$M = -0.1$			
0.5	50.7	0.000025	50.7	0.000025	50.7	0.000025
2	44.4	0.000110	45.2	0.000089	45.2	0.000088
4	29.8	0.004733	46.3	0.000068	46.6	0.000064
6	13.2	0.210475	36.4	0.000954	55.8	0.000008
8	6.5	1.096154	26.8	0.009410	43.9	0.000122
10	3.7	2.416534	28.5	0.006151	46.3	0.000078
12	2.4	3.759139	8.2	0.709997	30.8	0.003461

One measure of the accuracy of the model predictions, used for example by Cabelli [10], is the comparison of the transmitted plus reflected sound power to the incident sound power. The total sound power loss PL defined by Equation 3.119 for the current problem is given in Table 3.4 for the one, two and four-element models of the straight duct. Without flow, the PL values were less than 10^{-14} dB for all FEM models at all frequencies and thus the transmitted plus reflected sound power was exactly equal to the incident sound power (within computer round-off error). Certainly in this case the sound power check does not give a measure of the

Table 3.4 Total Sound Power Check for Plane Wave Propagation in a Straight Duct with the Incident Wave Specified

ka	Total sound power loss PL in dB		
	One element	Two elements	Four elements
		$M = 0.0$	
0.5	1.4465×10^{-15}	9.6432×10^{-16}	3.8573×10^{-15}
2	4.8216×10^{-16}	3.8573×10^{-15}	1.4465×10^{-15}
4	1.4465×10^{-16}	9.6432×10^{-16}	2.8929×10^{-15}
6	-2.8929×10^{-15}	9.6432×10^{-16}	-9.6432×10^{-16}
8	4.3395×10^{-15}	9.6432×10^{-16}	4.8216×10^{-16}
10	-3.8573×10^{-15}	-4.8216×10^{-15}	4.3395×10^{-15}
12	-3.8573×10^{-15}	-9.6432×10^{-15}	4.8216×10^{-16}
		$M = 0.1$	
0.5	8.2429×10^{-6}	8.2427×10^{-6}	8.2427×10^{-6}
2	3.3313×10^{-5}	2.9199×10^{-5}	2.9113×10^{-5}
4	-2.0537×10^{-4}	2.1826×10^{-5}	2.1055×10^{-5}
6	-7.2394×10^{-4}	3.5992×10^{-5}	2.4278×10^{-6}
8	4.1821×10^{-3}	-3.9213×10^{-4}	3.7950×10^{-5}
10	9.2923×10^{-3}	-6.8138×10^{-5}	1.8513×10^{-5}
12	1.1109×10^{-2}	-1.9794×10^{-3}	1.3194×10^{-4}
		$M = -0.1$	
0.5	-1.2313×10^{-5}	-1.2313×10^{-5}	-1.2313×10^{-5}
2	-4.7715×10^{-5}	-4.3576×10^{-5}	-4.3489×10^{-5}
4	1.9684×10^{-4}	-3.2194×10^{-5}	-3.1450×10^{-5}
6	7.2151×10^{-4}	-3.7403×10^{-5}	-3.5361×10^{-6}
8	-4.1962×10^{-3}	3.7646×10^{-4}	-5.4937×10^{-5}
10	-9.3191×10^{-3}	6.7392×10^{-5}	-2.4314×10^{-5}
12	-1.1129×10^{-2}	1.9743×10^{-3}	-1.3717×10^{-4}

accuracy of TL values which were in error by several decibels for the one element model at the largest ka values. With flow, the finite element models converged to small but nonzero values of PL in the order of 10^{-5} decibels, and the PL values were much smaller in many cases than the individual errors in the transmitted and reflected sound powers. Comparison of the PL values for $M = \pm 0.1$ shows that the values for a positive Mach number were roughly equal to those for the negative Mach number but of opposite sign. For the four-element model with positive

Mach number, the reflected plus transmitted sound power was slightly less than the incident sound power and for a negative Mach number slightly greater than the incident sound power.

3.3 Tests of the FEM Model Including Higher Order Modes

This section discusses tests of the finite element model to predict wave propagation in a straight duct with uniform flow and in a duct bend, including higher order modes using the FEM formulation developed in Section 3.1.6.

3.3.1 Mode Shapes and Eigenfrequencies for Rectangular Ducts

Part of the FEM developed for modeling higher order mode boundary conditions requires finding the mode shapes and eigenfrequencies of the duct cross-sections for the straight ducts linked to the bend or junction FEM models. The FEM model for the solution of this eigenvalue problem was considered in detail in Section 2.3. As the subsequent work will consider rectangular ducts, this section looks at rectangular duct cross-sections.

The exact mode shape function for the rectangular hard walled duct cross-section is

$$\Phi_m(y,z) = \cos(n_y \pi y) \cos\left(\frac{n_z \pi z}{r_z}\right) \tag{3.120}$$

and the exact non-dimensional frequency parameter given by

$$\omega_{c_m}^2 = \pi^2 \left[n_y^2 + \left(\frac{n_z}{r_z}\right)^2 \right] \tag{3.121}$$

for the m^{th} mode, where n_y and n_z can have any integer value from zero to infinity. Also y and z have been non-dimensionalized based on the duct width in the y-direction and r_z is the ratio of the duct width in the z-direction to that in the y-direction. The modal power factor F_m, defined by Equation 3.107, calculated

from the exact mode shapes given by Equation 3.120 gives a value of $F_m = 1$ for the plane wave mode ($n_y = n_z = 0$), a value of $F_m = 1/2$ for modes with either $n_y = 0$ or $n_z = 0$ and a value of $F_m = 1/4$ for modes with both n_y and n_z nonzero.

Figure 3.4 shows the ISOHERM12 element meshes used to generate the eigenvalues, mode shapes and modal sound power factors. Most of the subsequent work deals with two-dimensional duct problems with one, two or three quadrilateral elements spanning the connecting duct interfaces so that only one-dimensional eigenvalue problems must be solved. The one-element model has been set up to illustrate the two-dimensional cross-section model needed to provide input into a three-dimensional duct model. The width of the duct in the z-direction has been taken as twice the width in the y-direction. The two and three-element models have been constrained to one-dimensional models in the y-direction.

The one-element model in Figure 3.4 assumes rigid walled ducts so that the derivatives $\partial\phi'/\partial y$ and $\partial\phi'/\partial z$ are taken to be zero at the corner nodes. These have been assigned to the last nodal quantity "[5]" of the one-element model in Figure 3.4. This nodal quantity was excluded from the global matrices in the element assembly procedure. The mode shape is thus defined in terms of an eigenvector of the four corner nodal acoustic velocity potentials only. The finite element solution to this ISOHERM12 one-element model gives the following modal matrix $[\Phi]$ (refer to Section 3.1.6.4, Equation 3.72)

$$[\Phi]_{1el} = \begin{bmatrix} 1 & 1 & 1 & 1 \\ 1 & -1 & 1 & -1 \\ 1 & 1 & -1 & -1 \\ 1 & -1 & -1 & 1 \end{bmatrix} \tag{3.122}$$

where each column is the eigenvector for a mode, ordered from the mode with the smallest eigenvalue in first column (the plane wave mode) to the mode corresponding to the largest eigenvalue in the last column. Note that in this case the evaluation

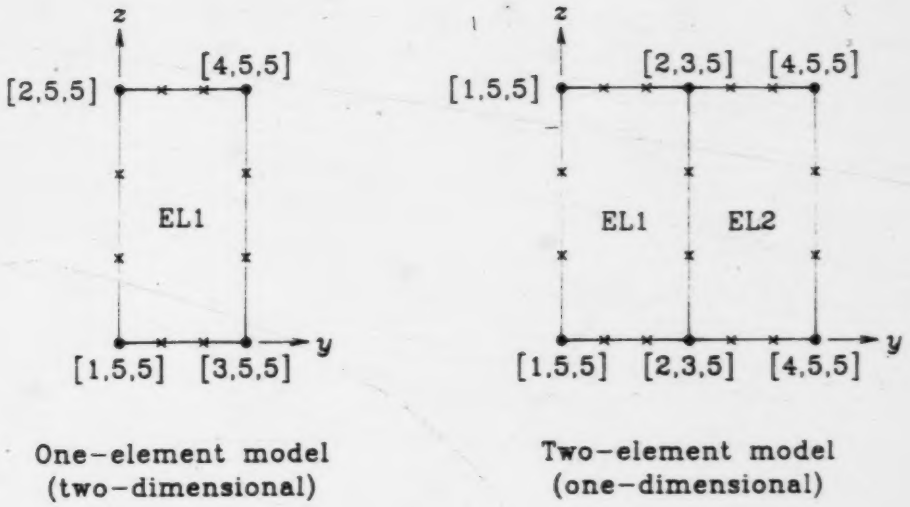

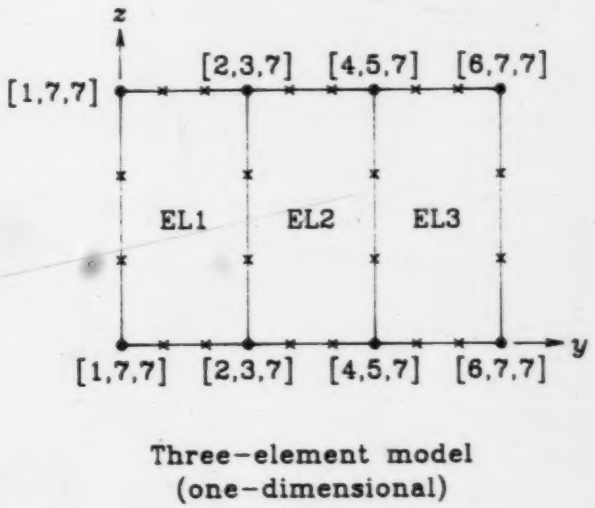

Figure 3.4 Rectangular duct cross-section models

of the exact mode shape functions given by Equation 3.120 at the corners of the duct gives modes identical to those in $[\Phi]$ obtained from the FEM model. If the one-element model is used to solve the one-dimensional eigenvalue problem then the modal matrix is given by

$$[\Phi]_{1el} = \begin{bmatrix} 1 & 1 \\ 1 & -1 \end{bmatrix} \tag{3.123}$$

where the first column corresponds to the plane wave mode and the second to the first cross mode.

The finite element solution to the ISOHERM12 two-element model shown in Figure 3.4 gives the following model matrix

$$[\Phi]_{2el} = \begin{bmatrix} 1 & 1 & 1 & 1 \\ 1 & 0 & -1 & 0 \\ 0 & -3.212 & 0 & 18.212 \\ 1 & -1 & 1 & -1 \end{bmatrix} \tag{3.124}$$

where the first, second and fourth elements of each column are the nodal velocity potentials and the third element of each column is the slope $\partial\phi'/\partial y$ midway across the duct. The nodal quantity "[5]" as for the one element model has been used for all nodal quantities constrained to zero. Note that in this case all elements of $[\Phi]$ are identical to the exact modal function evaluated at the nodes except for the slope quantities in the second and fourth columns. The exact value of $\partial\phi'/\partial y$ evaluated at this point for the first cross mode is $-\pi$ compared to a value of -3.212 in the FEM modal matrix, and for the third cross mode a value of 3π compared to a value of 18.212 in Equation 3.124.

Similarly the modal matrix $[\Phi]$ for three elements across the duct is given by

$$[\Phi]_{3el} = \begin{bmatrix} 1 & 1 & 1 & 1 & 1 & 1 \\ 1 & 0.5 & -0.5 & -1 & -0.5 & 0.5 \\ 0 & -2.736 & -5.739 & 0 & 17.079 & 36.444 \\ 1 & -0.5 & -0.5 & 1 & -0.5 & -0.5 \\ 0 & -2.736 & 5.739 & 0 & -17.079 & 36.444 \\ 1 & -1 & 1 & -1 & 1 & -1 \end{bmatrix} \tag{3.125}$$

where all velocity potential values are identical to the exact modal function evaluated at the nodes. The derivative values 2.736, 5.739, 17.079 and 36.444 in the third and fifth rows of this matrix correspond to the derivatives $d\Phi_m/dy$ of the exact modal function evaluated at one-third and two-third points across the duct. These are given by $\pi\sqrt{3}/2 = 2.720$, $\pi\sqrt{3} = 5.441$, $2\pi\sqrt{3} = 10.882$ and $5\pi\sqrt{3}/2 = 13.60$ for the first, second, fourth and fifth cross modes respectively.

In both the two and three-element models, the exact and FEM nodal derivative values differ significantly, with differences becoming greater as the mode number is increased. It is still best to use the FEM derivative values in the modal matrices rather than the exact values. Substitution of the exact values into the modal vectors leads to increased errors in the modal sound power factors and increased coupling between modes. The eigenvalues and modal sound power factors for the one, two and three element FEM models are compared to the exact values in Table 3.5. In terms of the one dimensional models, the one-element model predicts fairly accurately the first cross mode—the only cross mode that it considers. The two-element model predicts fairly accurately the first and second cross mode values and inaccurately predicts the third cross mode. The three element model gives fairly accurate predictions for the first, second and third cross modes, but less accurate predictions of the fourth and fifth cross modes.

The orthogonality of the modes can be checked by extending Equation 3.112 which defines the modal sound power factors F_m to give the matrix $[\Phi]^T[P][\Phi]/A$. The diagonal elements of this matrix are the modal sound power factors F_m. For the FEM models considered here, all off-diagonal elements had values of 10^{-14} or less which indicates insignificant coupling between the modes.

TABLE 3.5 Eigenvalues and Modal Power Factors for Duct Cross-sections

Mode No. m	Exact				ISOHERM12 FEM			
	n_x	n_y	ω_m^2	F_m	ω_m^2	Percent Error in ω_m^2	F_m	Percent Error in F_m
One-element, two-dimensional cross-section model								
0	0	0	0	1	0.0000	—	1.0000	0.000
1	0	1	$\frac{\pi^2}{4}$	$\frac{1}{2}$	2.4706	0.129	0.4857	-2.857
2	1	0	π^2	$\frac{1}{2}$	9.8824	0.129	0.4857	-2.857
3	1	1	$\frac{5\pi^2}{4}$	$\frac{1}{4}$	12.3529	0.129	0.2359	-5.632
Two-element, one-dimensional cross-section model								
0	0	0	0	1	0.0000	—	1.0000	0.000
1	1	0	π^2	$\frac{1}{2}$	9.8722	0.026	0.4954	-0.916
2	2	0	$4\pi^2$	$\frac{1}{2}$	39.5294	0.129	0.4857	-2.857
3	3	0	$9\pi^2$	$\frac{1}{2}$	94.2509	6.107	0.5974	19.49
Three-element, one-dimensional cross-section model								
0	0	0	0	1	0.0000	—	1.0000	0.000
1	1	0	π^2	$\frac{1}{2}$	9.8699	0.003	0.4988	-0.244
2	2	0	$4\pi^2$	$\frac{1}{2}$	39.5204	0.106	0.4895	-2.110
3	3	0	$9\pi^2$	$\frac{1}{2}$	88.9412	0.129	0.4857	-2.857
4	4	0	$16\pi^2$	$\frac{1}{2}$	162.858	3.131	0.5206	4.120
5	5	0	$25\pi^2$	$\frac{1}{2}$	273.558	10.87	0.8549	70.98

3.3.2 Propagation in a Straight Duct with Uniform Flow

The propagation within a rigid walled, two-dimensional, straight duct of width a has been considered in this section. A segment of the duct of length a has been modeled with one, two and three square ISOHERM12 elements across the duct width as shown in Figure 3.5. It was assumed that the straight duct extends to the left and right of the FEM model. The left side of the model has been taken

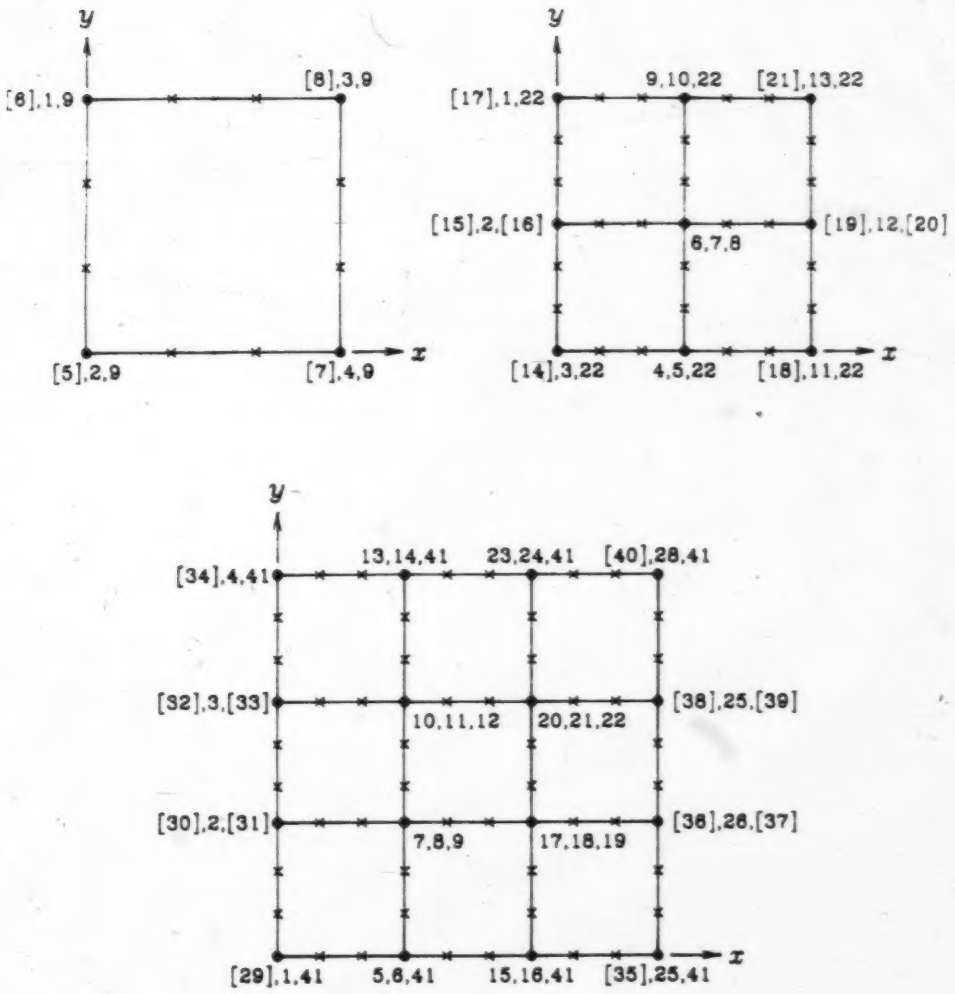

Figure 3.5 Finite Element Meshes for a Straight Duct

as the inlet at which an incident modal mixture is specified and an anechoic termination assumed at the outlet on the right side of the model. A uniform flow has been assumed for which a positive Mach number indicates flow from the left to the right.

The numbering of the global degrees of freedom in the models is shown in Figure 3.5. The highest numbered degree of freedom has been assigned to the $\partial\phi'/\partial y$ nodal quantities at the hard walls and has been constrained to a zero value. The numbers in square brackets indicate the quantities defining the inlet and outlet cross-section modal vectors. For the one-element model these involve only acoustic velocity potential quantities. For the other models these include $\partial\phi'/\partial y$ terms as well.

Either a plane wave, or the first, second or third cross modes have been chosen for the incident modal mixture vector $\{a\}$ defined in Section 3.1.6.4. A real unit value was assigned to the element of $\{a\}$ corresponding to the selected mode and zeros assigned to all other elements. The outlet modal mixture vector $\{c\}$ was then calculated from the exact convected wave equation solution and the FEM model over a range of ka values. The elements of $\{a\}$ and $\{c\}$ correspond respectively to the incident acoustic velocity potential at the inlet and the transmitted acoustic velocity potential at the outlet, taken at the lower wall of the duct for each mode.

The resulting plane wave acoustic velocity potential at the outlet with a unit incident plane wave velocity potential is shown in Figure 3.6 for the case of no flow. The real and imaginary parts of the outlet velocity potential for the FEM models with one, two and three elements across the duct are compared to the exact solution as a function of ka. The exact solution has been plotted at intervals in ka of 0.125 and the FEM values at twice this interval. All three models show good agreement with the exact solution up to ka of 3.5 at which point the one-element

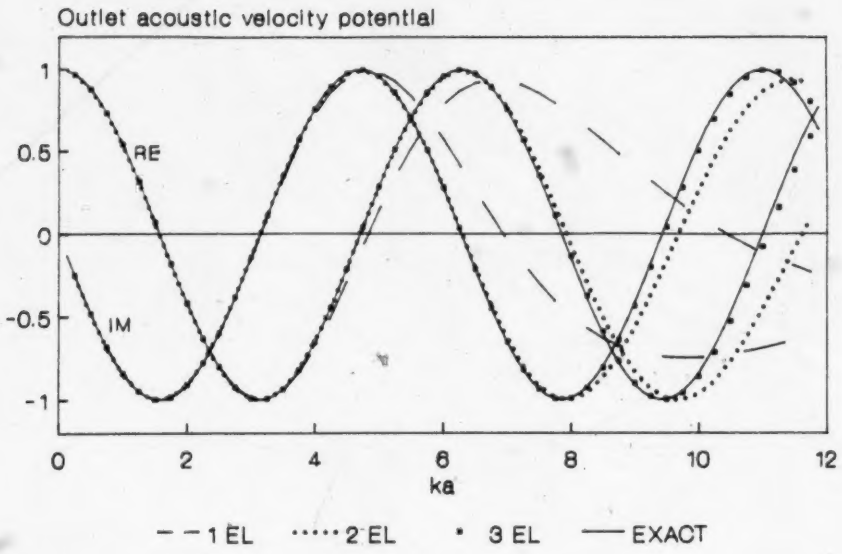

Figure 3.6 Plane Wave Acoustic Velocity Potential for a Straight Duct with no Flow

prediction starts to deviate visibly from the exact curves. With two elements across the duct width, the FEM prediction visibly starts to deviate from the exact curve at a ka value of about 7 and with three elements at a ka value of 10.

A similar graph for the first cross mode is shown in Figure 3.7. Below the cut-on frequency for this mode, the imaginary part of ϕ' is zero and the real part of ϕ' at the outlet is less than the unit incident value at the input. This demonstrates the decay of this evanescent mode from inlet to outlet and shows how the amount of decay is reduced as the frequency parameter ka increases and approaches the cut-on value of $ka = \pi$. The deviation between the exact and FEM model curves near the cut-on frequency is caused by differences in intervals at which the exact and FEM model points are plotted. The convergence of the FEM models to the exact solution appears to be similar to that for the plane wave.

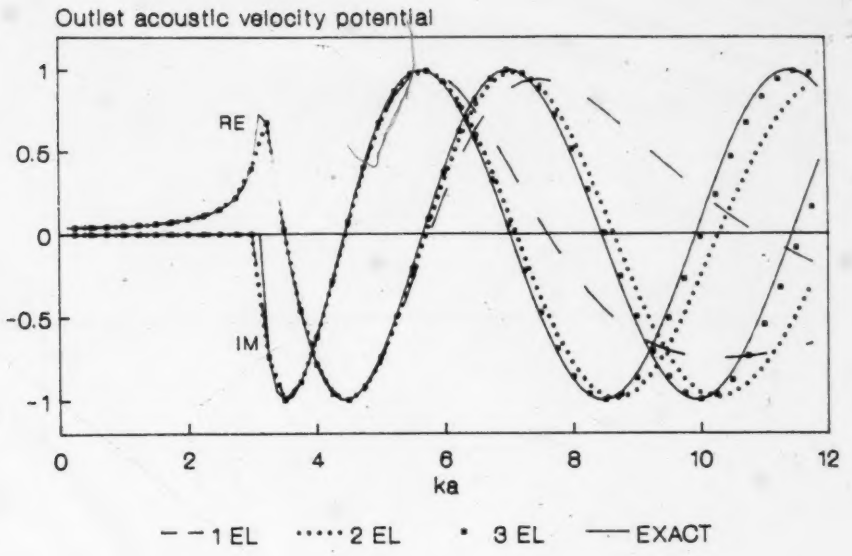

Figure 3.7 First Cross Mode Acoustic Velocity Potential for a Straight Duct with No Flow

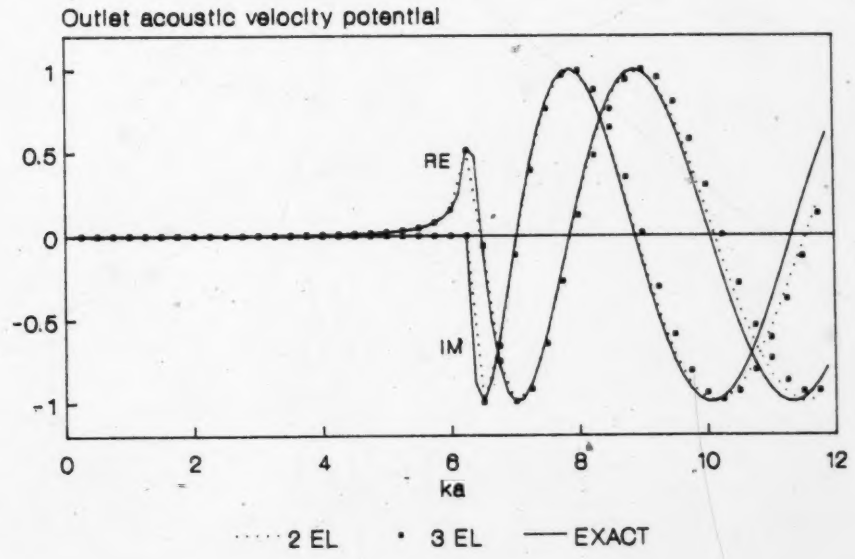

Figure 3.8 Second Cross Mode Acoustic Velocity Potential for a Straight Duct with No Flow

The graph of the second cross mode velocity potential at the outlet, for a unit inlet second cross mode potential, is shown in Figure 3.8. Note that the one-element model only predicts the plane wave and first cross mode and thus is not shown on this graph. The FEM model with two elements across the duct width starts to visibly deviate from the exact curve at a ka value of about 8. Note that the FEM model with three elements across the duct width gives greater errors than with two elements. This unexpected result may be partially explained by the observation that each element in the two-element model models exactly one half of a wavelength of the cross-section mode shape. It was noted in the last paragraph of Section 2.3.2.2, that the eigenvalues of a one-dimensional tube were predicted more accurately when each element modeled exactly half a wavelength. Table 3.5 shows, however, that the three-element model gives marginally smaller errors than the two-element model when predicting the eigenvalue ω_2 and modal power factor F_2 for the second cross mode. Thus, one would have expected the model with three elements across the duct width to give at least as good a prediction as with two elements across the width.

The results for the third cross mode are shown in Figure 3.9 for the case of no flow. The noticeable "clipping" of the exact solution, in this and other figures, is caused by the coarseness of the intervals at which the solution was evaluated. The FEM model with two elements across the duct width deviates considerably from the exact solution above the cut-on frequency of $ka = 3\pi$ for this mode. The model with three elements across the duct width on the other hand gives a very accurate prediction up to ka approaching 12—in fact more accurate than the predictions of the plane wave and lower cross modes with this model. For this mode each element models exactly one half of a wavelength of the cross-section mode shape.

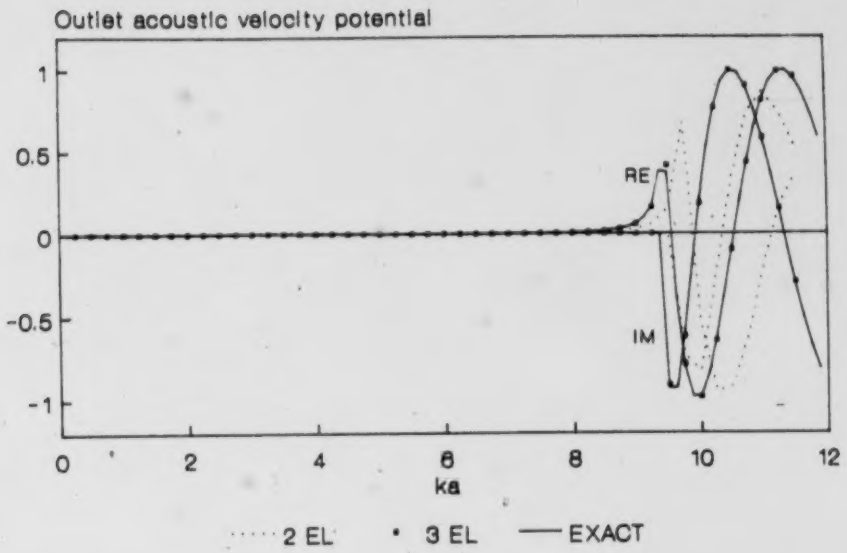

Figure 3.9 Third Cross Mode Acoustic Velocity Potential for a Straight Duct with No Flow

The results with flow are given in Figure 3.10, Figure 3.11, Figure 3.12 and Figure 3.13 for Mach numbers of 0.1 and -0.1 where a positive Mach number indicates the flow is in the same direction as the acoustic wave propagation and a negative Mach number indicate that the flow in the opposite direction. The results for the plane wave are shown in Figure 3.10 and are similar to the curves obtained for the no-flow case. For the positive Mach number case, the sinusoidal shaped curves have been "stretched out" and for the negative Mach number case "compressed" along the ka axis in comparison to the no-flow case. Also it was observed that flow in the opposite direction of the acoustic propagation increased the prediction error at a given ka value. Similar observations can be made concerning the first cross-mode results given in Figure 3.11. One difference noted here, compared to the no-flow case, is that below the cut-on frequency, the imaginary part of the velocity potential is nonzero and positive for the positive Mach number case and negative

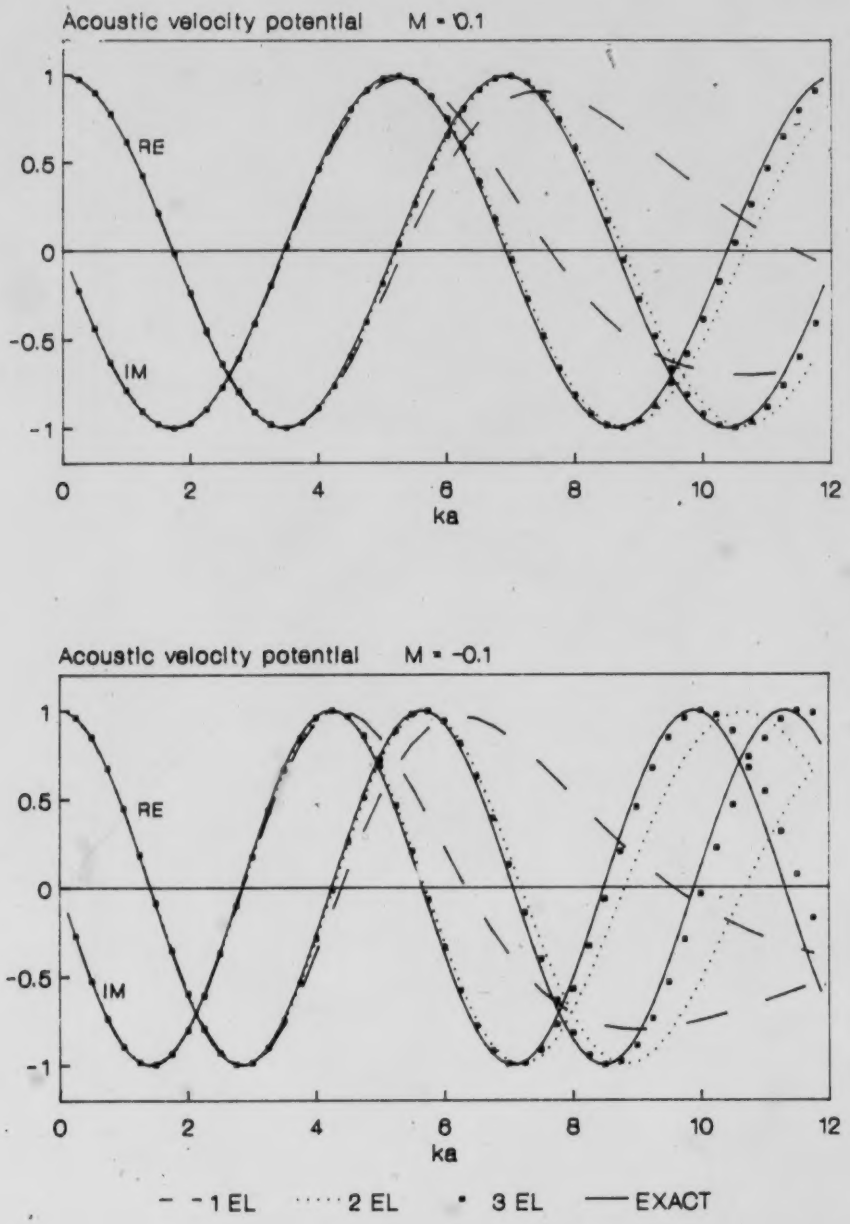

Figure 3.10 Outlet Plane Wave Acoustic Velocity Potential for a Straight Duct with a Uniform Flow

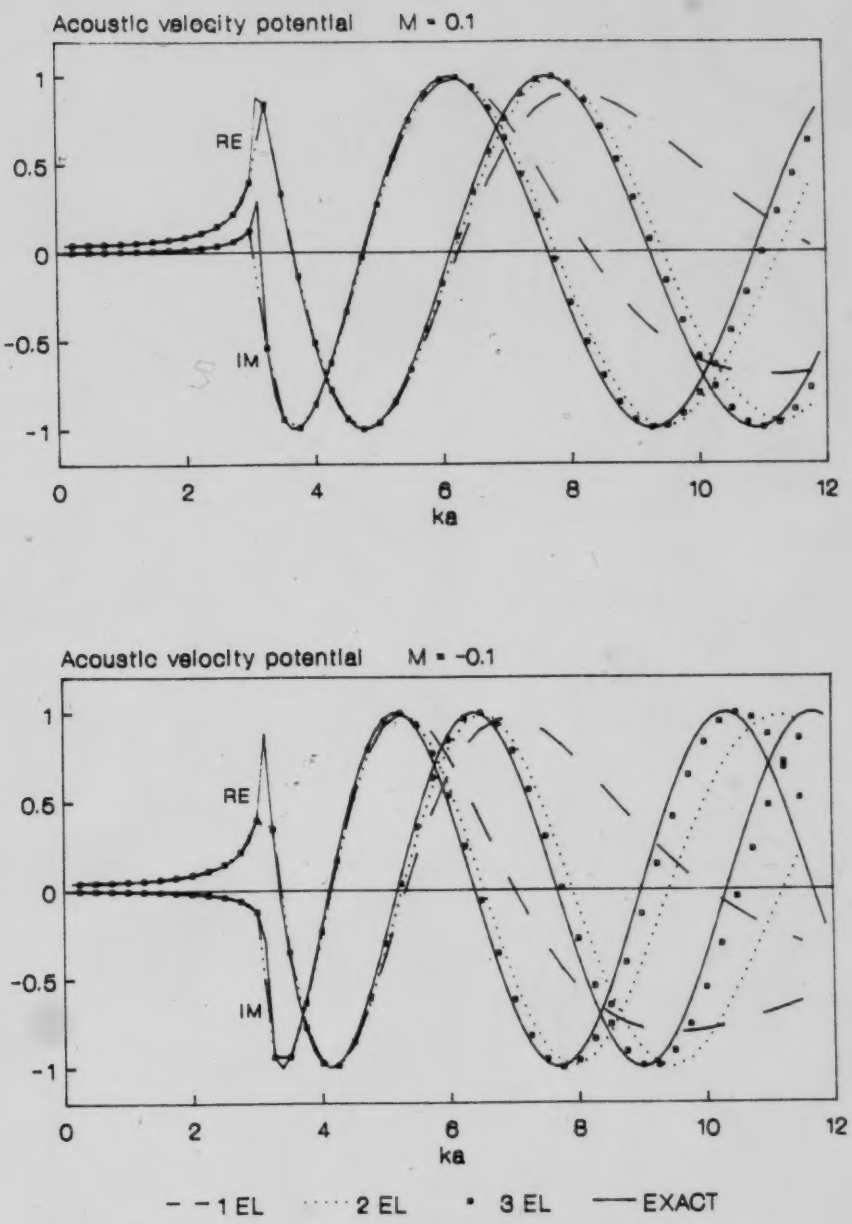

Figure 3.11 Outlet First Cross Mode Acoustic Velocity Potential for a Straight Duct with a Uniform Flow

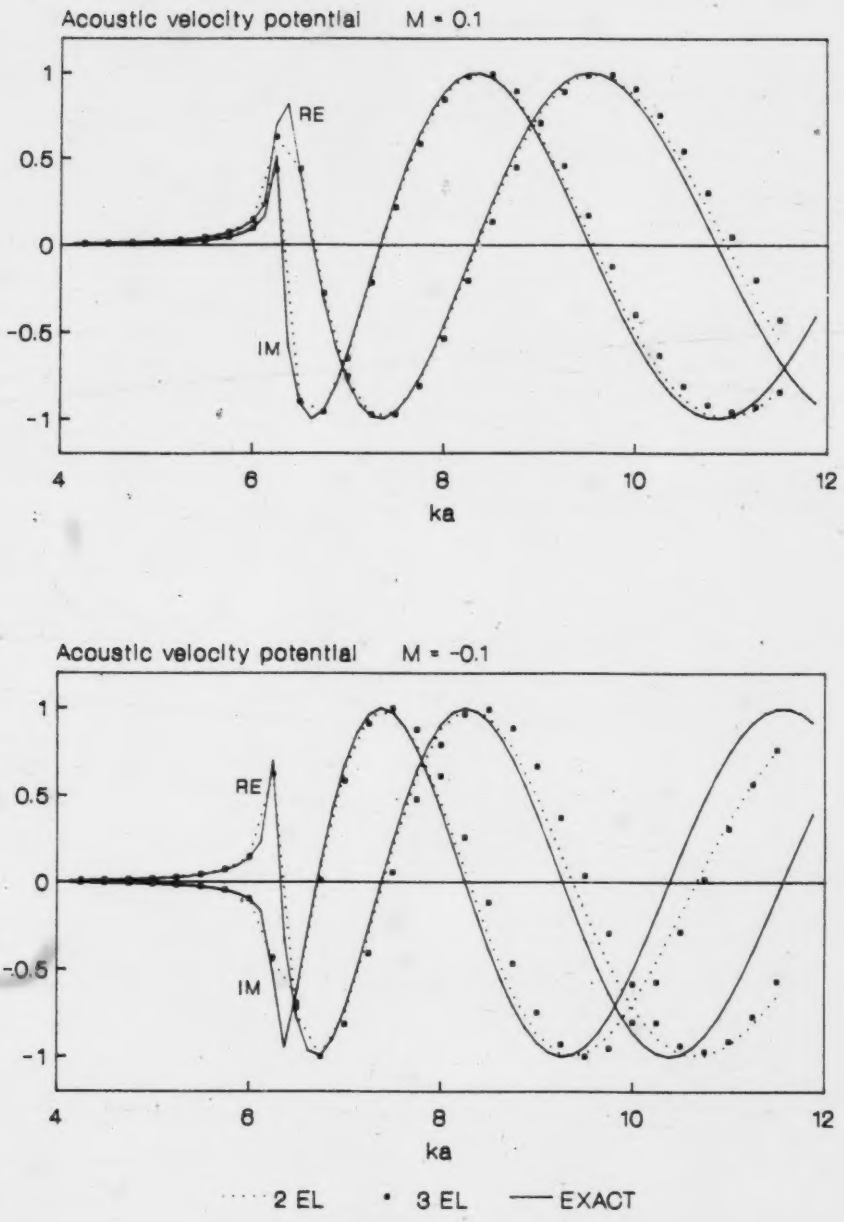

Figure 3.12 Outlet Second Cross Mode Acoustic Velocity Potential for a Straight Duct with a Uniform Flow

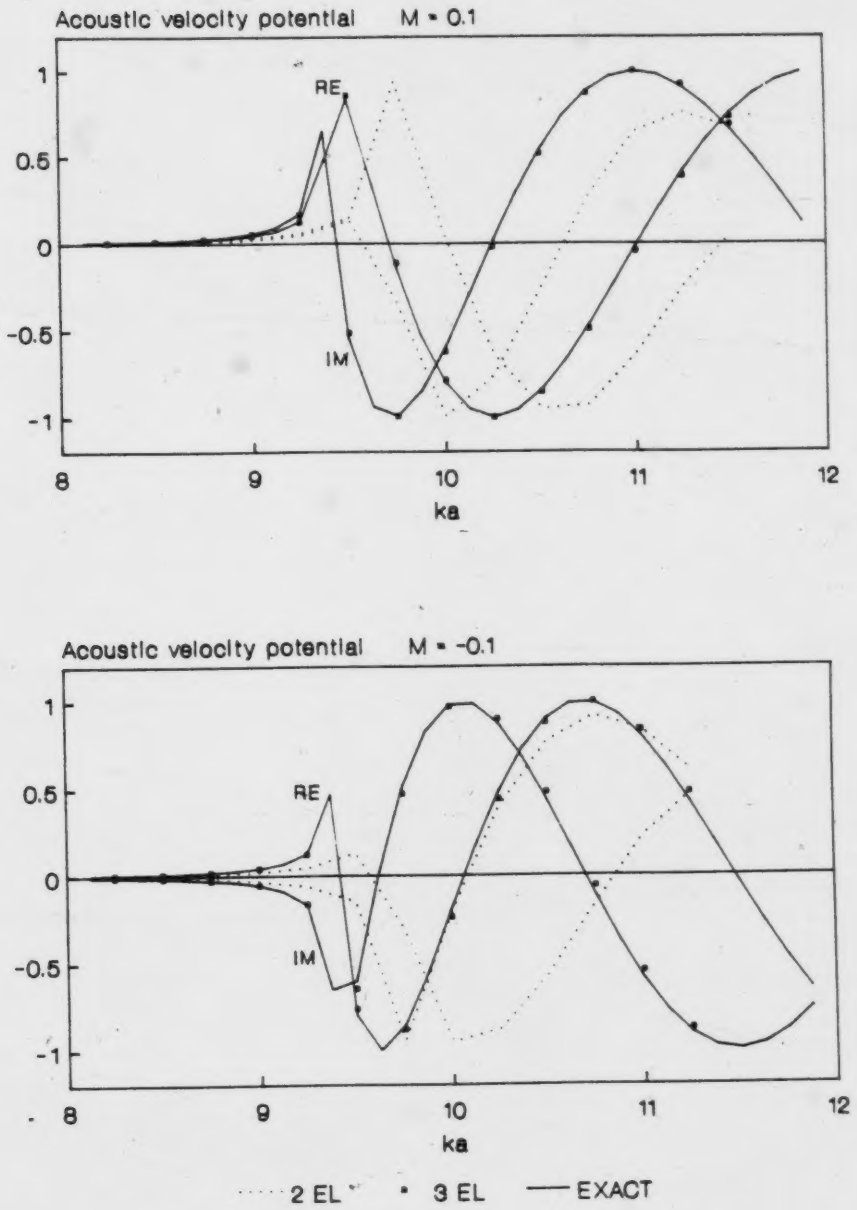

Figure 3.13 Outlet Third Cross Mode Acoustic Velocity Potential for a Straight Duct with a Uniform Flow

for the negative Mach number case. As with no flow, the results for the second cross mode are generally more accurate with two elements across the duct width than with three. Also the model with three elements across the duct width gives accurate results for ka approaching 12 for Mach numbers of 0.1 and -0.1.

In the next chapter considerable work is done in terms of prediction of sound power transmission loss and reflection loss for plane waves and the first cross modes in duct system components. The computer program used has been checked here for the straight duct problem considered above. The results for the reflected and transmitted plane wave with a plane wave incident were identical (to the number of significant digits shown) to that given in Table 3.3 which were based on constraining inputs and outputs to plane waves only. The predicted transmission loss TL and reflection loss RL of the first cross mode with the first cross mode incident are shown in Table 3.6 for the FEM models with one, two and three elements across the duct width. Comparing Table 3.3 and Table 3.6 shows that the one element model gives slightly smaller errors in TL and RL for the first cross mode than for the plane wave. The model with three elements across the duct width generally gave smaller errors for the plane wave than for the first cross mode. The results for the model with two elements across the cross-section were mixed and varied depending on the frequency parameter ka. One puzzling difference between these two tables is that in Table 3.3 for the plane wave propagation, the transmission losses for positive and negative Mach numbers were identical. For the first cross mode case, this is also true for the models with one element and three elements across the duct width. For the case of two elements across the duct width for ka of 10 and 12 (above the cut-on of the third cross mode) the results differ for positive and negative Mach numbers. The following paragraph sheds some light on the reason for this difference.

TABLE 3.6 Convergence for First Cross Mode Propagation in a Straight Duct with the First Cross Mode Incident

ka	One element		Two elements		Three elements	
	RL in dB	TL in dB	RL in dB	TL in dB	RL in dB	TL in dB
$M = 0.0$						
4	53.4	0.000020	53.2	0.000021	59.7	0.000005
6	18.2	0.066406	24.5	0.015551	55.4	0.000013
8	7.9	0.773874	17.2	0.082667	33.8	0.001802
10	4.1	2.110010	35.1	0.090083	21.7	0.029458
12	2.6	3.524120	9.7	0.549310	21.8	0.028759
$M = 0.1$						
4	47.6	0.000111	90.5	0.000000	59.1	0.000015
6	18.9	0.055575	24.1	0.017700	45.7	0.000167
8	8.1	0.730077	17.8	0.071480	32.4	0.002716
10	4.2	2.061800	35.0	0.211718	21.9	0.028250
12	2.6	3.480470	10.6	0.482457	22.6	0.023499
$M = -0.1$						
4	44.3	0.000111	54.3	0.000000	50.4	0.000015
6	19.0	0.055575	23.7	0.017700	42.6	0.000167
8	8.1	0.730077	17.9	0.071480	31.7	0.002716
10	4.2	2.061800	35.3	0.030151	21.9	0.028250
12	2.6	3.480470	10.7	0.441922	22.8	0.023499

In duct components, such as elbows for example, a specified single incident mode can be scattered, contributing sound power to many transmitted and reflected modes. In a straight rigid duct of uniform cross-section a given incident mode will continue to propagate as a single mode with no contributions to other modes. To check how well this was predicted with the straight duct FEM models, the TL and RL values were predicted for the first, second and third cross modes with the plane wave incident and for the plane wave, second and third cross modes with the first cross mode incident. With only one exception the TL and RL gave what appeared to be more or less random values between 280 dB and 320 dB with little dependence on the frequency, Mach number or number of elements. The one exception was the case of two elements across the duct cross-section when looking

at the TL and RL for the third cross mode with the first cross mode incident. For this case with ka greater than the third cross mode cut-on frequency, the RL values ranged from between 10 and 30 dB and TL ranged from 20 to 50 dB depending on frequency and Mach number. Thus, for this case, significantly more sound energy was transferred from the incident first cross mode to the transmitted and reflected third cross mode. This would explain the observation in the previous paragraph concerning different transmission losses for positive and negative Mach numbers at ka values of 10 and 12 in Table 3.6 for the case of two elements across the duct width.

The reason for this apparent transfer of sound energy to a higher mode in this FEM model is not completely understood. Certainly based on Figure 3.9, the model with two elements across the duct width predicts rather poorly the outlet third cross mode velocity potential with the third cross mode incident. With reference to the modal matrix for the two element cross-section model given by Equation 3.124, the modal vectors for the first and third cross modes are given by the second and fourth columns of this matrix. The only difference between these modes is the slope terms given in the third row. However the check of the orthogonality of the mode shapes, discussed in the last paragraph of Section 3.3.1 where the matrix $[\Phi]^T[P][\Phi]$ was evaluated, did not show any higher values for the off-diagonal terms involving the first and third cross modes than for other modes.

Subsequent work concentrates on predictions for the plane wave and first cross mode in duct components up to $ka = 6$. Based on the results for the straight duct problem with undistorted elements, the use of one element across the duct width should give acceptable results up to $ka = 4$, and two elements across the width should give acceptable results up to $ka = 6$ even with a Mach 0.1 flow opposite the direction of acoustic propagation.

3.3.3 Propagation in a Duct Bend

The previous straight duct problem tested the acoustic-flow model with undistorted elements. In this section, the propagation in a duct bend using distorted elements is considered. The bend selected is basically a 90 degree mitred elbow in which the inner corner of the bend has been rounded with a radius of one half the duct width. This bend was considered by Cabelli [10] using eight-noded quadrilateral isoparametric elements.

Meshes with four to thirty-one ISOHERM12 elements were used as shown in Figure 3.14. The normal derivative of ϕ' was constrained to zero at nodes on the bend walls to reduce the number of global DOF. The 113 DOF model was close to the maximum size model that could be handled on the desktop computer system used. The results with no flow for a plane wave incident are shown in Figure 3.15. $R_{\phi'}$ is the acoustic velocity potential reflection coefficient defined as the ratio of the reflected mode velocity potential to the incident mode velocity potential both taken at the duct wall. The transmission coefficient $T_{\phi'}$ is defined similarly base on the ratio of the transmitted and incident modes. The upper and lower graphs on the left hand side of the figure are for the reflected and transmitted plane wave modes and the graphs on the right side are for the reflected and transmitted first cross modes. This also applies to Figure 3.16 in which the results for the first cross mode incident are shown.

Cabelli's results [10] were digitized from a blown up photocopy of the figure and thus may not be reproduced precisely. There is, however, good agreement with the 113 DOF model. There are significant differences between the 113 DOF model and the 52 DOF model for some of the graphs above $ka = 4$, indicating that three elements are needed across the duct in this case to accurately model up to

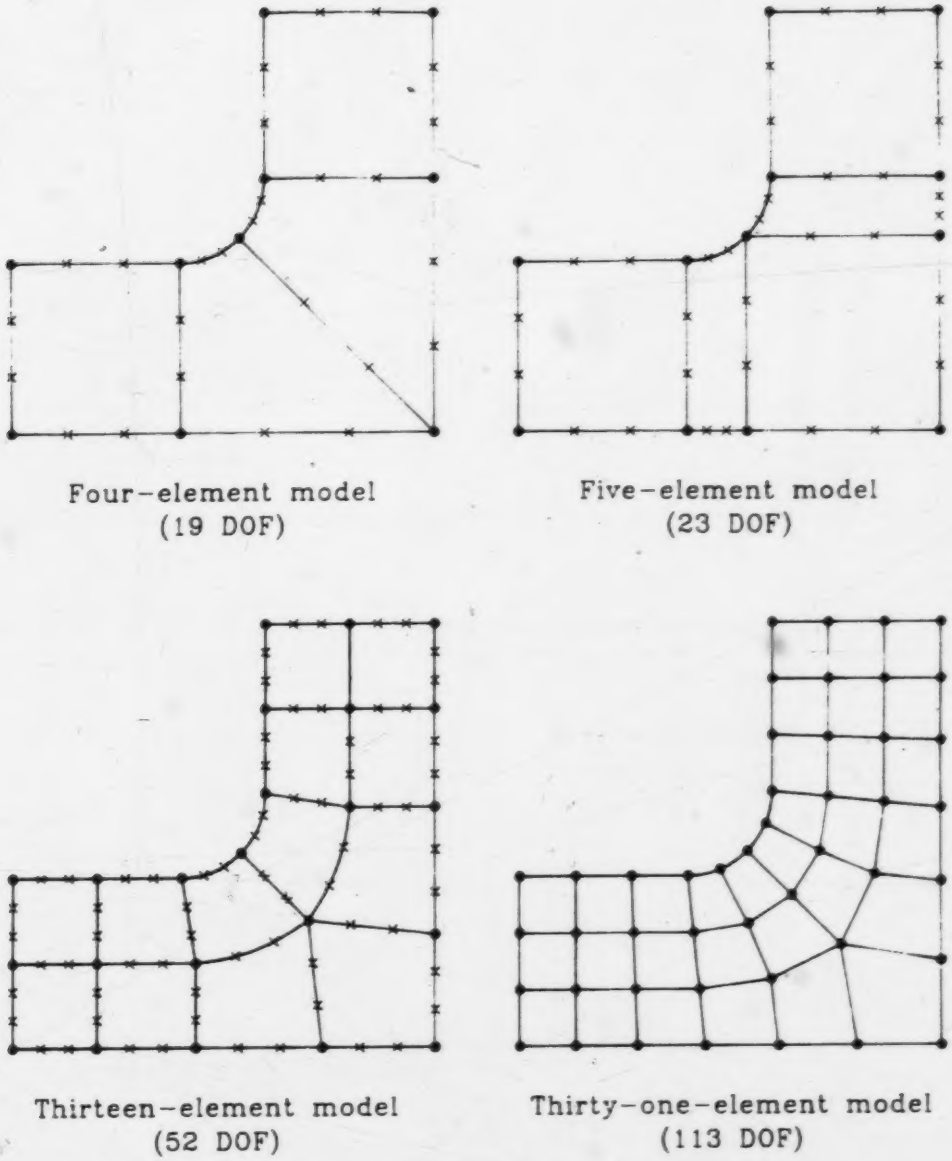

Figure 3.14 ISOHERM12 Finite Element Models for a Duct Bend

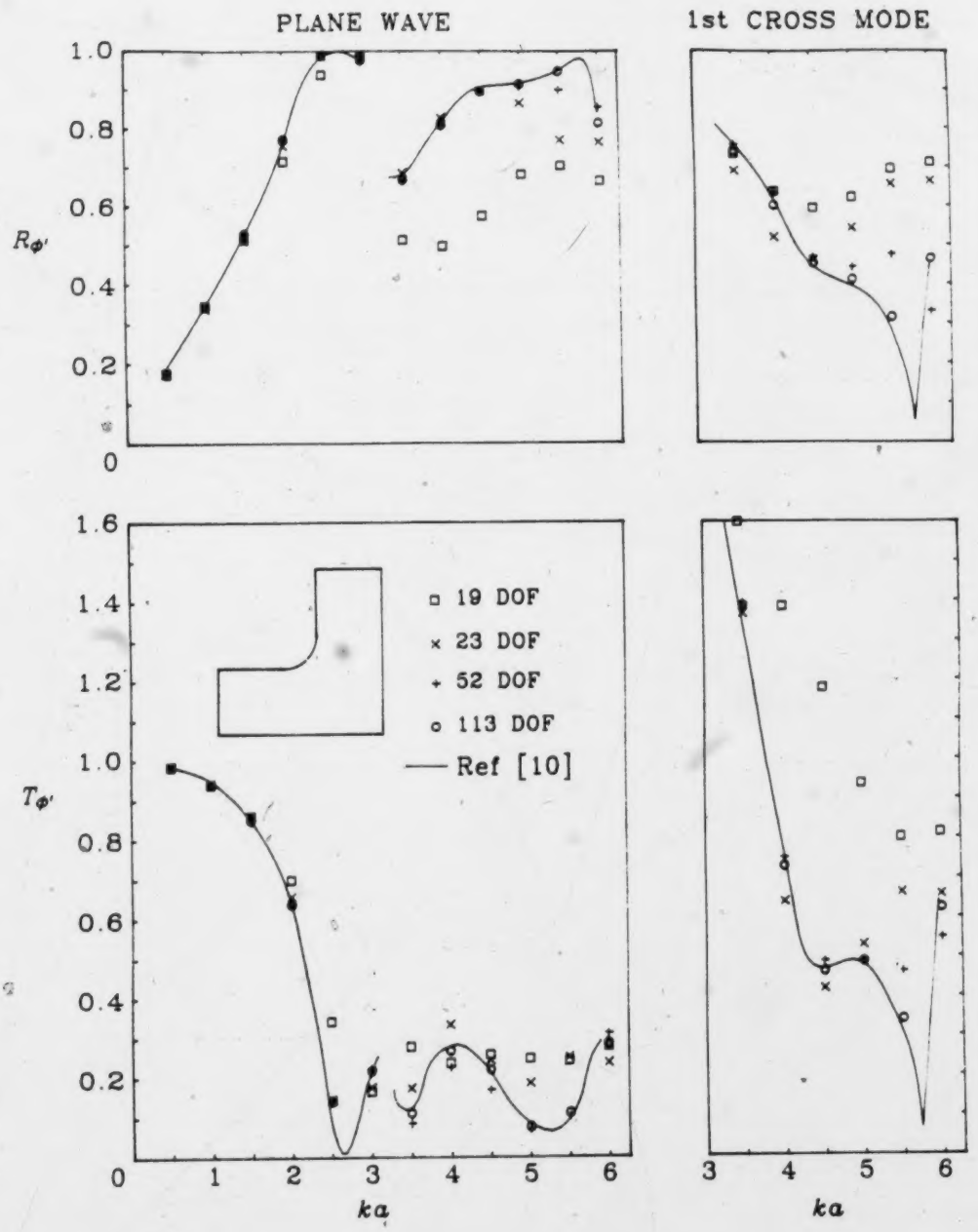

Figure 3.15 Bend Reflection and Transmission Coefficients with a Plane Wave Incident

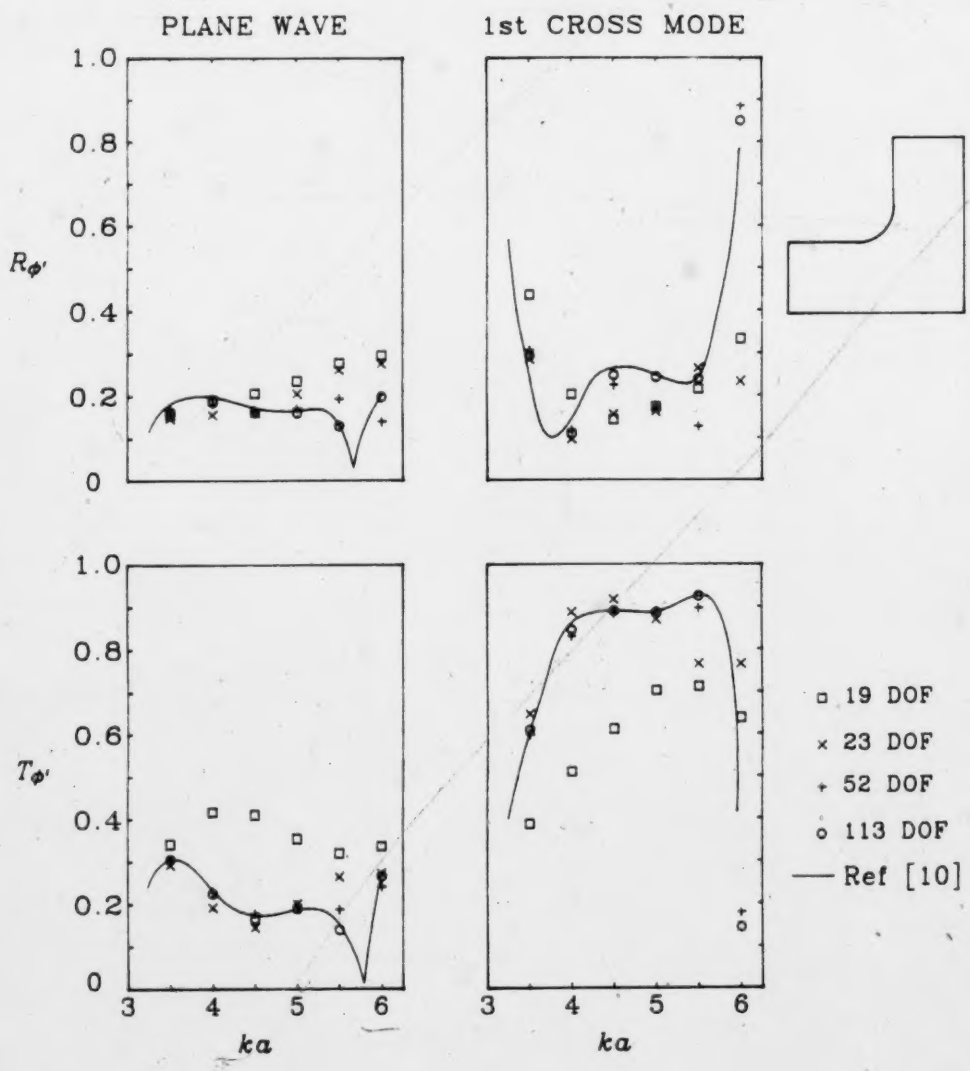

Figure 3.16 Bend Reflection and Transmission Coefficients with the First Cross Mode Incident

$ka = 6$. The need to use a finer mesh compared to that required for the straight duct problem is probably due to the decreased accuracy of the distorted elements but may also be partly due to the more complex acoustic field within the bend.

Two of the four elements in the 19 DOF model were severely distorted and this model gave poor results even at some points below the first cross-mode cut-on at $ka = \pi$. The five-element 23 DOF model, on the other hand, gave generally good agreement up to $ka = \pi$ and in fact reasonable agreement up to $ka = 4$ with the plane wave incident and to $ka = 5$ with the first cross mode incident. In this model three of the five elements are square and two elements long rectangles distorted along one of the short boundaries.

Cabelli also gave results for compressible potential mean flows, with inlet Mach numbers of 0.25 and 0.4, and local Mach numbers reaching 0.39 and 0.66 respectively at the inner curved corner. Some results were obtained for this elbow at these Mach numbers even though the incompressible flow model used was probably not very accurate at these velocities. The resulting transmission and reflection coefficients obtained typically showed smaller effects of flow and poor correlation with Cabelli's results.

The work of Peat [45] uses the same incompressible flow equations as used in this thesis and gives results for a duct expansion chamber for $M = 0.1$. The results are however for an axisymmetric cylindrical expansion chamber, assume plane wave inputs and outputs, given in terms of the muffler four-pole parameters and given only up to $ka = 1.5$. Peat's paper does not give any results for the no-flow case and thus does not indicate how significantly the flow influences the four-pole parameters at this Mach number. It was decided that the limited verification that might be obtained was not at this stage worth the effort necessary to modify

the current computer programs to handle this problem. Thus the straight duct results with flow and the bend results with no flow have been relied on as sufficient verification of the prediction model.

CHAPTER IV

PROPAGATION OF SOUND THROUGH DUCT BENDS AND JUNCTIONS

4.1 Introduction

This chapter is mainly concerned with sound propagation through duct junctions—a subject which has been given relatively little attention in the research literature. The physical problem to be considered is a duct bend or junction connected to infinitely long or anechoically terminated straight ducts. It is assumed that the incident mode or modes in one of the connecting ducts is known. The resulting reflected modes in this duct and the transmitted modes in the other connecting ducts are then to be determined. For example, with a plane wave incident, reflection and diffraction effects within the duct bend or junction can cause the scattering of the plane wave acoustic energy into higher order reflected and transmitted modes.

Considerable work has been done by Cabelli [9], [10] and Cabelli and Shepherd [13], [14], [51] on duct bends of various geometries using both the FDM and the FEM. Two bends are considered in this chapter to examine certain aspects of application of the ISOHERM12 element. The remainder of the chapter is concerned with application of this element to duct junctions or branch points.

4.2 A Mitred 90 Degree Bend

In Section 3.3.3 the propagation of sound through a duct bend requiring the use of distorted ISOHERM12 elements was considered. Three elements were required across the duct cross-section to accurately model the elbow reflection and transmission coefficients up to $ka = 6$ where a is the duct width. This model contained 31 elements and was close to the maximum size model that could be handled on the desk top computer system used for this work. In the subsequent work on duct junctions, it was anticipated that models with three elements across the duct width would be too large for the computer system used. A mitred 90 degree bend has been considered here to test the accuracy of the undistorted element for modeling this type of problem.

The finite element meshes which were used are shown in Figure 4.1. These are identified based on the number of elements across the duct width. In the earlier work of Craggs and Stredulinsky [23] and Stredulinsky, Craggs and Faulkner [55], on elbows and bends within a piping network, finite element models were constrained to plane waves at the interface to connecting straight ducts. The finite element meshes were extended one duct width from the bend or junction to allow some distance for the evanescent modes generated at the bend or junction to decay so that a plane wave boundary condition could be applied at the interfaces. For the case of flow it is also necessary to extend the finite element domains into the connecting straight ducts to model the inlet and outlet flow fields. The prediction method developed in Chapter III includes the evanescent modes in the boundary conditions at the connecting duct interfaces so that, in the absence of flow, it should be possible to shorten the inlet and outlet finite element domains and thus reduce the size of the finite element model. A model with a shortened inlet and outlet called

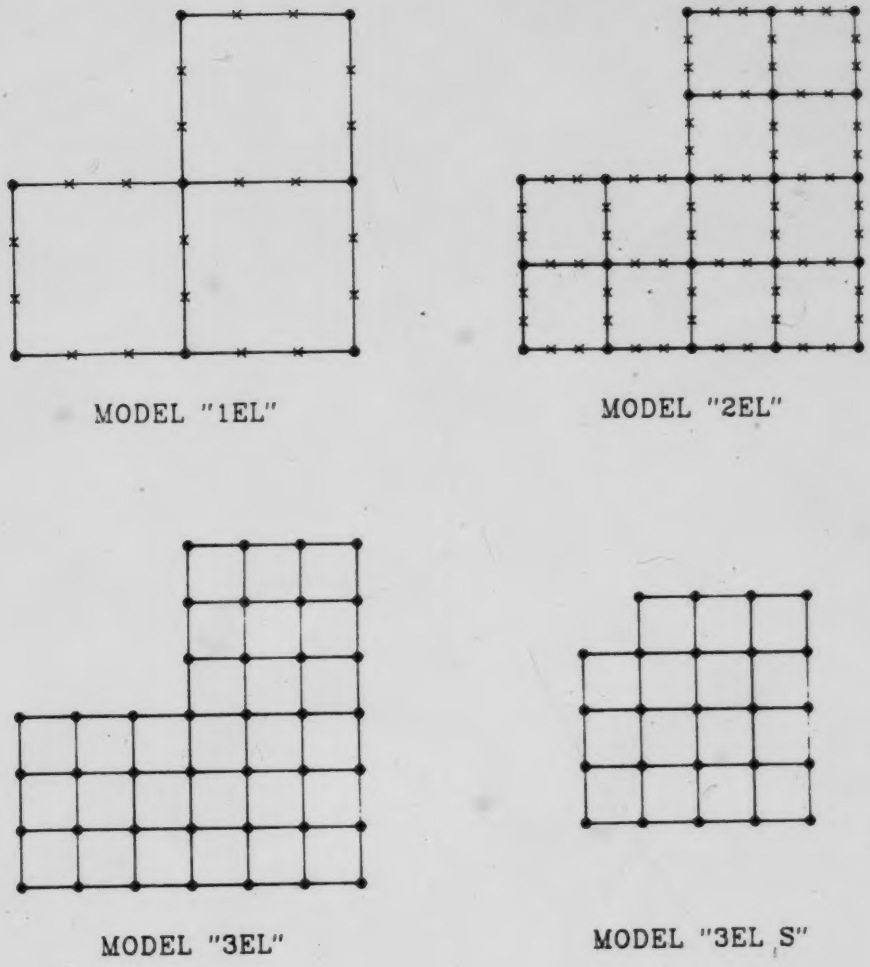

Figure 4.1 ISOHERM12 Meshes for a 90 Degree Mitred Duct Bend

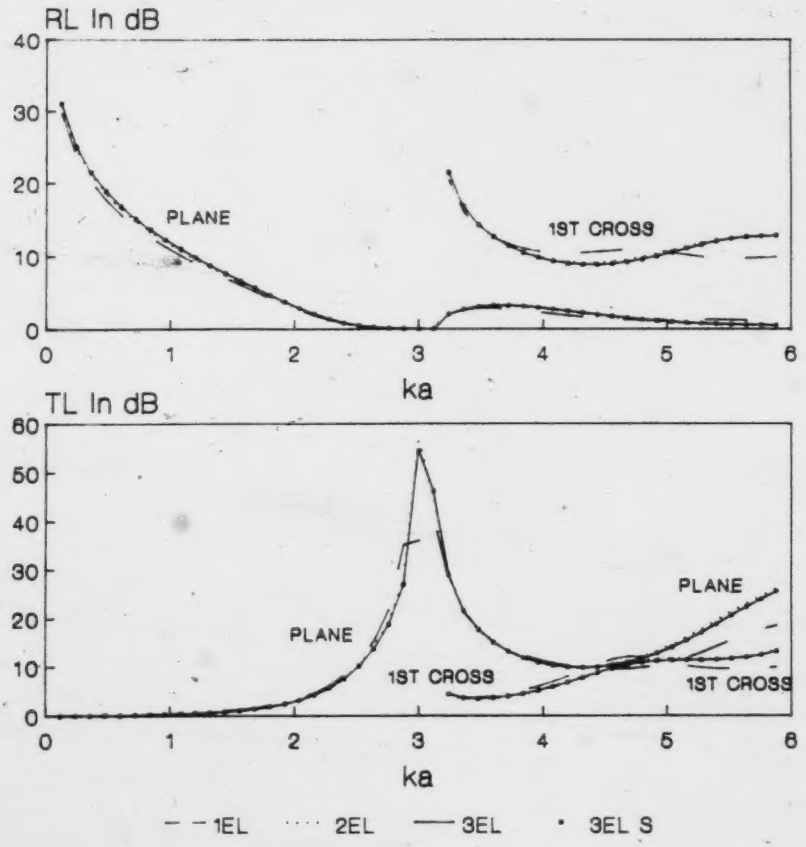

Figure 4.2 Convergence of FEM Models of a 90 Degree Mitred Bend with No Flow and a Plane Wave Incident

model "3EL S" is given in Figure 4.1. It may be possible to reduce this model further to a square composed of nine elements. This would require that the inlet and outlet boundaries be linked at one node—a condition not included in the prediction method development of Chapter III.

The results obtained using these models are compared, for the case of no flow, in Figure 4.2 for a plane wave incident and in Figure 4.3 with the first cross mode incident. Both the reflection loss RL and the transmission loss TL for the plane wave and first cross mode components are shown. The results for

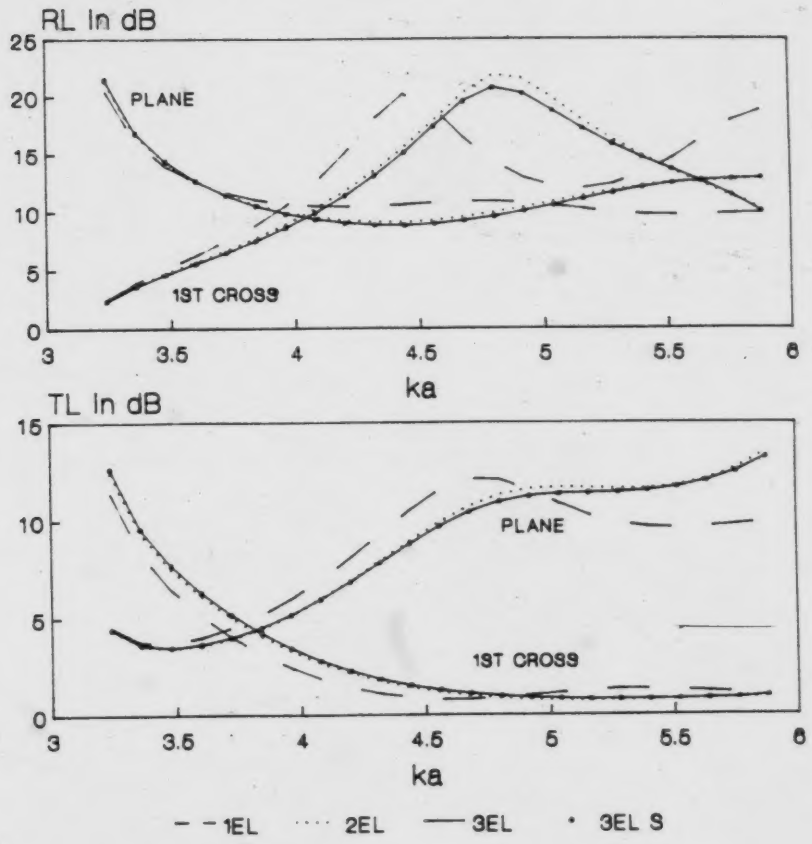

Figure 4.3 Convergence of FEM Models of a 90 Degree Mitred Bend with no Flow and the First Cross Mode Incident

the model "1EL" with one element across the duct width differ significantly from the other models. The "2EL" and "3EL" models differ generally by less than one decibel with differences reaching a maximum of 1.3 dB for the reflection loss with the first cross mode incident and ka between 4.5 and 5. The differences between the "3EL" and reduced "3EL S" models was 0.03 dB or less over the frequency range considered. Thus these results would indicate that undistorted element models with two elements across the duct cross-section should give acceptable results for $ka < 6$. Also in the absence of flow the results indicate that it is not necessary to extend the

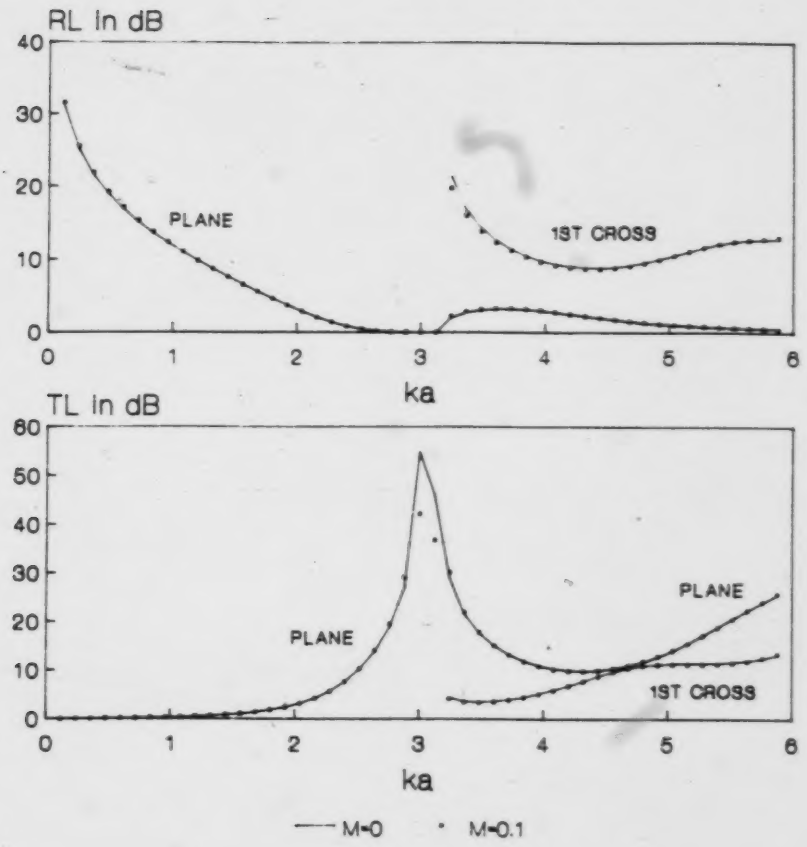

Figure 4.4 Propagation Characteristics of a 90 Degree Mitred Bend with Flow and a Plane Wave Incident

finite element models into the connecting straight ducts (with the restriction that the current prediction method requires that the connecting duct surfaces must be separated).

The velocity potential flow solution for this bend is likely to differ significantly from the actual flow field, since in a real flow, separation is likely to occur at the mitred inner corner. The effect of the potential flow on the propagation characteristics of the bend is shown in Figure 4.4 for a plane wave incident and in Figure 4.5 for the first cross mode incident. In these graphs the reflection loss *RL*

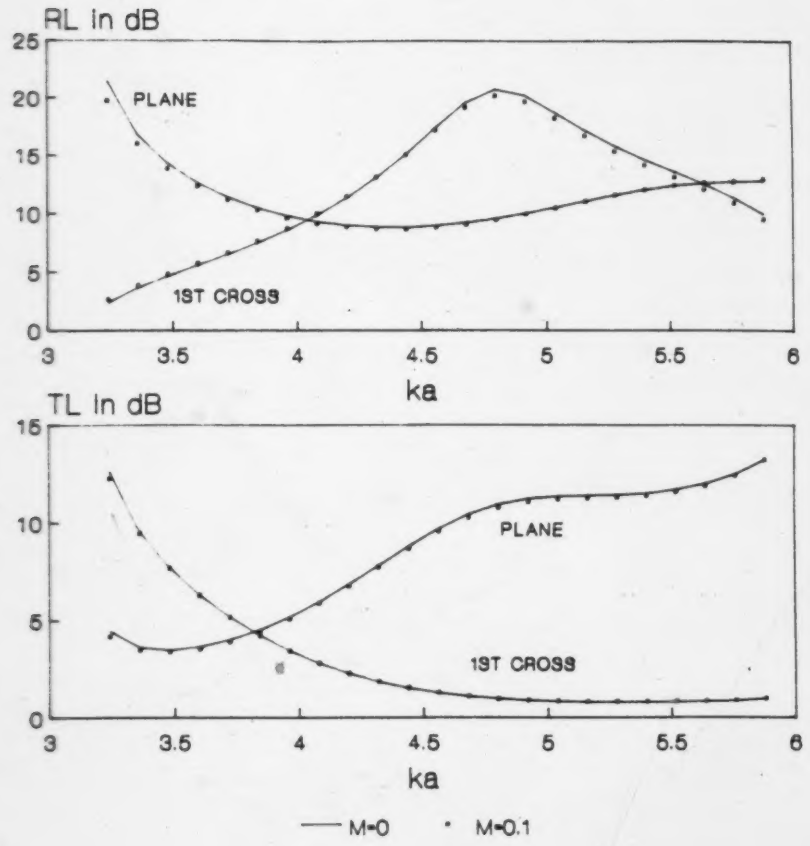

Figure 4.5 Propagation Characteristics of a 90 Degree Mitred Bend with Flow and the First Cross Mode Incident

and the transmission loss TL for no flow are compared to the case with flow with an inlet and outlet Mach number of 0.1 moving in the same direction as the acoustic wave. The effect of flow appears to be very small except near the cut-on frequency of the first cross mode where the plane wave transmission loss with a plane wave incident has changed by approximately 10 dB. The largest differences seem to occur where RL and TL are large—where relative differences in small sound power values are compared.

4.3 A Curved 90 Degree Bend with Turning Vane

The bend to be considered in this section is a 90 degree curved bend with an inner radius of $0.5a$ and an outer radius of $1.5a$, so that the width of the connecting straight ducts is a. A thin rigid turning vane subtending an angle of 90 degrees has been included in the bend for the case with the vane at a radius of $0.875a$ and for the case of the vane at $1.125a$. This bend was considered by Cabelli [9] using the FDM for values of ka up to 3. Without the vane in place, this type of bend has a small transmission loss over this frequency range. With the vane in place, the bend shows a significant peak in transmission loss at a frequency well below the cut-on frequency for the first cross mode in the connecting straight duct.

The finite element meshes used to model these bends are shown in Figure 4.6. Initially models with two elements across the duct width were used. Also, along the turning vane including the end nodes of the vane, the boundary condition that the acoustic velocity normal to vane be zero was used to constrain the acoustic velocity potential derivative nodal degrees of freedom. The reflection and transmission loss results for this model are shown in Figure 4.7 for a turning vane at a radius of $0.875a$, and in Figure 4.8 for a turning vane at a radius of $1.125a$ under the legend item "2ELC". It was then noted that there were significant differences between the predictions with this model and the results of reference [9]. Predictions were then obtained leaving the derivative nodal degrees of freedom at the ends of the vane unconstrained, increasing the number of global degrees of freedom from 74 to 76 and giving the results referred to as "2EL" in Figure 4.7 and Figure 4.8. A third result was obtained using three elements across the cross-section with shortened inlet and outlet FEM domains and again leaving the nodal quantities at the ends of the vanes unconstrained. This result is referred to as "3EL" in Figure 4.7 and Figure 4.8.

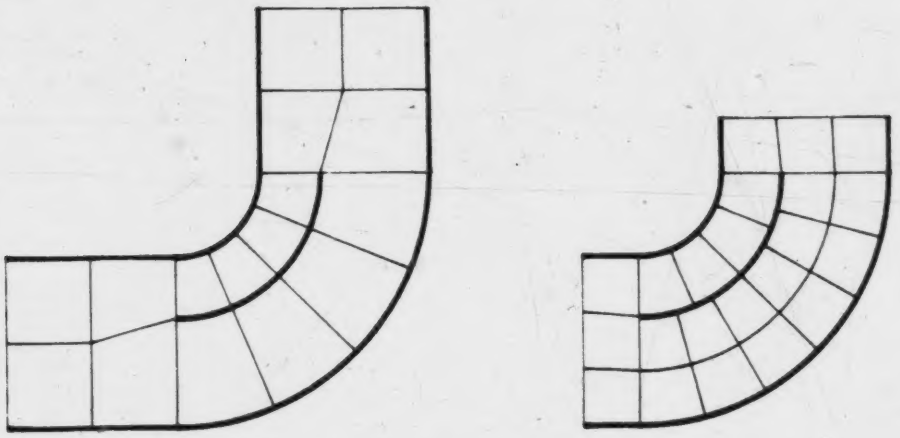

Bend with a turning vane at a radius of 0.875a

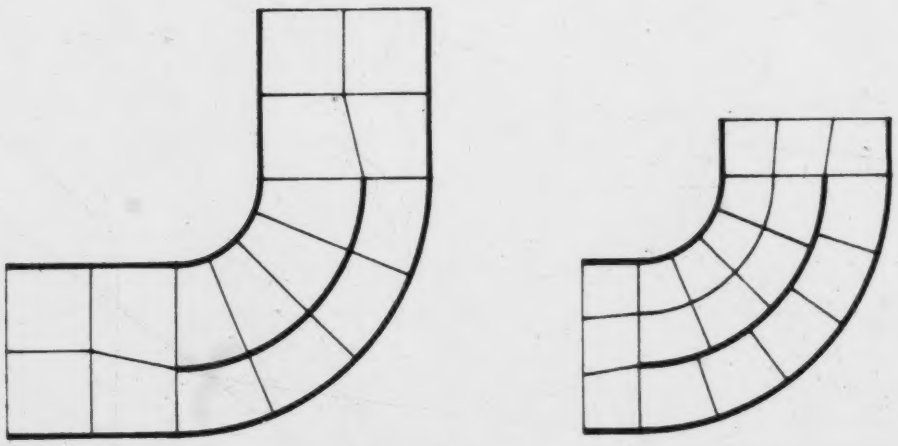

Bend with a turning vane at a radius of 1.125a

Figure 4.6 ISOHERM12 meshes for Curved 90 Degree Bends with an Inner Radius of 0.5a and an outer radius of 1.5a

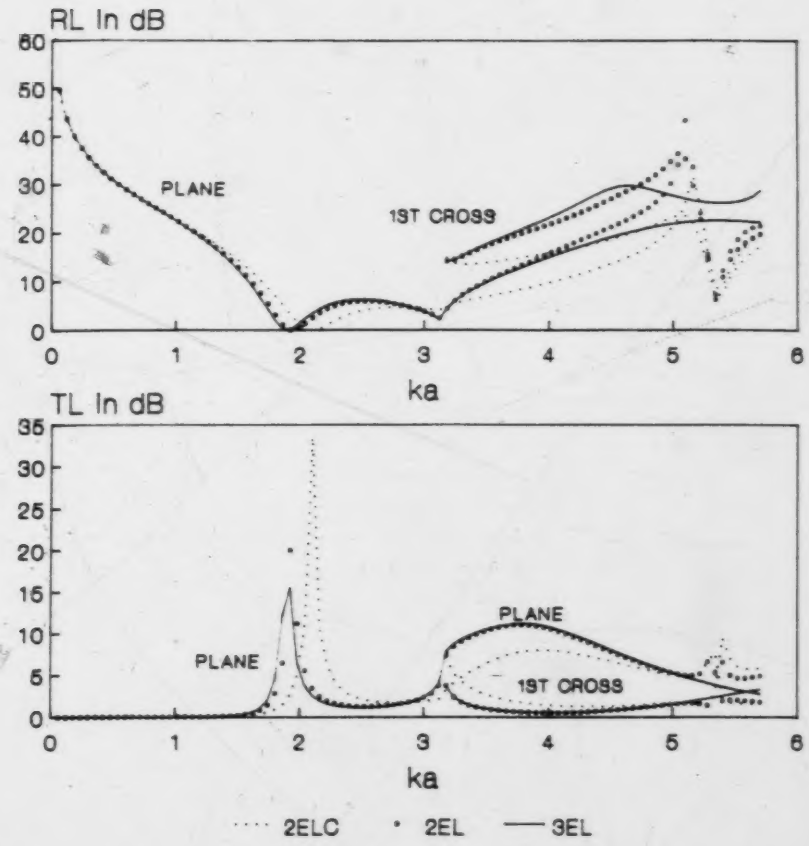

Figure 4.7 Convergence of FEM models for a curved 90 degree bend with a turning vane radius of $0.875a$ and a plane wave incident

These figures show an eight percent shift in ka for the peak in the plane wave transmission loss located at approximately $ka = 2$ in Figure 4.7 and a slightly smaller shift in Figure 4.8 when comparing the "2ELC" and "2EL" results. Also there are significant differences in transmission loss values for these two models above $ka = 1.5$. The "2EL" and "3EL" results are much closer, but still show some shift in the first TL peak and significant differences in the RL values above $ka = 4$ and in TL above $ka = 5$.

These results indicate that even in the range of ka between 1.5 and 2,

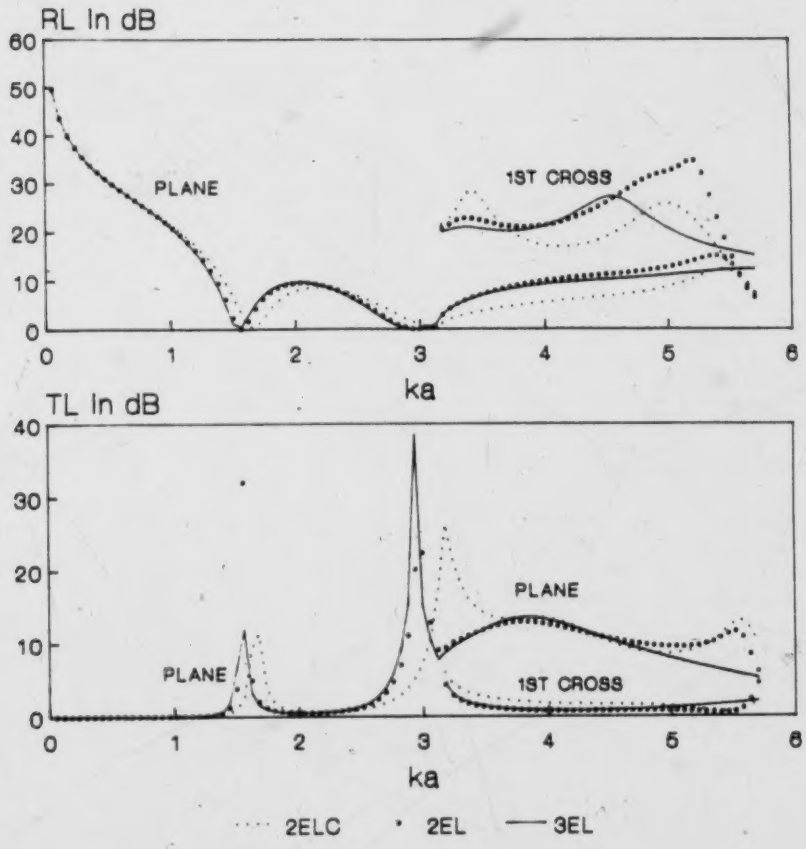

Figure 4.8 Convergence of FEM models for a curved 90 degree bend with a turning vane radius of $1.125a$ and a plane wave incident

the finite models have still not converged, even with three elements across the inlet and outlet width. Based on the previous elbows considered, this was unexpected. The bend with a curved inner corner shown in Figure 3.15, which involved distorted elements, showed good agreement between models with one and two elements across the duct width and insignificant differences between models with two and three elements across the duct width in this frequency range. At present it is not known whether the poorer result for this bend is due to the nature of the distortion of the elements or possibly the more complex sound field created by the presence

of the turning vane. These results also confirm, as found in modeling a complex shaped enclosure in Section 2.3.4, that constraining the derivative nodal quantities at boundary discontinuities can over-constrain the FEM models leading to increased errors. Even though the acoustic velocity normal to the vane is zero at end of the vane, in the fluid just beyond the end of the vane there could be a significant acoustic velocity perpendicular to the vane and therefore it is best to leave this node unconstrained and let the implicit boundary condition determine the normal acoustic velocity at the ends of the turning vane.

The FDM predictions of Cabelli [9] and the ISOHERM12 model with three elements across the duct cross-section are compared in Figure 4.9 and Figure 4.10 respectively for the turning vane at a radius of $0.875a$ and $1.125a$. These graphs show the plane wave transmission loss for a plane wave incident. Cabelli's results were digitized from a small figure which was given in terms of the reflection coefficient and the converted to transmission loss values and thus may not be reproduced precisely. Cabelli's results show the first transmission loss peak at a significantly lower frequency than the ISOHERM12 results and probably lower than values to which ISOHERM12 models with finer meshes are likely to converge. It was noted in Cabelli's paper, that using the FDM, the ends of the vane could only be determined to within one mesh space and for the vanes considered, the angle subtended by the vane was between 72 and 90 degrees. His experimental work on other bends with turning vanes consistently showed that the best approximation corresponded to the upper limit. In view of the above, some additional experimental results were obtained using an existing facility at the University of Alberta for measuring duct component transmission loss using the transfer function method of Chung and Blaser [15], [16].

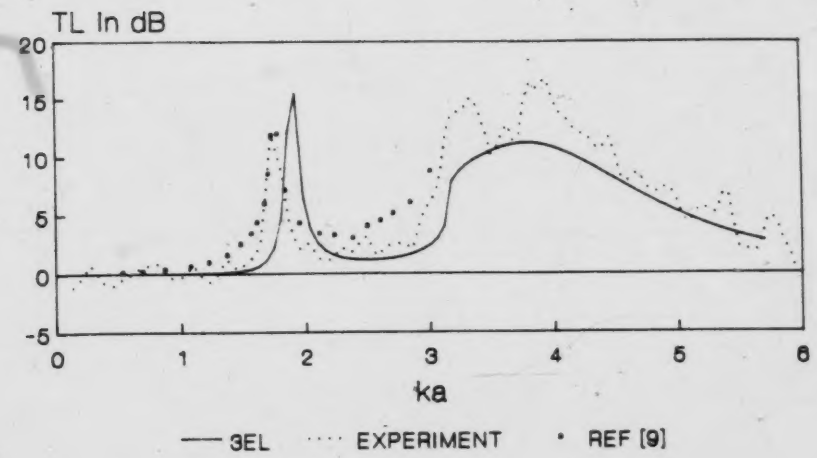

Figure 4.9 Comparison of the FEM with Experiment and the FDM of Reference [9] for the Plane Wave Transmission Loss of a Curved 90 Degree Bend with a Turning Vane at a Radius of 0.875a

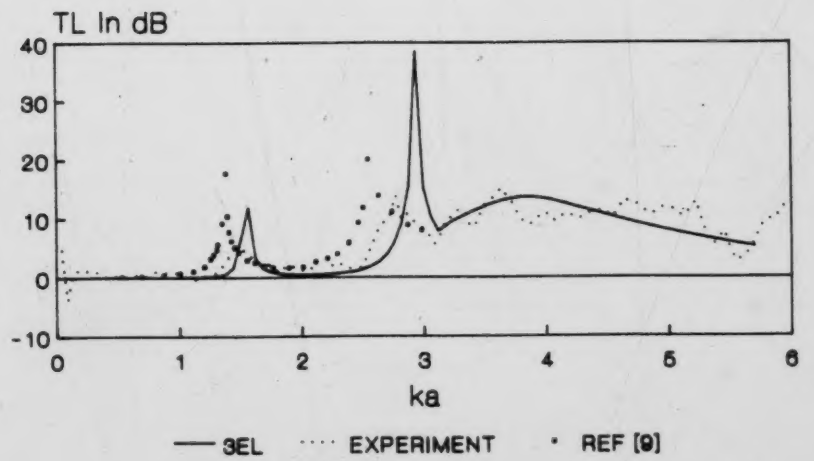

Figure 4.10 Comparison of the FEM with Experiment and the FDM of Reference [9] for the Plane Wave Transmission Loss of a Curved 90 Degree Bend with a Turning Vane at a Radius of 1.125a

The noise generation apparatus used in this experimental work consisted a white noise source, and amplifier driving an array of four small loudspeakers at the entrance of a straight inlet duct. This inlet duct was connected to the test bend which in turn connected to an outlet duct with an anechoic termination. The measurement apparatus consisted of two 1/4 inch B&K 4145 microphones, a B&K 2807 microphone power supply and a dual channel Nicolet 660A FFT spectrum analyser controlled by an HP Integral computer.

The experimental procedure was developed for measurement of plane wave transmission loss. The speaker array could be configured as a monopole, dipole or quadrapole—for the present measurement the monopole configuration was used to excite mainly the plane wave mode in the inlet duct. Measurement test stations were located upstream and downstream of the test bend. The microphones were located flush to the inner duct wall and spaced 24 mm apart along the axis of the duct, midway across the duct face in the plane of the bend. These measuring points were chosen to be at the nodal plane of the first cross mode so that the plane wave transmission loss measurement could be extended above the cut-on of the first cross mode [1,0] at $ka = \pi$ where a is the width in the plane of the bend. The actual bend considered, had an inner corner radius of 100 mm and outer radius of 300mm, with the turning vane located at either a radius of 175mm or 225mm. The vane was assumed to have zero thickness in the FEM predictions but actually had a thickness of 5mm. The rectangular connecting ducts had an inside dimension of 200 mm in the plane of the bend and 150 mm in the perpendicular dimension. Thus additional cut-on frequencies of $ka = 4.19$ for the [0,1] mode and of $ka = 5.23$ for the [1,1] modes were in the frequency range considered.

The experimental procedure consisted of measuring the acoustic transfer function and auto-spectrum with the two microphones at the upstream measure-

ment station (averaging 192 FFT traces) and then repeating the measurements at the downstream station. This data was transferred and used by the HP Integral computer to calculate transmission loss values. The results for the bend at a radius of $0.875a$ are shown in Figure 4.9. The location of the first experimental transmission loss peak is closer to Cabelli's result than the "3EL" ISOHERM12 model result. For the case of the vane at a radius of $1.125a$ the first peak in the transmission loss is shifted to a lower frequency and both Cabelli's prediction and the ISOHERM12 "3EL" prediction show a second peak at roughly double the frequency at which the first peak occurs. Again Cabelli's FDM result is lower than the FEM result. The peaks in the measured transmission loss curve are smaller than either predicted result and located midway between the predicted peaks.

There is certainly further work needed to resolve the above differences, including using the FEM models with finer meshes (probably requiring the use of a larger computer system) and comparing with FEM models using, for example, the HEX12 element. The actual thickness of the vane could also be modeled, although since this thickness is less than 3% of the duct width this is not expected to have a significant influence.

4.4 Propagation Through Duct Junctions

Compared to the amount of research done on duct bends, there has been relatively little work done on duct junctions where three or more ducts join at a common junction (restricted to three ducts in the present work). Some analytical work has been done for "T" junctions and 90 degree side branches for simple two dimensional rectangular geometries which involve solution of the Helmholtz equation in Cartesian coordinates and boundaries parallel to the coordinate axes. Miles [39] considered a "T" joint of equal width tubes using an electrical circuit analogy which

limited his approach to plane waves and assumed higher order modes decayed over short distances. In Miles' formulation any tube leading into the "T" could be chosen for the incident wave. The plane wave reflection coefficient and the transmission coefficients for the other branches could then be determined. This "T" junction was also considered by von Said [57]. In von Said's work, higher order modes were considered. An incident plane wave or the first cross mode were considered entering the stem of the "T" and the total reflection coefficient and transmission coefficient for the symmetric outlet ducts determined up to the cut-on of the fourth cross mode. He did not give individual mode reflection and transmission coefficients.

A different approach is taken by Redmore and Mulholland [46] who used a mode coupling theory to predict the sound pressure in a 90 degree side branch attached to a semi-infinite straight rectangular duct, with a source distribution at one end. This approach assumes that the modal sound field in the main duct is not affected by the presence of the side branch, and that the disturbances caused by this sound field at the common plane between the side branch and the main duct become the source for the sound field in the branch duct.

The subsequent work in this chapter considers the junction problem in which three semi-infinite straight ducts meet at a junction. The incident wave modal mixture approaching the junction along one of the ducts is specified and the reflection loss (the transmission loss for the reflected wave) and the transmission losses for each mode in the two outlet ducts determined. Before considering some specific applications two low frequency approximations will be considered in the next section. These are used in subsequent sections for comparison purposes.

4.4.1 Low Frequency Approximations for Duct Junctions

At very low frequencies, the classical approach to plane wave propagation in pipes can be used to predict the reflection and transmission losses for pipes connected at a common junction point. The acoustic pressure is assumed to be constant in the vicinity of the junction so that the combined incident wave plus reflected wave acoustic pressures in the inlet duct can be taken as equal to the acoustic pressures of the transmitted plane waves in the two outlet ducts (only valid at low frequencies). These conditions and the continuity condition that the incident plus reflected wave volume velocities must equal the combined outlet wave volume velocities, can be used to determine the reflected and transmitted plane waves for a given incident plane wave. The reflection loss RL for the reflected wave in the inlet duct and the transmission losses TL_1 and TL_2 for the two outlet ducts are then given by

$$RL = 10\log_{10}\left(\frac{1}{R}\right) = 10\log_{10}\left[\left(\frac{S_{in} + S_{out1} + S_{out2}}{S_{in} - S_{out1} - S_{out2}}\right)^2\right] \tag{4.1}$$

$$TL_1 = 10\log_{10}\left(\frac{1}{T_1}\right) = 10\log_{10}\left[\frac{(S_{in} + S_{out1} + S_{out2})^2}{4S_{in}S_{out1}}\right] \tag{4.2}$$

$$TL_2 = 10\log_{10}\left(\frac{1}{T_2}\right) = 10\log_{10}\left[\frac{(S_{in} + S_{out1} + S_{out2})^2}{4S_{in}S_{out2}}\right] \tag{4.3}$$

where R and T are the reflection and transmission coefficients respectively and S_{in}, S_{out1}, and S_{out2} are the cross-sectional areas of the inlet and two outlet ducts. Note that the results are only dependent on the duct cross-sectional areas and are independent of the junction geometry and frequency.

The work of Miles [39] for a "T" junction leads to ninefold infinity of simultaneous equations. If all higher order modal terms are dropped from these

equations, as a first approximation the following equations are obtained for a 90 degree side branch with ducts all of width a. A matrix Y can be formed as

$$[Y] = \begin{bmatrix} \frac{1}{\tan ka} & \frac{1}{\sin ka} & -\frac{1}{ka} \\ \frac{1}{\sin ka} & \frac{1}{\tan ka} & -\frac{1}{ka} \\ -\frac{1}{ka} & -\frac{1}{ka} & \frac{1}{\tan ka} \end{bmatrix} \tag{4.4}$$

where k is the wave number and a is the duct width, then let $[Z] = [Y]^{-1}$. A matrix $[C]$ can then be defined by

$$[C] = \begin{bmatrix} [I] & -[Z] \\ [Z] & [I] \end{bmatrix} \tag{4.5}$$

where [I] is the identity matrix. Also a column vector $\{D\}$ can be defined by

$$\{D\} = \begin{Bmatrix} -1 \\ 0 \\ 0 \\ Z_{11} \\ Z_{12} \\ Z_{13} \end{Bmatrix} \tag{4.6}$$

where Z_{11}, Z_{12} and Z_{13} are elements of the first column of $[Z]$. These can be used to form the linear system of equations

$$[C]\{\beta\} = \{D\} \tag{4.7}$$

which can be solved for the vector β containing the real and imaginary parts of the pressure reflection and transmission coefficients. The reflection loss and transmission loss value TL_{br} for the side branch and TL_{ct} for the continuing straight duct are then

$$RL = 10\log_{10}\left(\frac{1}{(\beta_1)^2 + (\beta_4)^2}\right) \tag{4.8}$$

$$TL_{\text{br}} = 10\log_{10}\left(\frac{1}{(\beta_3)^2 + (\beta_6)^2}\right) \tag{4.9}$$

$$TL_{\text{ct}} = 10\log_{10}\left(\frac{1}{(\beta_2)^2 + (\beta_5)^2}\right). \tag{4.10}$$

4.4.2 FEM Predictions for a 90 Degree Equal Width Side Branch

The first duct junction to be considered was a 90 degree side branch in a rectangular duct with a side branch having the same cross-section dimensions as the main straight duct. This junction was modeled in two dimensions using the ISOHERM12 meshes show in Figure 4.11. Based on the ninety degree mitred elbow results of Section 4.2, it was anticipated that the use of two elements across the cross-section would give acceptable accuracy up to $ka = 6$. The computer used did not have sufficient memory to handle the problem with three elements across the duct width if the finite element domain was extended one duct width into each connecting straight duct. The model "3EL S", with shortened inlet outlet finite element domains was used to check the convergence of the FEM models for the no-flow case. With reference to Figure 4.11, the incident wave was taken to enter the left hand duct. A wave could then be reflected back down this inlet duct and waves could be transmitted out the side branch and the continuing main duct to the right of the FEM model.

The RL and TL values predicted by the ISOHERM12 models with no flow and a plane wave incident are shown in Figure 4.12 as a function of ka based on the duct width. "PL" in the legend refers to the reflected and transmitted plane wave components and "1X" refers to the first cross mode components. Except close to the cut-on of the first cross mode at $ka = \pi$ for the reflection loss RL, the difference between the "2EL" and "3ELS" curves is less than one decibel. Thus the "2EL" models could be used to give a reasonable indication of the junction sound propagation. Similar convergence of FEM models was obtained in Figure 4.13 for the case of the first cross mode incident.

Figure 4.14 compares the plane wave results for the "3EL S" model to the simple low frequency (frequency independent) approximation and Miles [39] first

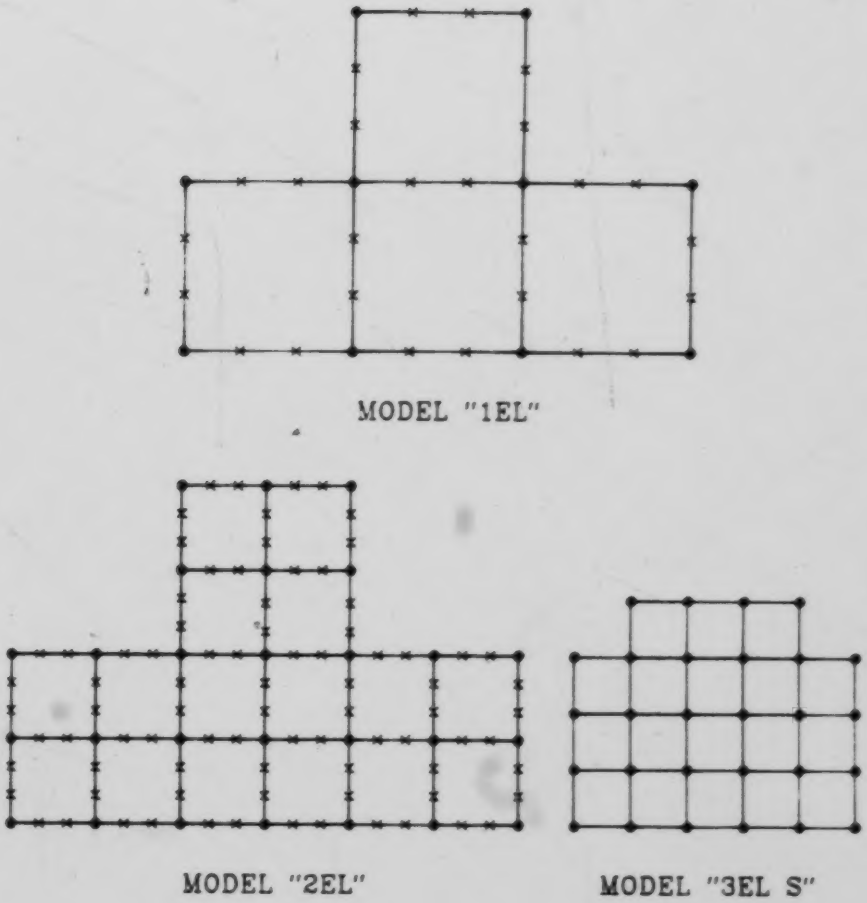

Figure 4.11 ISOHERM12 Meshes for a 90 Degree Side Branch with Equal Width Ducts

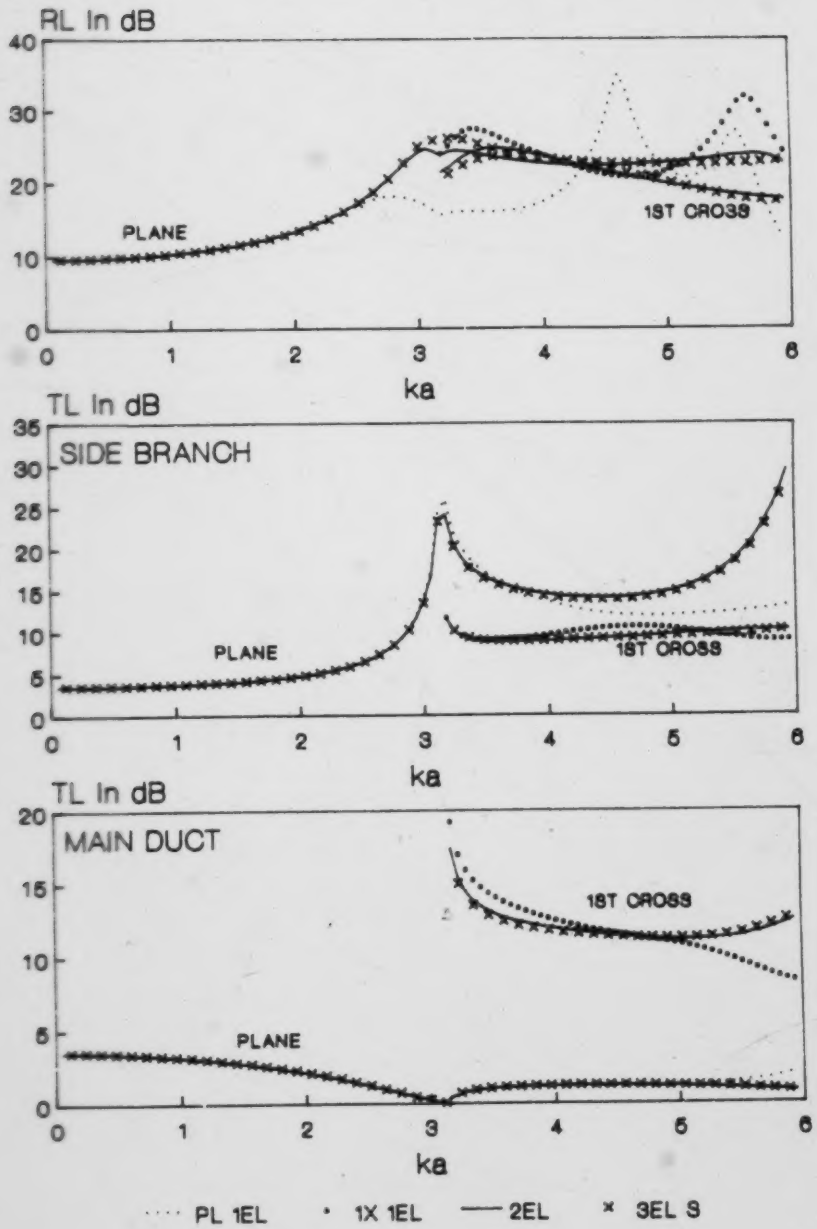

Figure 4.12 Convergence of FEM Models for a 90 Degree Side Branch with the Same Width as the Main Duct and a Plane Wave Incident with No Flow

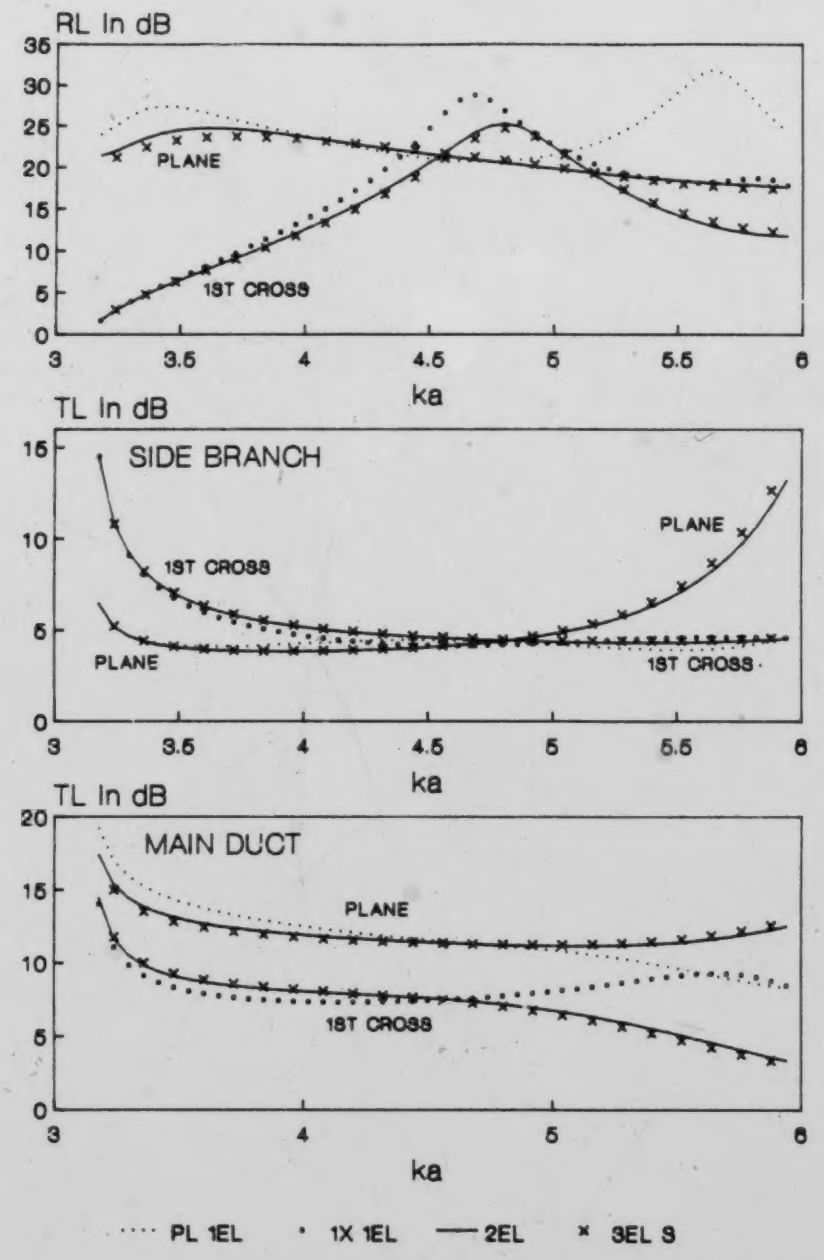

Figure 4.13 Convergence of FEM Models for a 90 Degree Side Branch with the Same Width as the Main Duct and the First Cross Mode Incident with No Flow

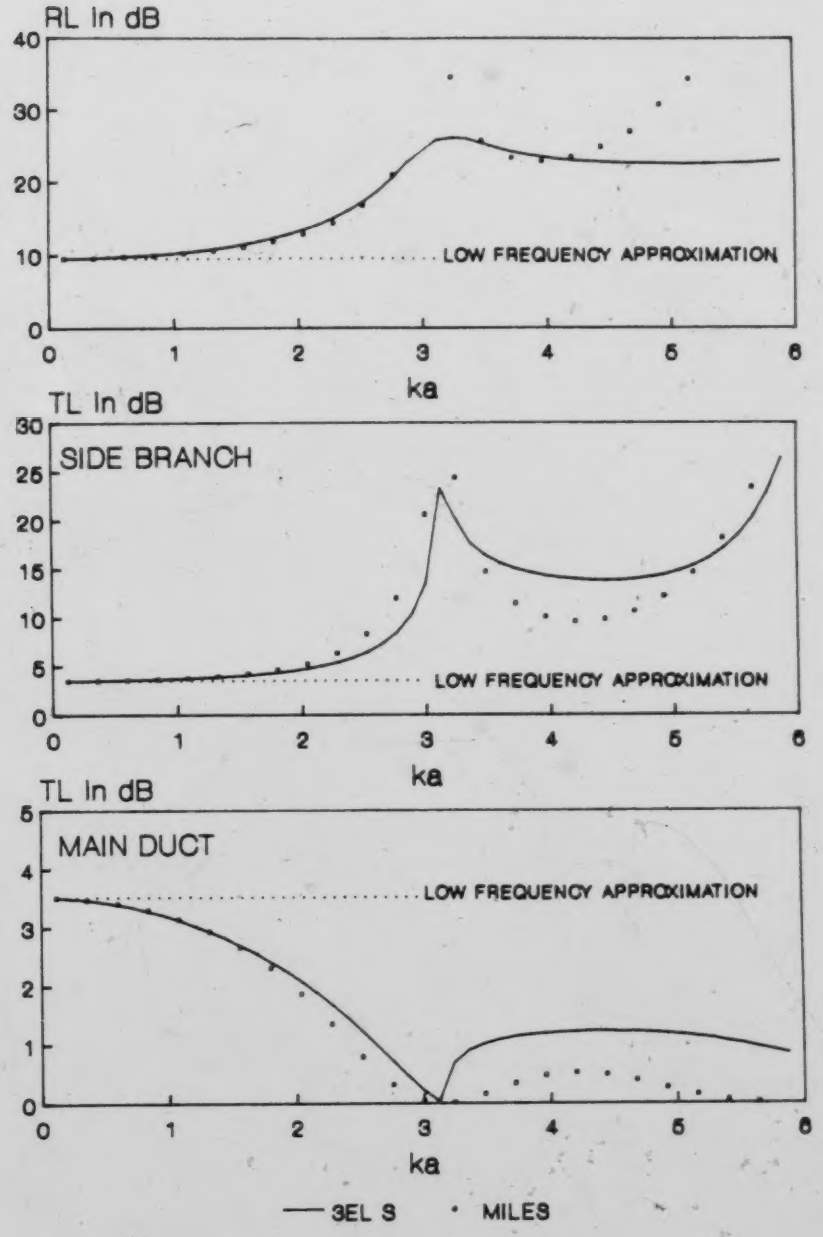

Figure 4.14 Comparison with Other Approximate Solutions for a 90 Degree Side Branch with the Same Width as the Main Duct and a Plane Wave Incident with No Flow

approximation discussed in the previous section. At $ka = 0.06$ the three predictions agree within 0.002 dB. This figure indicates that the simple low frequency result can be used to predict the RL and TL values to within one decibel up to a ka of between 1 an 1.5. Miles results shows good agreement up to $ka = 2$ and generally shows similar trends as the FEM prediction over most of the frequency range considered.

The effect of flow at Mach 0.1 on the propagation characteristics of a 90 degree mitred bend was found to be small as discussed in Section 4.2. For the case of a duct junction its was anticipated that perhaps greater changes due to flow could occur because of the more complex flow field. Certainly a junction leads to many more flow possibilities, including different combinations of flow direction in the connecting ducts and variation of flow rates in the ducts. Two flow configurations have been considered here. In the first (M indicated as positive), the flow has been taken to be in the same direction as the acoustic propagation—into the inlet duct with the incident wave and the out the side branch and the continuing duct. In the second case (M indicated as negative), the flow has been taken in the opposite direction—into the junction from the side branch and the main continuing duct and out the acoustic inlet duct—opposite to the direction of the incident and transmitted acoustic waves.

The ISOHERM12 mesh used to model this junction with flow was the model "2EL" shown in Figure 4.11. As indicated in Section 4.2 for the mitred bend, the potential flow through this junction which contains sharp mitred corners may not be very realistic but hopefully will provide some indication of the flow effects. Also it would have been desirable to also use models with three elements across the duct width in order to check the convergence of the predictions. It was not possible, however, to run a model of this size on the computer system used in this work. The

results for inlet Mach numbers of 0, 0.1 and −0.1 are shown in Figure 4.15 for a plane wave incident, and in Figure 4.16 for the first cross incident, for the case of an equal flow split. With an inlet Mach number of 0.1, since the connecting ducts have the same cross-sectional area, the branch and continuing main duct flows were at Mach 0.05. Excluding the region near the cut-on frequency for the first cross-mode at $ka = \pi$, the changes due to flow were less 0.2 decibel below this frequency and less than one decibel above it.

Figure 4.17 graphs the differences in RL and TL for the cases with flow compared to the no-flow case for a plane wave incident. The graph for the reflection loss shows the most complex variation with frequency. The graphs indicate that the flow has a greater influence on the plane wave transmitted in the branch than on the first cross mode. The opposite appears to occur for the transmission down the continuing main duct—here the flow appears to have little effect on the plane wave transmission but a significant effect on the first cross mode transmission particularly at higher frequencies. Additional results were obtained for the case of only 10% of the flow out the side branch and for the case of 90% of the flow out the side branch. The results for these cases with a plane wave incident are given in Figures 4.18 and 4.19. The comments made concerning the case with 50% branch flow apply for these cases as well. In comparing the 10% and 90% branch flow cases, significant changes were noted in the RL values, most noticeable for the first cross mode. The transmission down the side branch changed very little. The transmission of the plane wave out the continuing main duct did not change significantly however in going from a 10% branch flow to a 90% branch flow there was generally a decrease in transmission of the 1st cross mode down the continuing main duct.

For the first cross mode incident the results for the three flow cases are given in Figure 4.20, Figure 4.21 and Figure 4.22. Again as a function of frequency,

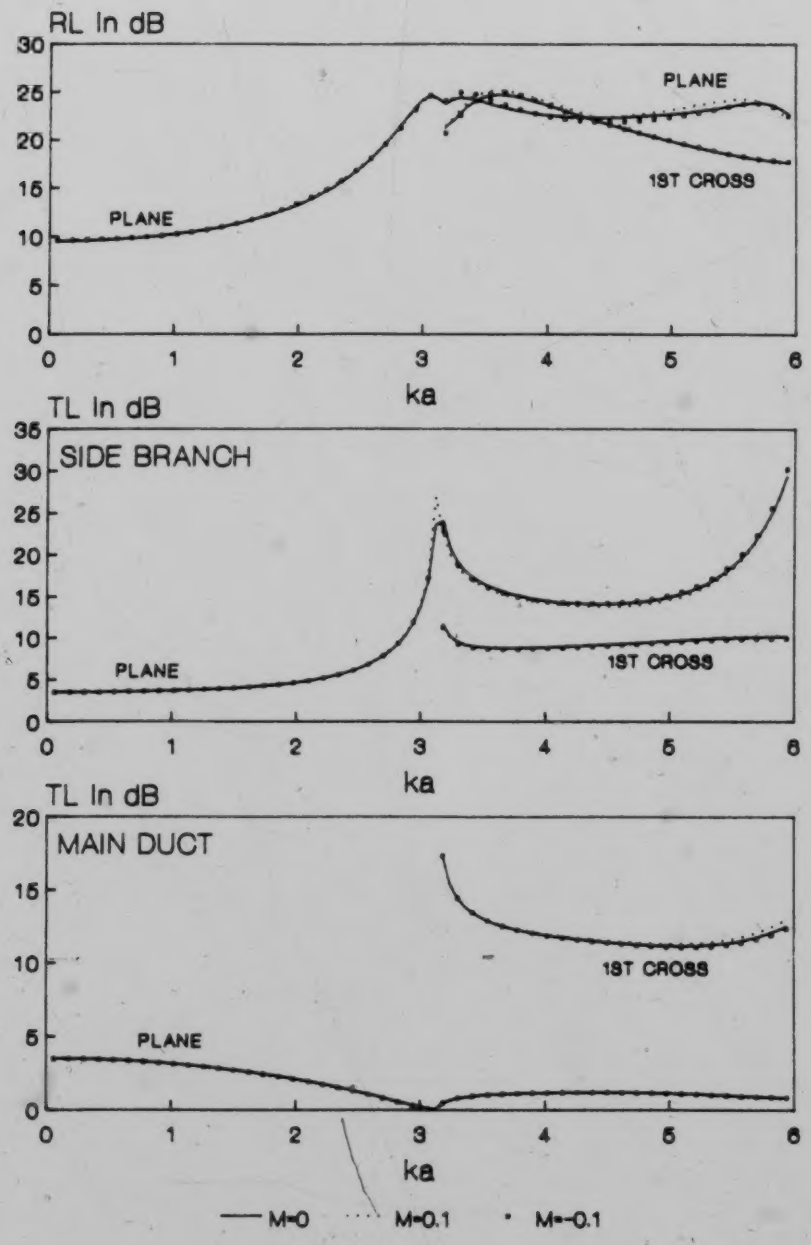

Figure 4.15 The Effect of Flow on Sound Propagation for a 90 Degree Side Branch with the Same Width as the Main Duct and an Equal Flow Split with a Plane Wave Incident

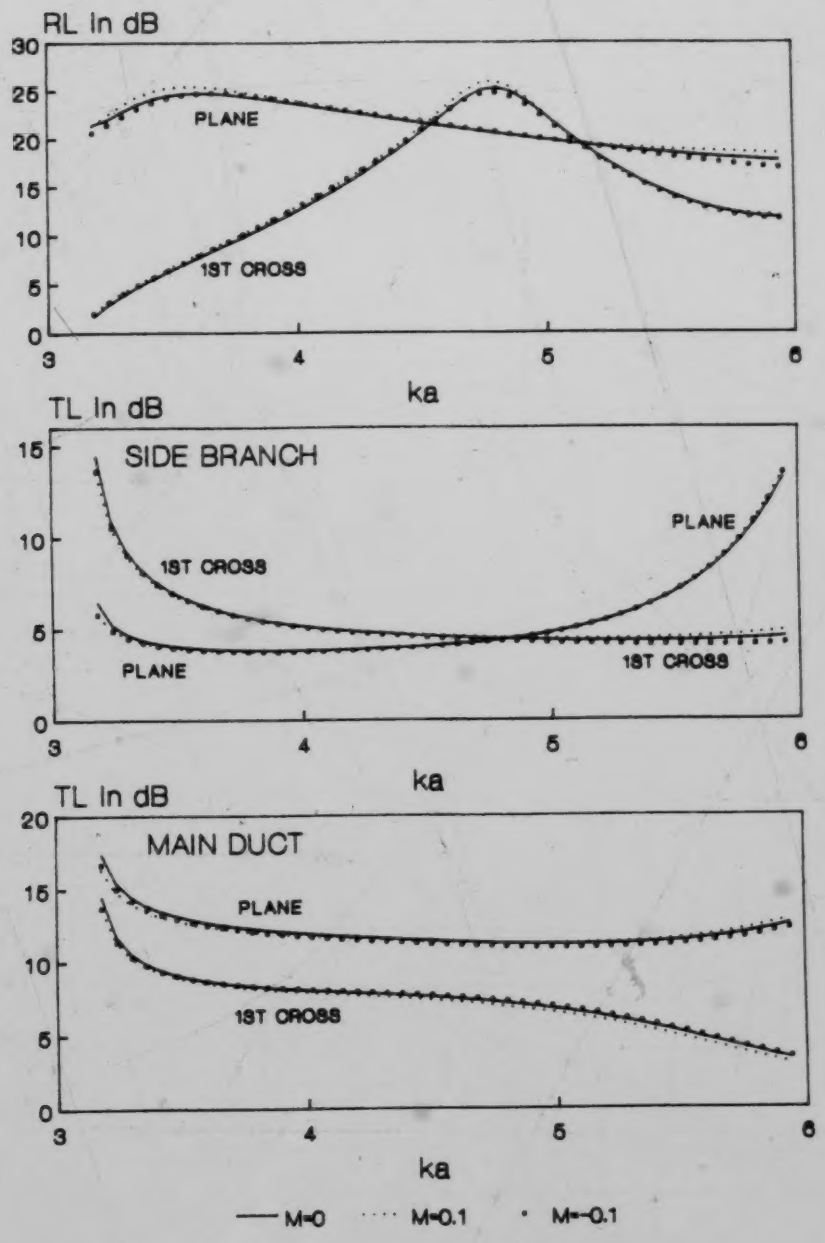

Figure 4.16 The Effect of Flow on Sound Propagation for a 90 Degree Side Branch with the Same Width as the Main Duct and an Equal Flow Split with the First Cross Mode Incident

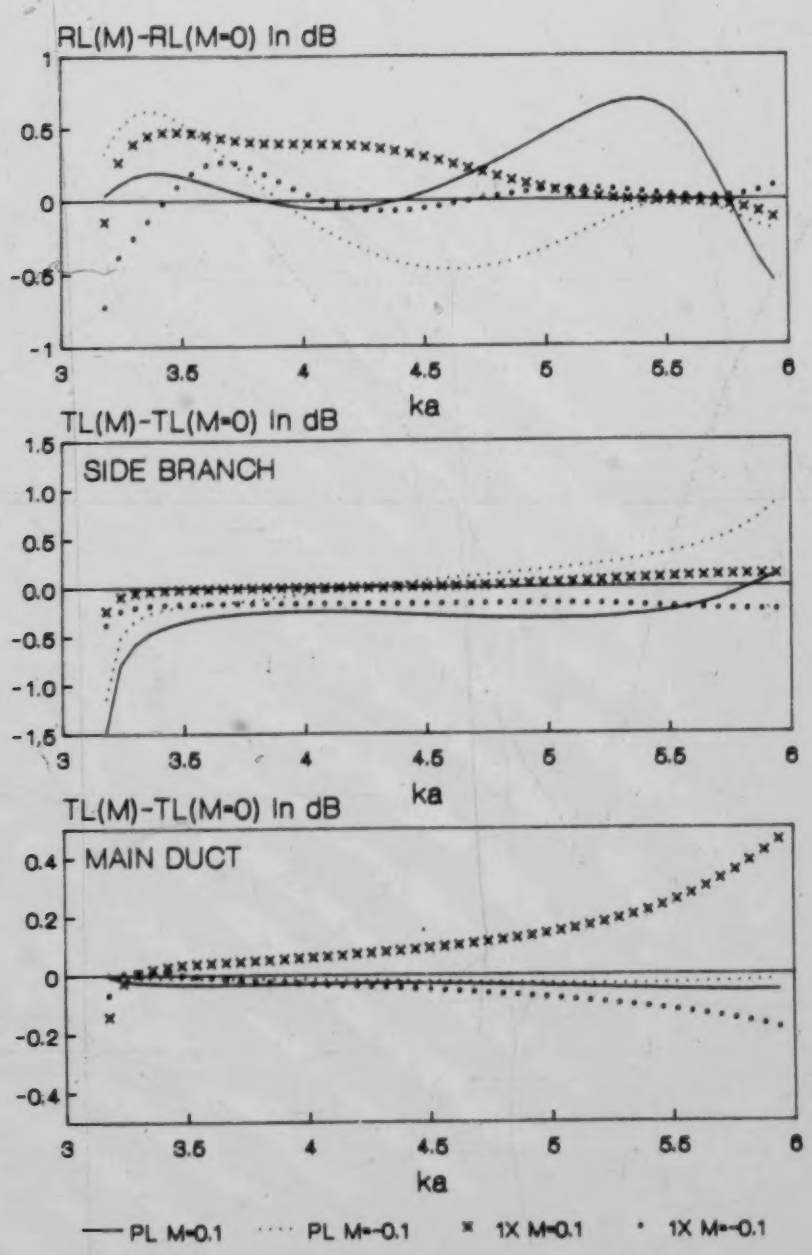

Figure 4.17 Change in RL and TL with respect to the No-flow Case for a 90 Degree Side Branch with the Same Width as the Main Duct and an Equal Flow Split with a Plane Wave Incident

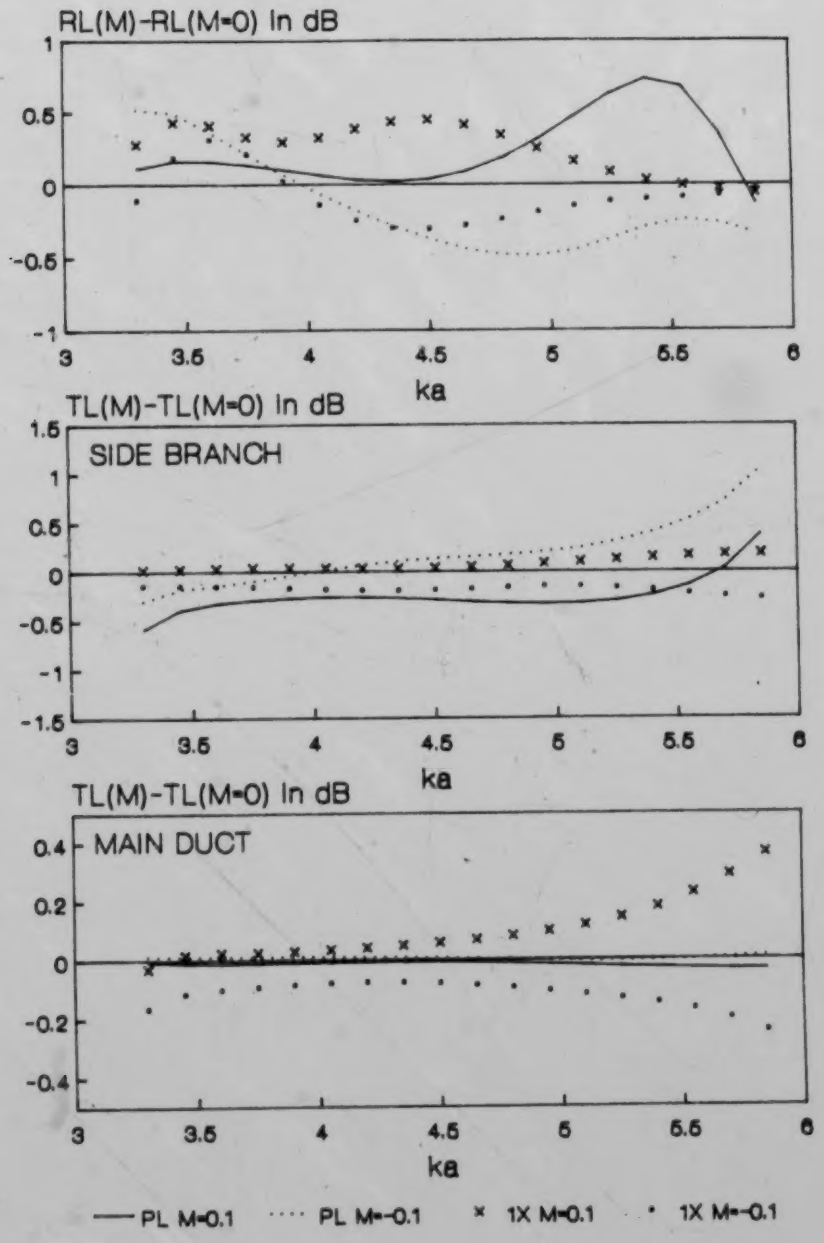

Figure 4.18 Change in RL and TL with respect to the No-flow Case for a 90 Degree Side Branch with the Same Width as the Main Duct and 10% of the Flow Out the Side Branch with a Plane Wave Incident

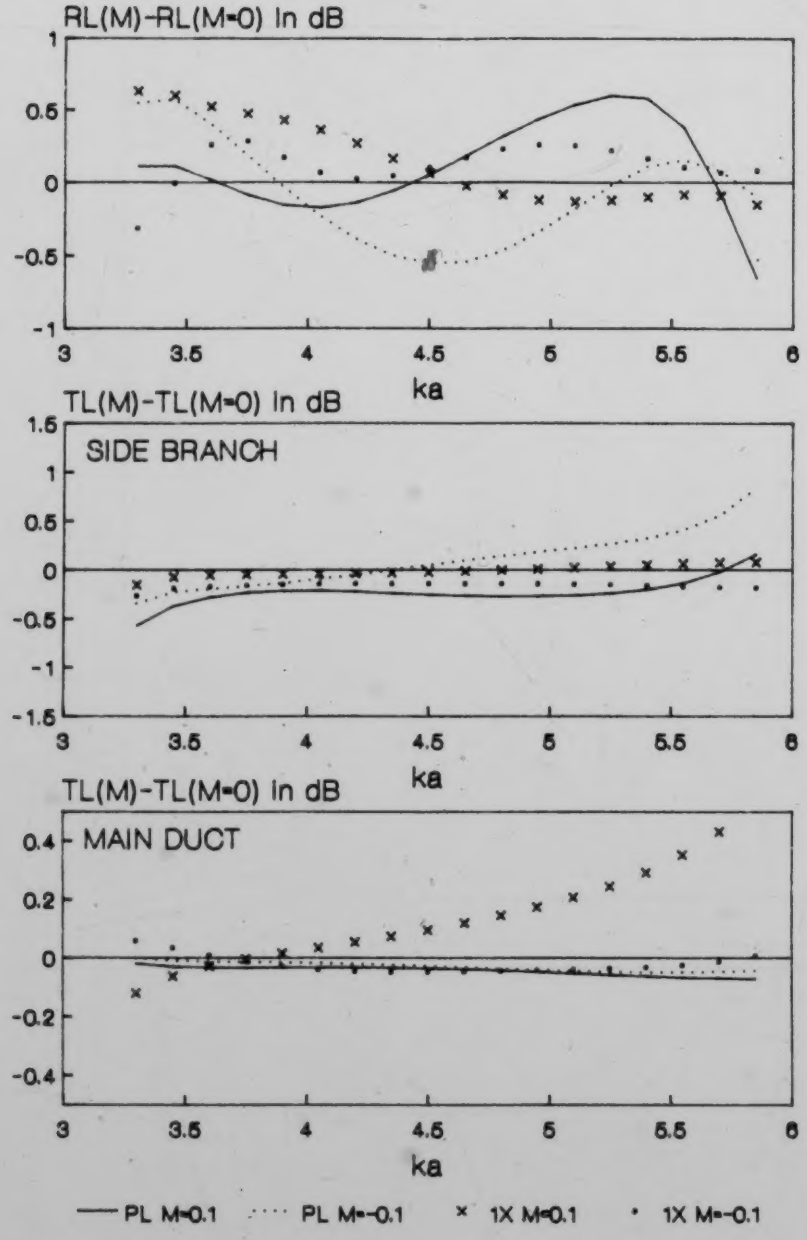

Figure 4.19 Change in RL and TL with respect to the No-flow Case for a 90 Degree Side Branch with the Same Width as the Main Duct and 90% of the Flow Out the Side Branch with a Plane Wave Incident

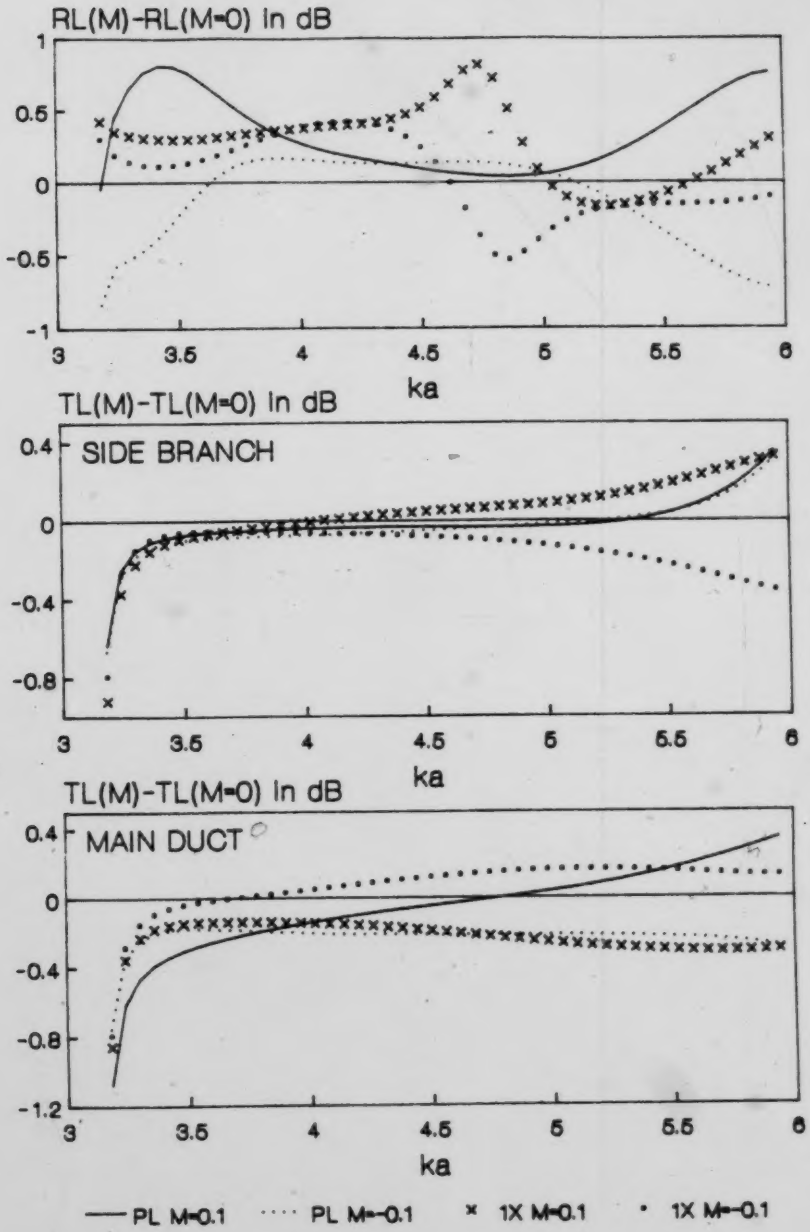

Figure 4.20 Change in RL and TL with respect to the No-flow Case for a 90 Degree Side Branch with the Same Width as the Main Duct and an Equal Flow Slit with the First Cross Mode Incident

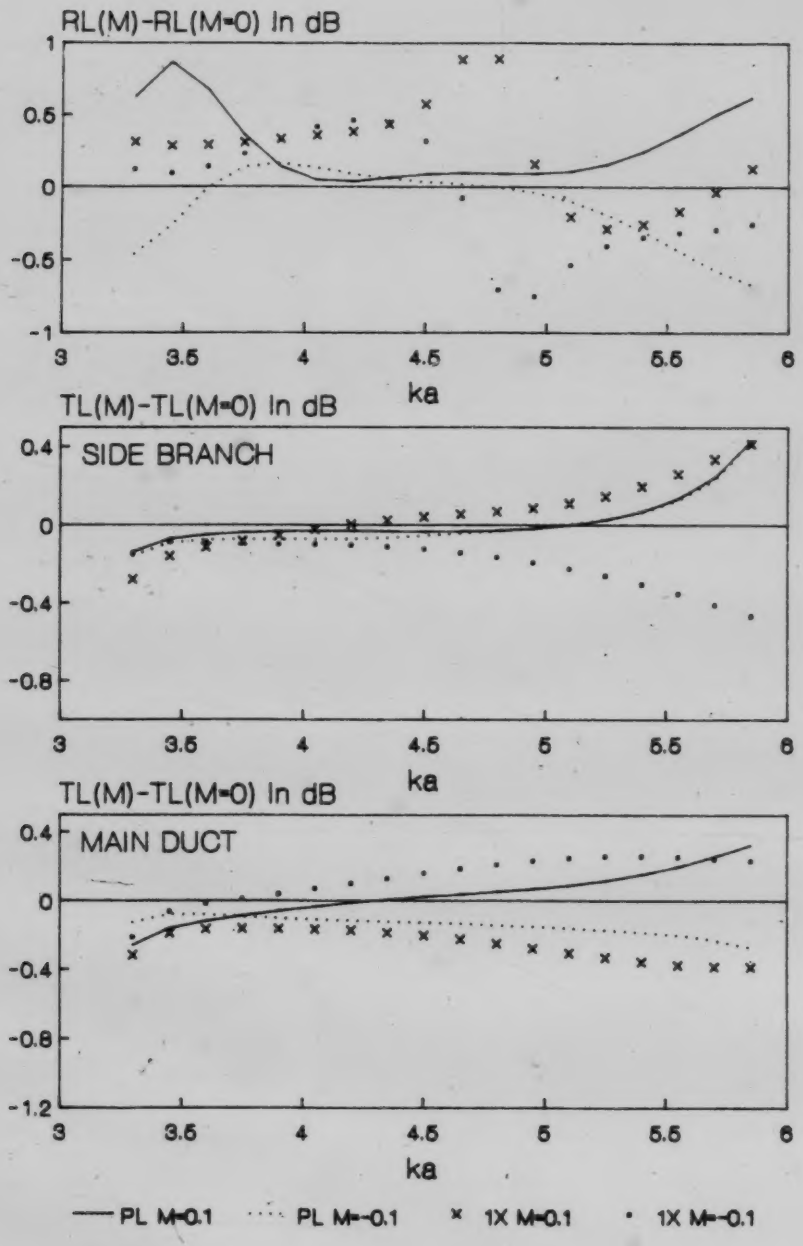

Figure 4.21 Change in RL and TL with respect to the No-flow Case for a 90 Degree Side Branch with the Same Width as the Main Duct and 10% of the Flow Out the Side Branch with the First Cross Mode Incident

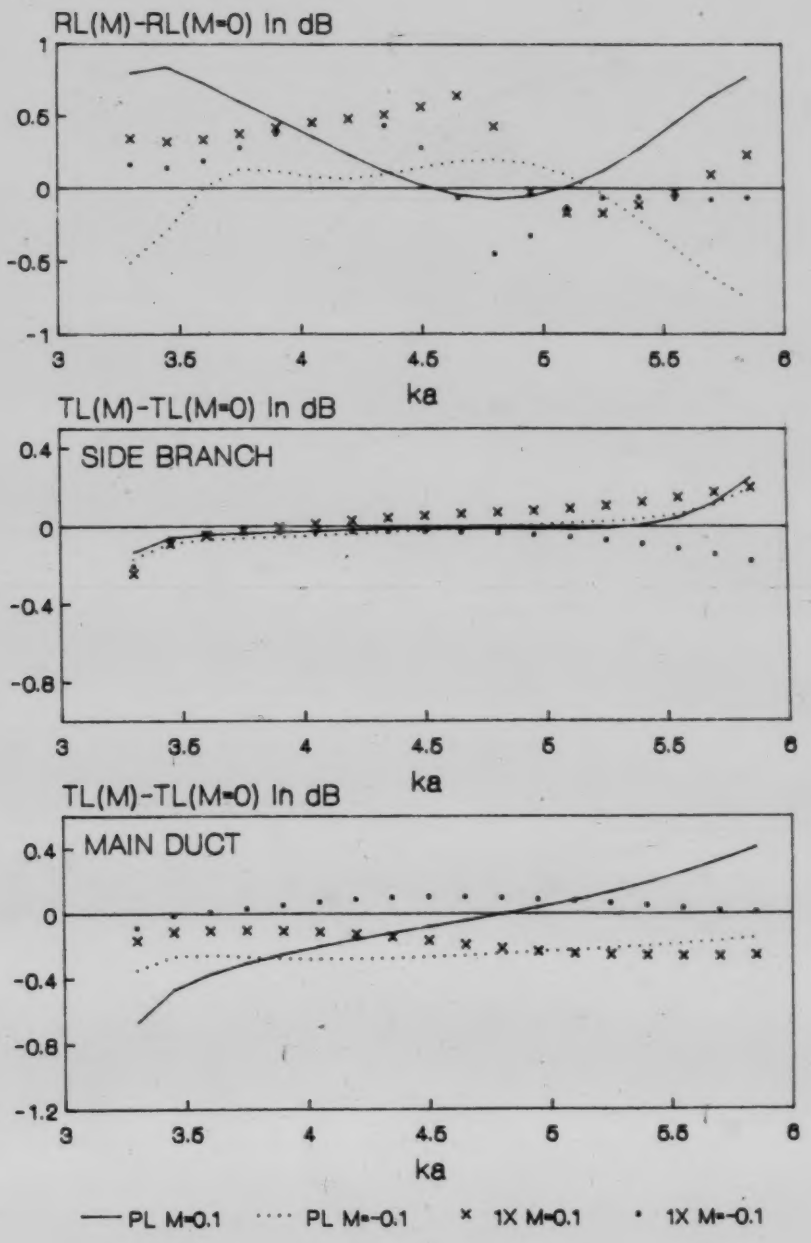

Figure 4.22 Change in RL and TL with respect to the No-flow Case for a 90 Degree Side Branch with the Same Width as the Main Duct and 90% of the Flow Out the Side Branch with the First Cross Mode Incident

the curves are most complicated for the reflection loss RL. In these cases, the side branch plane wave transmission loss is unaffected by the flow except near the cross mode cut-on frequencies while first cross mode shows greater changes with flow.

As indicated above, it would be desirable to use finer mesh models to confirm the above results with flow. Probably the major conclusion that can be drawn from this is that for Mach numbers of 0.1 or less the convective effect of flow has a relatively small influence on duct bend and junction transmission losses.

4.4.3 FEM Predictions for a 90 Degree Half Width Side Branch

This section considers a duct junction with a 90 degree side branch which has half the width of the inlet and continuing duct. The ISOHERM12 mesh used to model this junction is shown in Figure 4.23. The results for this junction are shown for the no-flow case and for the case of an inlet Mach number of 0.1 and equal flow velocities of Mach 0.0667 in the continuing main duct and side branch. The non-dimensional frequency parameter ka is based on the inlet duct width.

The RL and TL values predicted for this junction with a plane wave incident are shown in Figure 4.24. The graphs are generally similar to that obtained for the full width side branch shown in Figure 4.15 and show similar effects of flow. One difference is the decreased plane wave reflection and side branch transmission at low frequencies due to the decrease in cross-sectional area of the branch. There is also a sharper peak in the reflection loss graph near the cut-on of the first cross mode at $ka = \pi$. The other major difference is the absence of the first cross mode in the transmission loss graph for the side branch. The cut-on of the first cross mode in the branch occurs at $ka = 2\pi$ for no flow.

The results with the first cross mode incident, shown in Figure 4.25 for the half width branch, also show significant changes in the curves as a function of

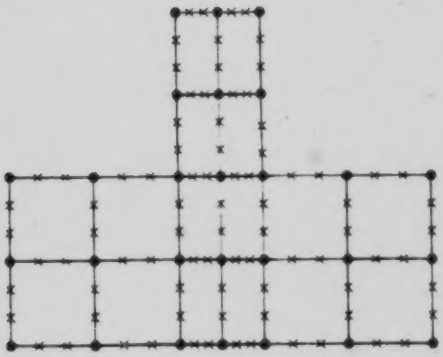

Figure 4.23 ISOHERM12 Element Mesh for a 90 degree Side Branch with Half the Width of the Main Duct

frequency compared to the results for a full width side branch shown in Figure 4.16. The most significant change was for the first cross mode reflection loss curve which for the full width side branch showed a peak in RL near $ka = 4.8$. For the half width branch the corresponding RL curve continually increased over the frequency range considered, shifting the peak (if it still occurs) to a point above $ka = 6$. The effect of flow with an inlet Mach number of 0.1 was small and generally similar to that found for the full width branch.

4.4.4 FEM Predictions for a 45 Degree Side Branch

The last junction to be considered in this chapter is a more complex junction containing a 45 degree side branch and a tapered section reducing the cross-sectional area of the continuing duct—probably more typical of junctions occurring in HVAC systems than the 90 degree side branches considered previously.

The finite element mesh used for this junction is shown in Figure 4.26. Note that a mesh with only one element across the duct width had be used. This leads to one of the limitations of the present prediction method as developed in

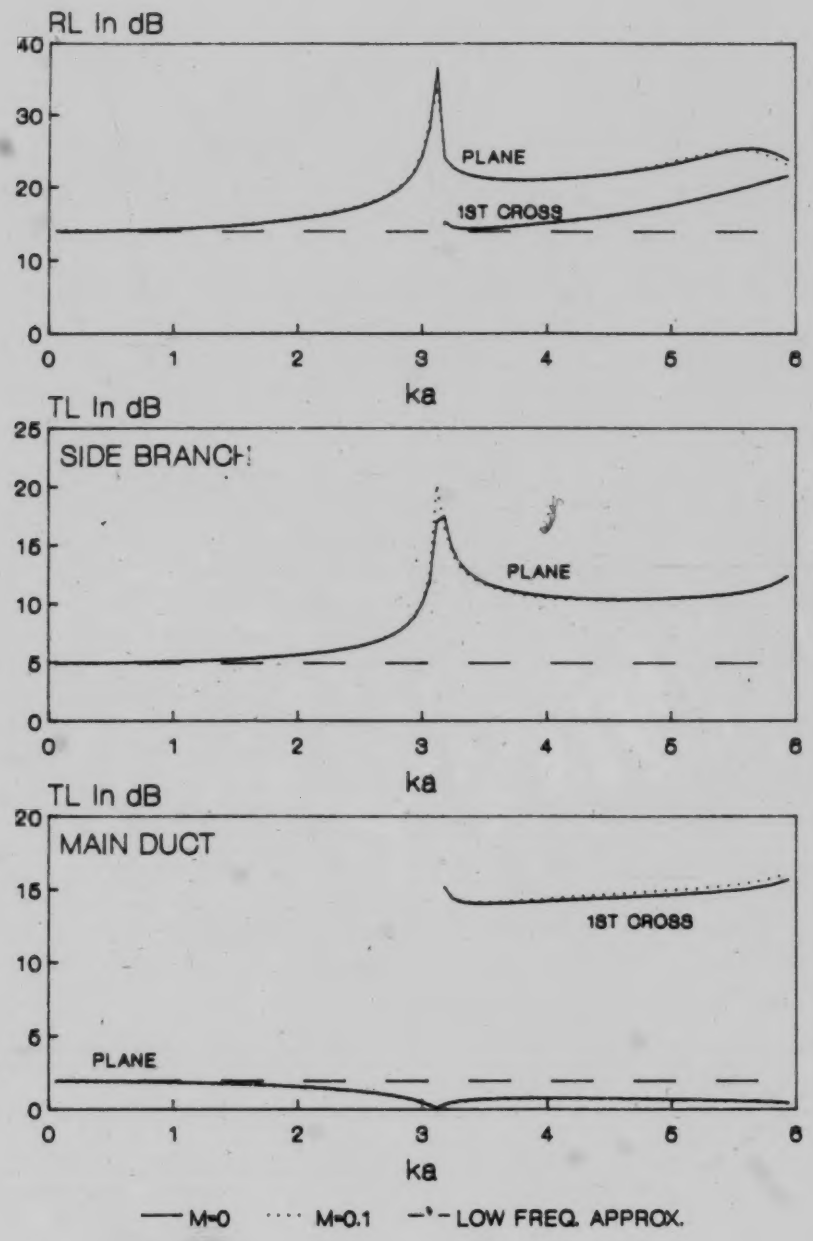

Figure 4.24 The Effect of Flow on Sound Propagation for a 90 Degree Side Branch with Half the Width of the Main Duct and 1/3 of the Flow Out the Side Branch with a Plane Wave Incident

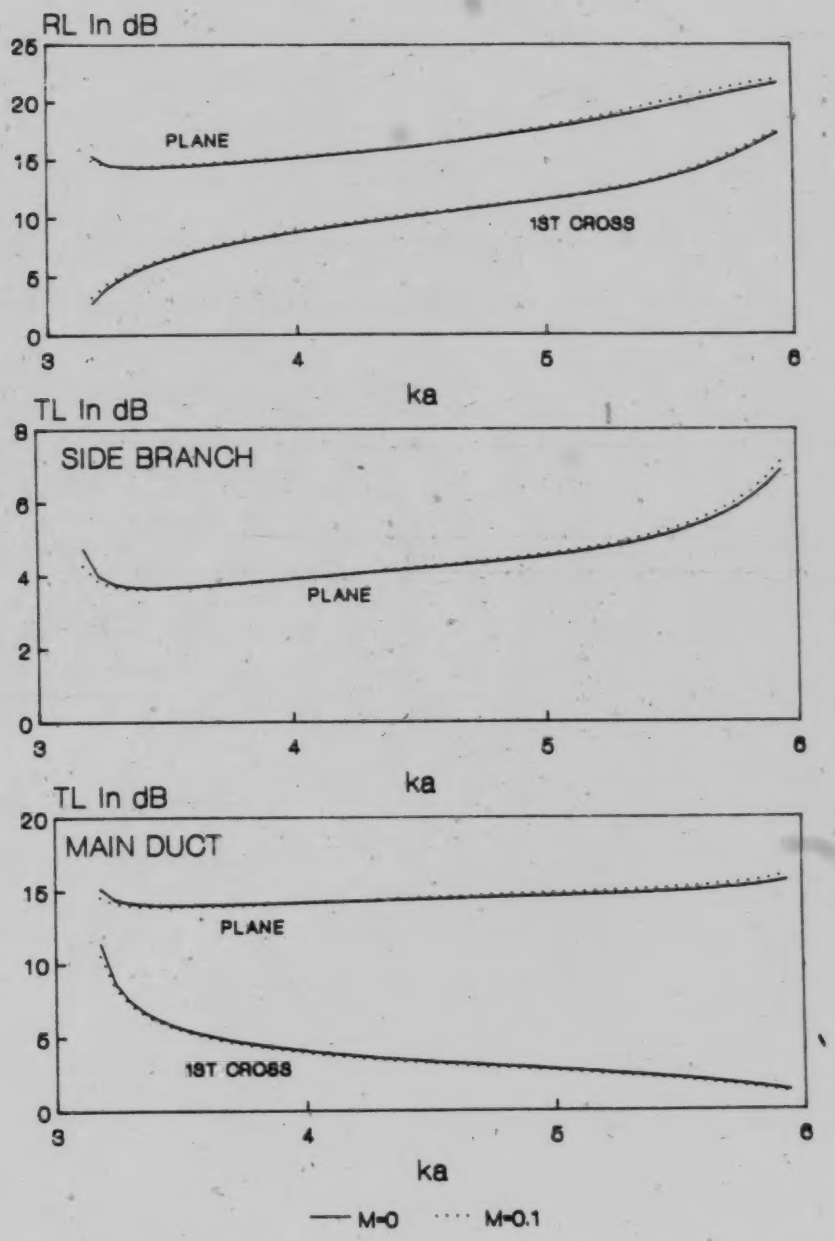

Figure 4.25 The Effect of Flow on Sound Propagation for a 90 Degree Side Branch with Half the Width of the Main Duct and 1/3 of the Flow Out the Side Branch with the First Cross Mode Incident

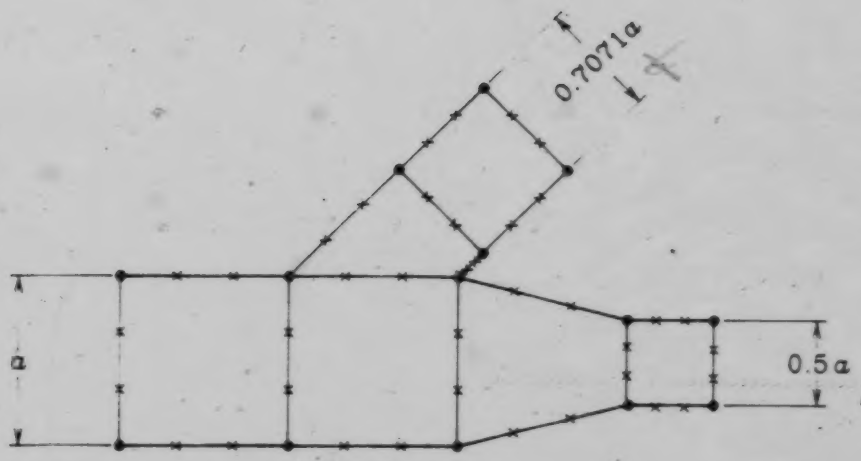

Figure 4.26 ISOHERM12 Element Mesh for a Junction with a 45 Degree Side Branch

Chapter III. The global finite element model, given by the global matrix equation shown in Equation 3.52, is in terms of acoustic velocity potential and derivative nodal quantities. These derivative nodal quantities are with respect to the global spatial coordinates. The duct cross-section modal matrices introduced in Section 3.1.6.4 for the modes occurring at the connecting straight duct interfaces are in terms of velocity potential nodal quantities and derivative nodal quantities tangent to the connecting duct interfaces. These can only be used directly in the current method if the normal to the interface surface is parallel to one of the global coordinate axes. The one exception is the case when only one element is used across the duct cross-section. In this case, for a hard walled duct the derivative quantities were constrained to zero so that the nodal quantities were in terms of the velocity potential only and connecting interfaces at any angle could be used. The conventional isoparametric elements such as HEX12 and HEX32 discussed in Chapter II do not have this problem since the nodal quantities used with these elements do not involve derivative quantities and thus could be used with the present method

for connecting duct interfaces at any angle.

The resulting predictions for this 45 degree junction are shown in Figure 4.27. In view of the coarseness of the mesh used, the results may not be very accurate especially above $ka = 3$. The side branch and continuing duct plane wave TL curves are similar to that obtained for a similar but not identical junction studied by Stredulinsky, Craggs and Faulkner [55] using two quadratic HEX8 elements across the duct widths and constraining connecting duct interfaces to plane waves. The side branch plane wave TL curve contains a "hump" reaching a maximum at roughly half the cut-on frequency of the first cross mode. This hump did not occur in the simple 90 degree branch results shown in Figure 4.14 and 4.24. It is similar to that occurring in a simple 1/4 wavelength expansion chamber with a length a. Along the path from the inlet to the branch outlet there is an expansion and contraction occurring roughly over a length a which may be working effectively like a 1/4 wavelength expansion chamber.

The results tend to diverge more rapidly from the low frequency approximation than for the simpler 90 degree elbows. For example, the results for the 90 degree branch shown in Figure 4.24 follow the horizontal line representing the low frequency approximation closely up to $ka = 1$, whereas the results of Figure 4.27 for the 45 degree side branch diverge significantly for ka of between 0.2 and 0.4.

As indicated above, due to the coarseness of the finite element mesh, the results for first cross mode are probably not very accurate. They do, however, show the different ka cut-on values for the different width branches, which are analytically π for the reflected wave, $\pi\sqrt{2}$ and 2π for the branch and duct continuing straight on. Further work is required to modify the prediction method so that finer meshes could be used to confirm the above results for branches at 45 degrees or any other desired angle.

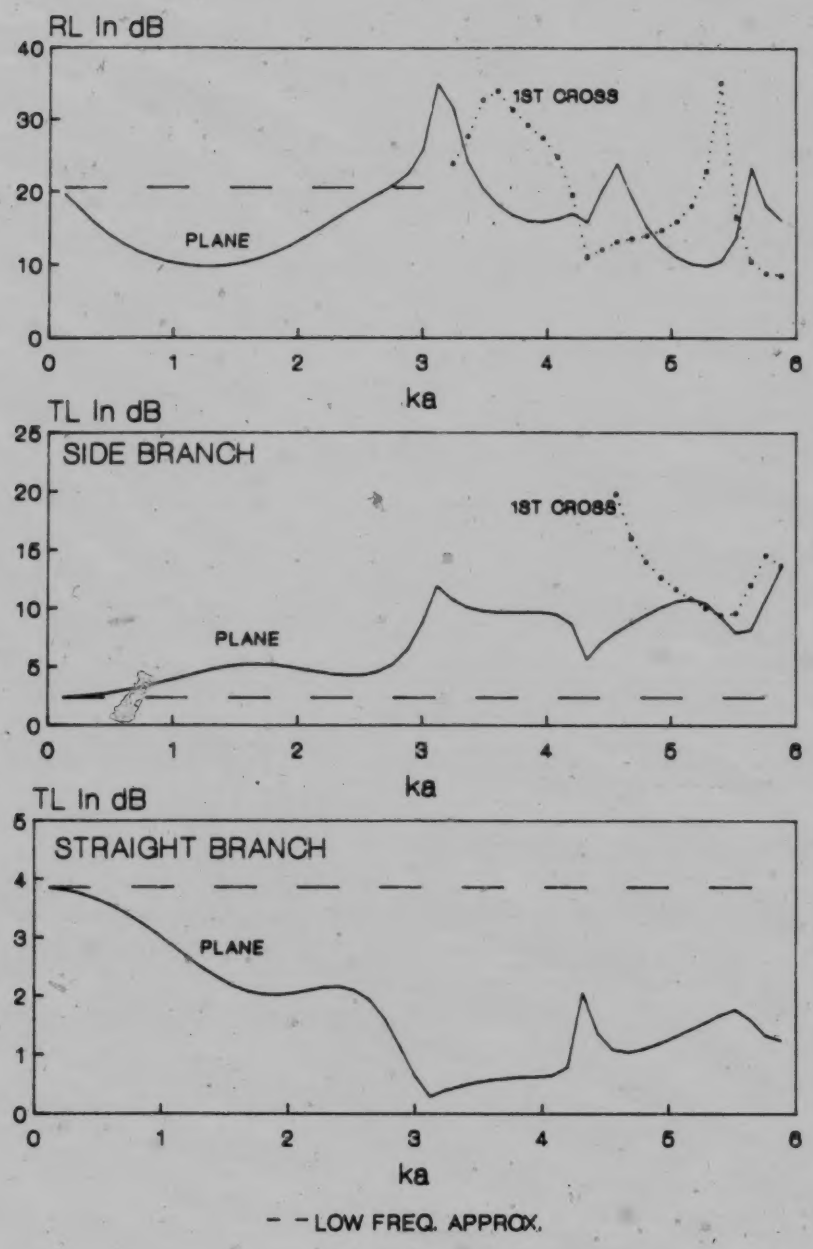

Figure 4.27 Propagation of Sound Through a Duct Junction with a 45 Degree Side Branch and No Flow for a Plane Wave Incident

CHAPTER V

CONCLUDING REMARKS

5.1 Summary

This thesis has considered the development of a cubic isoparametric Hermitian hexahedral finite element to efficiently model the propagation of sound through rigid walled duct bends and junctions. With the goal of improved technology transfer, the computer programs developed have been implemented on a desk top computer.

The element was initially tested by considering the acoustic enclosure eigenvalue problem, governed by the Helmholtz equation, and the incompressible potential fluid flow problem governed by Laplace's equation. The results for this new element have been compared to results for the conventional cubic isoparametric element which uses Serendipity shape functions and has the same number of degrees of freedom as the new Hermitian element. The new element leads to fewer degrees of freedom in global models compared to the conventional cubic isoparametric element models having the same number of elements (typically giving 40% fewer degrees of freedom). This is achieved by concentrating nodal quantities at the corners of the element and also explicitly constraining derivative nodal quantities at the rigid walled boundaries. It was demonstrated that the new element generally gave more accurate results on a degree of freedom basis. This improved accuracy was greatest for the case where the cuboid parent elements remained rectangular. Under certain

twisting distortions of the element boundaries, the new element gave much higher errors than the conventional isoparametric element.

A finite element model using this element was then developed to study the propagation of sound through duct bends and junctions including the convective effect of low Mach number steady fluid flow through the bend or junction. Due to memory limitations of the computer, a two-dimensional version of the element was used for this part of the work. The fluid flow was modeled using incompressible potential flow theory. The flow field was obtained first and then used in the equation governing the acoustic model. The same element mesh was used for both the acoustic and flow models. The initial development was tested with boundary conditions limiting the sound propagation to plane waves in straight ducts connected to the bend or junction models. This was then extended to consider higher order mode boundary conditions. An undistorted element model was then used to model propagation with flow in a straight duct. Propagation of modes up to and including the third cross mode was considered, and accurate results obtained up to $ka = 12$ with three elements across the duct cross-section. A distorted element model was tested for the problem of a mitred duct bend with a curved inner corner. This problem required three elements across the duct cross-section to accurately model plane wave and first cross mode propagation up to $ka = 6$.

Following the development and testing of the acoustic-flow model, the procedure was used to consider two additional duct bend problems and to study sound propagation in duct junctions. The first bend considered was a 90 degree mitred bend which could be modeled with undistorted elements. In this case it was found that models with only two elements across the duct width could accurately model plane wave and first cross mode propagation up to $ka = 6$. It was also

demonstrated that in the absence of flow, with the present procedure, it is not necessary to extend the FEM model very far into the connecting straight ducts since the evanescent modes were included in the boundary conditions.

The second bend considered was a curved 90 degree bend with a turning vane. Modeling this bend required distorted elements and there were significant differences, above $ka = 4$, between models with two elements and three elements across the cross-section and some difference between these models at a transmission loss peak between $ka = 1.5$ and $ka = 2$. This predicted peak was in one case roughly 10% higher than measured and predicted by another researcher using a FDM model. This problem also demonstrated, as found earlier when studying acoustic enclosures, that one must be cautious in constraining nodal derivative quantities at boundary discontinuities. The constraint of nodal derivative quantities along continuous boundaries or at 90 degree corners to explicitly satisfy boundary conditions can lead to models with fewer degrees of freedom without sacrificing accuracy. However at acute or oblique angle corners and other discontinuities, for example, the end point of a turning vane, it was found best to leave the nodal quantities unconstrained and thus handled by the implicit boundary conditions.

The last subject treated in this thesis was the propagation of sound through duct junctions. The first junction considered was a simple junction with a 90 degree side branch having the same width as the main duct. With the finite element model extended one duct width into the connecting ducts it was found that only two elements could be used across the duct cross-section without exceeding the computer's memory capacity. In the absence of flow, a model with three elements across the duct cross-section, but with shortened regions in the connecting ducts, was used to confirm that the models with two elements across the duct width

gave sufficiently accurate results up to $ka = 6$ for plane wave and first cross mode propagation. Results for 10%, 50% and 90% of the flow out the side branch were obtained with an inlet Mach number of 0.1. It was found that the flow had only a small effect, changing the transmission loss values by less than 1 decibel for the plane wave and first cross modes up to $ka = 6$ with the exception of near the cut-on for the first cross mode where differences of up to 3 dB were noted. Predictions were also made for a 90 degree side branch which has half the width of the main duct with equal flow velocities out the branch and continuing duct. The flow effects were similar to that obtained for the full width branch.

The last junction considered contained a 45 degree side branch and tapered section in the continuing duct just after the branch. The results for this junction showed more complex curves for the reflection loss and transmission loss as a function of frequency than did the simple 90 degree side branches. There was also greater deviation from the frequency independent low frequency plane wave approximation. This problem also demonstrated one deficiency in the current procedure—it can only be used with the isoparametric Hermitian element for bends or junctions in which the connecting duct interfaces are parallel to the global coordinate axes, for cases where more than one element is used across the duct cross-section. This problem does not occur if conventional isoparametric elements are used.

5.2 Areas of Further Research

There were several areas encountered in this work concerning the development and testing of the ISOHERM32 element which could be investigated further.

In Section 2.2.2, it was noted that this new element has C^1 continuity when undistorted but generally has only C^0 continuity when distorted. It was observed that if the elements formed segments of a polar grid then C^1 continuity was also achieved. It would be interesting to consider in more detail types of distortions which maintain the C^1 continuity of this element.

In Section 2.3.2.3, it was observed that the twisting of the common plane between two ISOHERM32 elements forming a rectangular enclosure caused large increases in the prediction error of the eigenfrequency for the first axial mode perpendicular to this plane. This behavior did not occur in a similar model using the conventional isoparametric HEX32 element. It would be of interest to investigate this further to determine the reason for this difference in behavior between these elements. The problem of the curved bend with a turning vane discussed in Section 4.3 showed some discrepancies between the predicted FEM results and experiment and FDM results of another researcher. Part of the problem appears to be the increased inaccuracies of the distorted elements, which means that a finer element mesh is needed to handle this problem—a model too large to run on the desk top computer used for the current work.

As indicated above, the last junction considered in this thesis was a 45 degree branch. This problem demonstrated that the present procedure can only model bends or junctions where the connecting straight duct interfaces are parallel to the global Cartesian coordinate axis for the case of more than one element across the duct cross-section. It should be possible to modify the global matrix equation for the finite element model given by Equation 3.84 so that nodal derivative quantities on the connecting duct interfaces are in terms of normal and tangential derivative quantities rather than derivatives with respect to the global axes. This would then

allow the modal matrix and modal recipe vectors for duct interfaces at any angle to be used in the finite element models. Also due to limitations of the computer system used for this work, all the bend and junction predictions have been made using a two-dimensional version of the element. Certainly much work could be done on a main frame computer, applying the element to three-dimensional bends and junctions for ducts of rectangular cross-section and also ducts with circular or oval cross-sections.

The duct network problem discussed in Section 1.3 was treated by Craggs and Stredulinsky [23] and Stredulinsky, Craggs and Faulkner [55] combining the transfer matrix and finite element methods, using exact plane wave solutions in straight ducts and FEM models in bends, junctions and other areas where two or three-dimensional effects are important. It should be possible to use the method developed in this thesis to consider higher order mode boundary conditions for the FEM models linked to straight ducts in which exact solutions including higher order modes are used, extending the predictions to higher frequencies including the convective effect of flow. The work in this thesis indicated that low Mach number flow had little effect on the bend and junction transmission losses, however, as indicated by the straight duct results of Section 3.3.2, the flow can have significant effect on phases of the acoustic waves. In the work for reference [55] it was observed that small changes in the duct network dimensions caused considerable change in the overall network transmission loss. Thus it is likely that the phase changes occurring in the bends and junctions and in the straight duct sections, even for flows at low Mach number, may have much greater influence on the overall duct network than observed for individual system components.

Other areas where further work is required, if the goal of obtaining more accurate methods for noise prediction in HVAC duct systems is to be achieved,

include implementing models with absorptive duct linings and flexible walled ducts and considering the problem of flow generated noise within the duct systems. Based on the work conducted in this thesis and references [23] and [55], the implementation of such a prediction scheme for a real HVAC system is probably still within the realm of a mainframe computer, but in view of the rapid development of computer technology, may soon be possible using a personal desk top computer and thus more accessible to design engineers.

BIBLIOGRAPHY

[1] American Society of Heating, Refrigeration and Air Conditioning Engineers, *Heating, Ventilation and Air Conditioning Systems and Applications*, Chapter 52, 1987.

[2] Astley, R.J., "A finite element, wave envelope formulation for acoustical radiation in moving flows", Journal of Sound and Vibration, Vol. 103, No. 4, 1985, pp. 471 - 485.

[3] Astley, R.J. and Eversman, W., "A finite element method for transmission in non-uniform ducts without flow: Comparison with the method of weighted residuals", Journal of Sound and Vibration, Vol. 57, No. 3, 1978, pp. 367 - 388.

[4] Astley, R.J. and Eversman, W., "A finite element formulation of the eigenvalue problem in lined ducts with flow", Journal of Sound and Vibration, Vol. 65, No. 1, 1979, pp. 61 - 74.

[5] Astley, R.J. and Eversman, W., "The finite element duct eigenvalue problem: An improved formulation with Hermitian Elements and no-flow condensation", Journal of Sound and Vibration, Vol. 69, No. 1, 1980, pp. 13 - 25.

[6] Astley, R.J. and Eversman, W., "Acoustic transmission in non-uniform ducts with mean flow, Part II: The finite element method", Journal of Sound and Vibration, Vol. 74, No. 1, 1981, pp. 103 - 121.

[7] Buma, C.J., *Multiple-source Excitation of Acoustic Resonances of Damped Small-Room Enclosures*, M.Sc.Thesis, University of Alberta, 1986.

[8] Burnett, D.S., *Finite Element Analysis from Concepts to Applications*, Addison-Wesley, Reading, Massachusetts, 1987.

[9] Cabelli, A., "The acoustic characteristics of duct bends", Journal of Sound and Vibration, Vol. 68, No. 3, 1980, pp. 369 - 388.

[10] Cabelli, A., "The influence of flow on the acoustic characteristics of a duct bend for higher order modes – a numerical study", Journal of Sound and Vibration, Vol. 82, No. 1, 1982, pp. 131 - 149.

[11] Cabelli, A., "Application of the time dependent finite difference theory to the study of sound and vibration interactions in ducts", Journal of Sound and Vibration, Vol. 103, No. 1, 1985, pp. 13 - 23.

BIBLIOGRAPHY (continued)

[12] Cabelli, A., "The propagation of sound in a square duct with a non-rigid side wall", Journal of Sound and Vibration, Vol. 103, No. 3, 1985, pp. 379 - 394.

[13] Cabelli, A. and Shepherd, I.C., "The influence of geometry on the acoustic characteristics of duct bends for higher order modes", Journal of Sound and Vibration, Vol. 78, No. 1, 1981, pp. 119 - 129.

[14] Cabelli, A. and Shepherd, I.C., "Duct acoustics – a numerical technique for the higher order mode solution of three-dimensional problems with rigid walls and no flow", Journal of Sound and Vibration, Vol. 92, No. 3, 1984, pp. 419 - 426.

[15] Chung, J.Y. and Blaser, D.A., "Transfer function method of measuring in-duct acoustic properties. I. Theory", Journal of the Acoustical Society of America, Vol. 68, No. 3, 1980, pp. 907 - 913.

[16] Chung, J.Y. and Blaser, D.A., "Transfer function method of measuring in-duct acoustic properties. II. Experiment", Journal of the Acoustical Society of America, Vol. 68, No. 3, 1980, pp. 914 - 921.

[17] Craggs, A., "The transient response of a coupled plate-acoustic system using plate and acoustic finite elements", Journal of Sound and Vibration, Vol. 15, No. 4, 1971, pp. 509 - 528.

[18] Craggs, A., "The use of simple three dimensional acoustic finite elements for determining the natural modes and frequencies of complex shaped enclosures", Journal of Sound and Vibration, Vol. 23, No. 3, 1972, pp. 331 - 339.

[19] Craggs, A., "An acoustic finite element approach for studying boundary flexibility and sound transmission between irregular enclosures", Journal of Sound and Vibration, Vol. 30, No. 3, 1973, pp. 343 - 357.

[20] Craggs, A., "A finite element method for damped acoustic systems: An application to evaluate the performance of reactive mufflers", Journal of Sound and Vibration, Vol. 48, No. 3, 1976, pp. 377 - 392.

[21] Craggs, A., "A finite element method for modelling dissipative mufflers with a locally reactive lining", Journal of Sound and Vibration, Vol. 54, No. 2, 1977, pp. 285 - 296.

[22] Craggs, A. and Stead, G., "Sound transmission between enclosures – A study using plate and acoustic finite elements", Acustica, Vol. 35, No. 2, 1976, pp. 89 - 98.

[23] Craggs, A. and Stredulinsky, D.C., "Analysis of acoustic wave transmission in a piping network", Journal of the Acoustical Society of America, Submitted for publication, 1989.

BIBLIOGRAPHY (continued)

[24] Cummings, A., "Sound transmission in curved duct bends", Journal of Sound and Vibration, Vol. 35, No. 4, 1974, pp. 451 - 477.

[25] Cummings, A., "Sound transmission in 180° duct bends of rectangular section", Journal of Sound and Vibration, Vol. 41, No. 3, 1975, pp. 321 - 334.

[26] Doak, P.E., "Excitation, transmission and radiation of sound from source distributions in hard-walled ducts of finite length (I): The effects of duct cross-section geometry and source distribution space-time pattern ", Journal of Sound and Vibration, Vol. 31, No. 1, 1973, pp. 1 - 72.

[27] Doak, P.E., "Excitation, transmission and radiation of sound from source distributions in hard-walled ducts of finite length (II): The effects of duct length", Journal of Sound and Vibration, Vol. 31, No. 2, 1973, pp. 137 - 174.

[28] Eversman, W., "Computation of axial and transverse wave numbers for uniform two-dimensional ducts with flow using a numerical integration scheme", Journal of Sound and Vibration, Vol. 41, No. 2, 1975, pp. 252 - 255.

[29] Eversman, W., "A reciprocity relationship for transmission in non-uniform hard walled ducts without flow", Journal of Sound and Vibration, Vol. 47, No. 4, 1976, pp. 515 - 521.

[30] Eversman, W., "Acoustic energy in ducts: Further observations", Journal of Sound and Vibration, Vol. 62, No. 4, 1979, pp. 517 - 532.

[31] Eversman, W. and Astley R.J., "Acoustic transmission in non-uniform ducts with mean flow, Part I: The method of weighted residuals", Journal of Sound and Vibration, Vol. 74, No. 1, 1981, pp. 89 - 101.

[32] Eversman, W., Cook, E.L. and Beckemeyer, R.J., "A method of weighted residuals for the investigation of sound transmission in non-uniform ducts without flow", Journal of Sound and Vibration, Vol. 38, No. 1, 1975, pp. 105 - 123.

[33] Fuller, C.R. and Bies, D.A., "Propagation of sound in a curved bend containing a curved axial partition", Journal of the Acoustical Society of America, Vol. 63, No. 3, 1978, pp. 681 - 686.

[34] Gladwell, G.M.L., "A finite element method for acoustics", 5^{e} Congres International D'Acoustique, Paper No. L33, 1965.

BIBLIOGRAPHY (continued)

[35] Kaizer, A.J.M., and Leeuwestein, A., "Calculation of the sound radiation of a nonrigid loudspeaker diaphragm using the finite-element method", Journal of the Audio Engineering Society, Vol. 36, No. 7/8, 1988, pp. 539 - 551.

[36] Ling S.F., Hamilton J.F., Allen J.J., "A Two-dimensional isoparametric Galerkin Finite Element for Acoustic-Flow problems", Transactions of the ASME, Journal of Mechanical Design, Paper No. 82-DET-97, 1982.

[37] Lippert, W.K.R., "The measurement of sound reflection and transmission at right-angled bends in rectangular tubes", Acustica, Vol. 4, 1954, pp. 313 - 319.

[38] Lippert, W.K.R., "Wave transmission around bends of different angles in rectangular ducts", Acustica, Vol. 5, 1955, pp. 274 - 278.

[39] Miles, J.W., "The diffraction of sound due to right-angled joints in rectangular tubes", Journal of the Acoustical Society of America, Vol. 19, No. 4, 1947, pp. 572 - 579.

[40] Morfey, C.L., "Sound transmission and generation in ducts with flow", Journal of Sound and Vibration, Vol. 14, No. 1, 1971, pp. 37 - 55.

[41] Morse,M., *Vibration and Sound*, American Institute of Physics, 1986.

[42] Munjal, M.L., *Acoustics of Ducts and Mufflers with Application to Exhaust and Ventilation System Design*, John Wiley & Sons, New York, 1987.

[43] Osborne, W.C., "Calculation of the angular propagation constant for a bend", Journal of Sound and Vibration, Vol. 37, No. 1, 1974, pp. 65 - 77.

[44] Panton, L., *Incompressible flow*, John Wiley & Sons, New York, 1984.

[45] Peat, K.S. "Evaluation of four-pole parameters for ducts with flow by the finite element method", Journal of Sound and Vibration, Vol. 84, No. 3, 1982, pp. 389 - 395.

[46] Redmore, T.L., and Mulholland, K.A., "The application of mode coupling theory to the transmission of sound in the sidebranch of a rectangular duct system", Journal of Sound and Vibration, Vol. 85, No. 3, 1982, pp. 323 - 331.

BIBLIOGRAPHY (continued)

[47] Rostafinsky, W., "On propagation of long waves in curved ducts", Journal of the Acoustical Society of America, Vol. 52, No. 5, 1972, pp. 1411 - 1420.

[48] Rostafinsky, W., "Analysis of propagation of waves of acoustic frequencies in curved ducts", Journal of the Acoustical Society of America, Vol. 56, No. 1, 1974, pp. 11 - 15.

[49] Rostafinsky, W., "Acoustic systems containing curved duct sections", Journal of the Acoustical Society of America, Vol. 60, No. 1, 1976, pp. 23 - 28.

[50] Seybert A.F., and Cheng C.Y.R., "Application of the boundary element method to acoustic cavity response and muffler analysis", Transactions of the ASME, Journal of Vibration, Acoustics, Stress and Reliability, Vol. 109, 1987, pp. 15 - 21.

[51] Shepherd, I.C. and Cabelli, A., "Transmission and reflection of higher order acoustic modes in a mitred duct bend", Journal of Sound and Vibration, Vol. 77, No. 4, 1981, pp. 495 - 511.

[52] Shuku, T. and Ishihara, K., "The analysis of the acoustic field in irregularly shaped rooms by the finite element method", Journal of Sound and Vibration, Vol. 29, No. 1, 1973, pp. 67 - 76.

[53] Sigman, R.K., Majjigi, R.K. and Zinn, B.T., "Determination of turbofan inlet acoustics using finite elements", American Institute of Aeronautics and Astronautics Journal, Vol. 16, No. 11, 1978, pp. 1139 - 1145.

[54] Stead, G., *Finite element approach to sound transmission*, M. Sc. thesis, University of Alberta, 1973.

[55] Stredulinsky, D.C., Craggs, A., Faulkner, M.G., "Acoustics of piping and ducts", Canadian Acoustics, Vol. 15, No. 4, 1987, pp. 3 - 14.

[56] Vo, P.T. and Eversman, W., "A method of weighted residuals with trigonometric basis functions for sound transmission in circular ducts", Journal of Sound and Vibration, Vol. 56, No. 2, 1978, pp. 243 - 250.

[57] von Said, A., "Theorie der schallausbreitung in kanälen mit rechtwinkligen ecken und verzweigungen", Acustica, Vol. 33, 1975, pp. 203 - 210.

[58] Young, C.J. and Crocker, M.J., "Prediction of transmission loss in mufflers by the finite-element method', Journal of the Acoustical Society of America, Vol. 57, No. 1, 1975, pp. 144 - 148.